

**Intelligent user-specific motion planning and control of lower-limb  
exoskeletons**

by

Javad Khodaei Mehr

A thesis submitted in partial fulfillment of the requirements for the degree of

Doctor of Philosophy

in

Biomedical Engineering

Department of Electrical and Computer Engineering  
University of Alberta

© Javad Khodaei Mehr, 2024

# Abstract

Recent strides in lower-limb exoskeleton development have significantly enhanced the potential for more effective rehabilitation and assistance for individuals with mobility impairments. Despite these advancements, the widespread adoption of exoskeletons demands improvements in both hardware and software design to enhance user comfort and safety. This doctoral research addresses this need by focusing on the implementation of personalized and safe locomotion patterns, addressing a critical shortfall in existing exoskeleton designs.

To empower users with the ability to modify gait trajectories during walking, a novel adaptable gait trajectory shaping method is introduced, leveraging adaptable central pattern generators (ACPGs). These ACPGs are synchronized across various joints and dynamically updated in response to the physical interaction between the human and the robot. Expanding on this, a fusion of reinforcement learning and ACPGs is proposed, enabling the generation of user-specific locomotion trajectories. This innovative approach reads the user’s physical human-robot interaction (pHRI) over time, facilitating the achievement of desired gait patterns, such as step length and walking velocity. Experimental validation on able-bodied individuals using the Indego lower-limb exoskeleton demonstrates the capability of refining exoskeleton gait trajectories in real-time.

To elevate safety levels, an algorithm is introduced to assess postural stability during changes in exoskeleton trajectories governed by ACPGs. An extended model for the divergent component of motion (DCM) is tailored for multi-degree-of-freedom (DOF) exoskeletons. Leveraging this algorithm, the exoskeleton gains the ability to

ensure postural stability and the viability of locomotion in pHRI by employing a DCM-based hip correction strategy to adjust the upper body position. The effectiveness of this intelligent controller for ensuring safe and stable locomotion is rigorously investigated through experimental studies conducted on the Indego lower-limb exoskeleton.

# Preface

The ultimate goal of this project is to make lower-limb exoskeletons adaptive to the user's gait pattern. This can provide a better experience of using these devices with less chance for injuries and higher chance for rehabilitation. This thesis is part of a multidisciplinary research collaboration, led by Dr. Mahdi Tavakoli (principal investigator) at the Department of Electrical and Computer Engineering, University of Alberta and Dr. Vivian Mushahwar at the Department of Medicine. All of the work presented in this thesis was conducted in the Telerobotic and Biorobotic Systems Lab and the Rehabilitation Innovations Core of the Sensory Motor Adaptive Rehabilitation Technology (SMART) Network at the University of Alberta.

I was responsible for the experiment design, performing the experiments, data collection and analysis, and the manuscript preparation. Also, the experimental setup was designed by myself. Dr. Mahdi Tavakoli and Dr. Mushahwar were the supervisory authors on this project and were involved throughout the project in concept formation and manuscript composition.

Chapter 1 presents the motivation and objectives of this project and summarizes the thesis organization and contributions. Parts of this chapter were published as: Javad K. Mehr, Mojtaba Akbari, Pouria Faridi, Hongjun Xing, Vivian K. Mushahwar, Mahdi Tavakoli, Artificial-Intelligence-Powered Lower-limb Assistive Devices: Future of Homecare Technologies, Advanced Intelligent Systems, 2023.

Chapter 3 of this thesis was published as: Mojtaba Sharifi, Javad Khodaei Mehr, Vivian K. Mushahwar, Mahdi Tavakoli, Autonomous Locomotion Trajectory Shaping and Nonlinear Control for Lower-Limb Exoskeletons, IEEE/ASME Transactions on

Mechatronics, 2022.

Chapter 4 of this thesis was presented as: Mojtaba Sharifi, Javad Khodaei Mehr, Vivian K. Mushahwar, Mahdi Tavakoli, Adaptive CPG-based Gait Planning with Learning-based Torque Estimation and Control for Lower-limb Exoskeletons, IEEE Robotics and Automation Letters, 2021.

Chapter 5 of this thesis was published as: Javad K. Mehr, Edward Guo, Mojtaba Akbari, Vivian K. Mushahwar, Mahdi Tavakoli, Deep Reinforcement Learning based Personalized Locomotion Planning for Lower-Limb Exoskeletons, IEEE International Conference on Robotics and Automation, London, UK, 2023.

Chapter 6 of this thesis was submitted to the journal of IEEE transactions on bionics and medical robotics as Javad K. Mehr, Mojtaba Akbari, Edward Guo, Pouria Faridi, Vivian K. Mushahwar, Mahdi Tavakoli, Locomotion Planning for Lower-Limb Exoskeletons via Intelligent Central Pattern Generators and Reinforcement Learning.

Chapter 7 of this thesis was published as: Javad K. Mehr, Mojtaba Sharifi, Vivian K. Mushahwar, Mahdi Tavakoli, Intelligent Locomotion Planning with Enhanced Postural Stability for Lower-Limb Exoskeletons, IEEE Robotics and Automation Letters, 2021. Also, selected for presentation at the IEEE/RSJ International Conference on Intelligent Robots and Systems, Prague, Czech Republic, 2021.

# Acknowledgements

I would like to express my deepest gratitude to my esteemed supervisors, Dr. Mahdi Tavakoli and Dr. Vivian Mushahwar, for their invaluable guidance, unwavering support, and continuous encouragement throughout my journey in completing this thesis. Their expertise, dedication, and insightful feedback have been instrumental in shaping my research and enhancing the quality of my work. I am truly grateful for their mentorship and for pushing me to achieve my best.

I would also like to extend my heartfelt appreciation to my friends in the TBS (Telerobotics and Biorobotics Systems) group and Mushahwar's lab. Their camaraderie, intellectual discussions, and shared experiences have enriched my research endeavors and made this journey enjoyable. I am grateful for their friendship, collaboration, and for being a constant source of motivation.

I owe a debt of gratitude to my beloved family for their unwavering love, encouragement, and belief in my abilities. Their support, understanding, and sacrifices have been invaluable in enabling me to pursue my academic goals. I am profoundly thankful to my parents, siblings, and extended family for always being there for me and for being the foundation of my strength.

Lastly, I would like to express my sincere appreciation to all the individuals, colleagues, and participants who contributed to this research in various ways. Your involvement and willingness to share your insights and experiences have been crucial to the success of this thesis.

To everyone who has played a part in this journey, whether big or small, your support has been indispensable, and I am deeply grateful for your presence in my life.

# Table of Contents

<b>1</b>	<b>Introduction</b>	<b>1</b>
1.1	Motivation . . . . .	1
1.2	Contributions of this research . . . . .	3
1.2.1	Provide an approach that can facilitate real-time modifications in the exoskeleton’s gait . . . . .	3
1.2.2	Make the gait trajectories adaptive with the user’s target loco- motion . . . . .	5
1.2.3	Upper-body position adjustment and postural stability . . . . .	6
1.3	Outline of this dissertation . . . . .	8
<b>2</b>	<b>Literature review</b>	<b>10</b>
2.1	Adaptive locomotion planning . . . . .	10
2.2	pHRI estimation methods . . . . .	11
2.3	Reinforcement learning algorithms for exoskeletons . . . . .	13
2.4	Exoskeleton simulating environments for training RL agents . . . . .	14
2.5	Postural stability for bipedal locomotion . . . . .	15
<b>3</b>	<b>Autonomous Locomotion Trajectory Shaping and Nonlinear Control for Lower-Limb Exoskeletons</b>	<b>17</b>
3.1	Introduction . . . . .	17
3.2	Exoskeleton Dynamics and Adaptive CPG-Based Online Trajectory Shaping . . . . .	20
3.3	TBA Disturbance-Observer-Based Control . . . . .	24
3.3.1	Controller and Observer Design . . . . .	24
3.3.2	Unified Stability Proof . . . . .	29
3.4	Experimental Studies . . . . .	30
3.5	Discussion . . . . .	36
3.6	Conclusion . . . . .	39

<b>4</b>	<b>Adaptive CPG-based Gait Planning and Control for Exoskeletons</b>	<b>41</b>
4.1	Introduction . . . . .	41
4.2	ACPG-Based Gait Planning . . . . .	43
4.3	Learning-Based pHRI Torque Estimation and Tracking Controller . .	46
4.3.1	NARX Neural Network Scheme . . . . .	47
4.3.2	Learning Algorithm . . . . .	50
4.3.3	Tracking Controller with Torque Compensation . . . . .	50
4.4	Experimental Evaluations . . . . .	51
4.5	Conclusion . . . . .	58
<b>5</b>	<b>Deep Reinforcement Learning based Personalized Locomotion Plan-</b>	
	<b>ning for Lower-Limb Exoskeletons</b>	<b>61</b>
5.1	Introduction . . . . .	61
5.2	Intelligent CPG dynamics . . . . .	62
5.3	Implementation of an RL agent to adjust energy contributions for tra-	
	jectory shaping . . . . .	65
5.3.1	Deep reinforcement learning . . . . .	65
5.3.2	Interaction energy modification via RL . . . . .	67
5.4	Results and Discussion . . . . .	68
5.4.1	Simulations . . . . .	69
5.4.2	Experimental evaluations . . . . .	72
5.5	Conclusion . . . . .	75
<b>6</b>	<b>Locomotion Planning for Lower-Limb Exoskeletons via Intelligent</b>	
	<b>Central Pattern Generators and Reinforcement Learning</b>	<b>77</b>
6.1	Introduction . . . . .	77
6.2	Simulation Environment . . . . .	79
6.3	Methodology . . . . .	82
6.3.1	Intelligent Central Pattern Generators . . . . .	82
6.3.2	Implementation of an RL agent to adjust energy contributions	
	for trajectory shaping . . . . .	84
6.4	Results and discussion . . . . .	87
6.4.1	Simulation results . . . . .	88
6.4.2	Empirical results . . . . .	90
6.5	Conclusion . . . . .	97

<b>7</b>	<b>Intelligent Locomotion Planning with Enhanced Postural Stability for Lower-Limb Exoskeletons</b>	<b>98</b>
7.1	Introduction . . . . .	98
7.2	Methodology . . . . .	100
7.2.1	DCM Analysis with 4DB Model . . . . .	100
7.2.2	DCM Offset for Viability of Walking . . . . .	104
7.2.3	ACPG Dynamics for Synchronized and Feasible Locomotion . . . . .	105
7.3	Results & Discussion . . . . .	108
7.3.1	Trunk Adjustment Using DCM Analysis . . . . .	109
7.3.2	Locomotion Shaping with Maximum Walking Frequency . . . . .	113
7.4	Conclusions . . . . .	115
<b>8</b>	<b>Conclusions, Recommendations, and Future Work</b>	<b>117</b>
8.1	Conclusions . . . . .	117
8.2	Limitations of this research . . . . .	122
8.3	Future Work . . . . .	123
	<b>Bibliography</b>	<b>126</b>
	<b>Appendix A: DCM dynamics</b>	<b>135</b>
A.1	Inertia matrix and gravity vector values: . . . . .	135
A.2	DCM definition . . . . .	136

# List of Tables

3.1	Coefficients of the Fourier series (3.7) for the hip and knee initial motions based on the analysis of normal gait trajectories . . . . .	32
3.2	Parameter and initial values of the proposed ACPGs dynamics (3.6) for the hip and knee joints . . . . .	33
6.1	Parameters of the proposed iCPGs and RL. . . . .	88

# List of Figures

1.1	Lower-limb exoskeletons developed for assisting/rehabilitating people with neurological impairments: a) HAL, b) ReWalk, c)Indego, d) Exo H3, and e) Ekso GT [13] . . . . .	2
3.1	The employed lower-limb exoskeleton (Indego by Parker Hannifin Corporation), and joint consequences from the stance leg to the swing one based on pinned (point-feet) model . . . . .	21
3.2	Autonomous two-level control strategy for lower-limb exoskeletons: Adaptive CPG-based gait trajectory update in high-level and nonlinear torque control in low-level, employing an adaptive HRI torque observer	24
3.3	Indego lower-limb exoskeleton worn by two able-bodied users for over-ground walking: first participant (33 year-old) and second participant (27 year-old) . . . . .	31
3.4	Estimated pHRI (a) torque and (b) energy for different joints, and (c) total frequency of the locomotion, obtained from the proposed ACPG in the presence of HRI for the first wearer . . . . .	34
3.5	(a) Desired and actual trajectories, (b) and (c) tracking errors of the knee and hip joints for the right leg in the presence of pHRI for the first wearer . . . . .	35
3.6	Trajectory and phase variation of the right hip with respect to the left hip for the first wearer . . . . .	36
3.7	Estimated pHRI (a) torque and (b) energy for different joints, and (c) total frequency of the locomotion, obtained from the proposed ACPG in the presence of HRI for the second wearer . . . . .	37
3.8	Trajectory and phase variation of the right hip with respect to the left hip for the second wearer . . . . .	38

4.1	ACPG-based gait planning: (a) control architecture, (b) ACPG structure for online adjustment of the locomotion’s frequency, amplitude and mean value, and (c) NARX model for the estimation of active pHRI torque . . . . .	48
4.2	Indego lower-limb exoskeleton assisting a human user in overground walking with a safety harness . . . . .	52
4.3	Variation of (a) interaction torque integral, (b) equilibrium position, and (c) corresponding logarithmic function value for the right and left hip joints . . . . .	54
4.4	Variation of trajectories for (a) left hip with respect to right hip, and (b) left knee with respect to left hip (black arrows show the direction of locomotion and red arrows show the direction of trajectory deviation)	56
4.5	Variation of (a) injected pHRI energy, (b) motion amplitude, and (c) corresponding logarithmic function value for the right and left hip joints	57
4.6	Amendment of (a) response trajectories with adjustment of equilibrium position and amplitude of the motion for the right hip and left knee, (b) overall locomotion frequency, and (c) pHRI energy transferred through all joints . . . . .	59
5.1	Schematic of the proposed iCPG method for personalized motion planning. . . . .	63
5.2	Variation of pHRI energy and frequency of walking for the weak muscle scenario without RL refinements. . . . .	70
5.3	Variation of pHRI energy due to an RL agent selecting an effective energy to modify the frequency of walking for the weak muscle scenario.	71
5.4	Variations of gait frequency in the absence and presence of RL modification for the strong muscle scenario. . . . .	72
5.5	pHRI energy and walking frequency variations for a user interacting with a lower-limb exoskeleton in the absence of RL modifications. . .	73
5.6	a) Experimental set-up: A 29-year-old neurologically-intact user wearing the Indego lower-limb exoskeleton, b) Desired and actual trajectories generated via iCPGs for the left hip and right knee joints. . . . .	74
5.7	pHRI energy, effective energy, and walking frequency variations for a user interacting with a lower-limb exoskeleton in the presence of RL modifications. . . . .	75
6.1	Schematic of the proposed simulation environment. . . . .	80

6.2	(a) Frequency, (b) RL action, (c) pHRI torque, and (d) modified interaction energy, for weak muscle scenario during the training process in the simulation. . . . .	89
6.3	(a) Frequency, (b) RL action, (c) pHRI torque, and (d) modified interaction energy, for strong muscle scenario during the training process in the simulation. . . . .	91
6.4	Experimental set-up used for empirical experiments with a) first, b) second, and c) third users. . . . .	92
6.5	Actual and desired frequency of the first participant in the a) presence and b) absence of RL modification to the pHRI torque for weak muscle scenario. . . . .	93
6.6	Actual and desired frequency of the first participant in the a) presence and b) absence of RL modification to the pHRI torque for weak muscle scenario. . . . .	93
6.7	Actual and desired frequency of the second participant in the a) presence and b) absence of RL modification to the pHRI torque for weak muscle scenario. . . . .	94
6.8	Actual and desired frequency of the second participant in the a) presence and b) absence of RL modification to the pHRI torque for weak muscle scenario. . . . .	95
6.9	Actual and desired frequency of the third participant in the a) presence and b) absence of RL modification to the pHRI torque for weak muscle scenario. . . . .	96
6.10	Actual and desired frequency of the third participant in the a) presence and b) absence of RL modification to the pHRI torque for weak muscle scenario. . . . .	96
7.1	Structure of the proposed intelligent control strategy with combination of DCM and ACPG schemes for upper body adjustment and trajectory shaping . . . . .	99
7.2	Schematic of the proposed 4-DOF body (4DB) model for DCM analysis	101
7.3	Demonstration of footprints and DCM trajectory and offset during locomotion . . . . .	104
7.4	Experimental set-up: Indego lower-limb exoskeleton in a user study (having a safety harness) during over-ground walking . . . . .	109
7.5	Right and left hip trajectories in the presence and absence of DCM corrections . . . . .	110

7.6	Relative motion of the right and left hips with and without considering DCM corrections . . . . .	111
7.7	Actual and desired end-of-step values of DCM for right and left feet in the presence of DCM correction . . . . .	112
7.8	End-of-step values of DCM in the absence of DCM correction . . . . .	112
7.9	Performance of the position controller in tracking the desired right hip and knee trajectories . . . . .	112
7.10	Control of (a) the amplitude and (b) the frequency of locomotion between their threshold and maximum values using ACPG dynamics . . . . .	114
7.11	Variation of DCM offset below its maximum value . . . . .	114

# Abbreviations

**ACPGs** Adaptable central pattern generators.

**CoM** Center of mass.

**CP** Cerebral palsy.

**CPGs** Central pattern generators.

**DCM** Divergent component of motion.

**HES** Human exoskeleton system.

**iCPGs** Intelligent central pattern generators.

**LIPF** Linear inverted pendulum flywheel.

**MS** Multiple sclerosis.

**pHRI** Physical human robot interaction.

**RL** Reinforcement learning.

**SCI** Spinal cord injury.

# Chapter 1

## Introduction

### 1.1 Motivation

Millions of people all over the world are currently experiencing neurological conditions, including stroke, spinal cord injury, multiple sclerosis, and cerebral palsy [1]. Each year, more than 15 million people in the world experience a stroke [2]. The statistics for SCI show that about 500 thousand people worldwide experience SCI annually [3]. CP is the most common neurological impairment in childhood; one out of every 500 babies is born with this condition [4]. Similarly, MS is another neurological impairment, affecting a large group of people. There are now 2.8 million people worldwide who have MS [5]. Note that the mentioned conditions are only some cases that can result in mobility impairments. Any method that can help people with mobility impairments to have a more independent life will have a considerable impact.

A robotic exoskeleton, inspired by the natural armor of insects, is a sophisticated mechanical device designed to enhance human physical capabilities while reinforcing the body's structure. Crafted from durable materials, these exoskeletons envelop and engage with the user's limbs or core, acting as an external scaffold that facilitates movement, and improves strength, and stability. Exoskeletons integrate sensors and intelligent control systems to seamlessly respond to user movements, ensuring intuitive operation and a harmonious man-machine interaction. Figure 1.1 depicts some of the

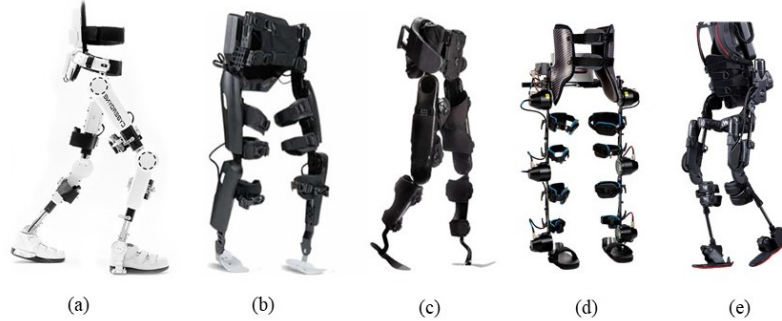


Figure 1.1: Lower-limb exoskeletons developed for assisting/rehabilitating people with neurological impairments: a) HAL, b) ReWalk, c)Indego, d) Exo H3, and e) Ekso GT [13]

commercially available exoskeletons which are specific for lower-limb assistance.

Robotic exoskeletons find diverse applications, from aiding in medical rehabilitation for individuals with mobility impairments to transforming industrial settings by reducing physical strain and boosting productivity. Their potential to enhance human performance and elevate quality of life continues to expand, driven by ongoing advancements in technology. As these innovations unfold, robotic exoskeletons stand as a testament to humanity’s relentless pursuit of innovation and its ability to redefine the boundaries of human potential.

Using lower-limb exoskeletons to assist people with mobility impairments in daily living activities will enhance their quality of life and facilitate rehabilitation. In comparison with traditional physical therapies, powered exoskeletons have the ability to provide frequent, consistent and long-term assistance with minimal engagement of a therapist [6]. This leads to a lower cost and higher efficiency of task execution by accurately rendering the required assistance level to any person with specific neurological conditions. Moreover, precise measurements of human limb movements can be collected for continuous monitoring of the user’s condition by deploying embedded sensors in the exoskeleton’s structure. In this regard, powered lower-limb exoskeletons (such as Indego [7], ReWalk [8], HAL [9], Ekso GT [10], and Exo-H3 [11]) have been invented to assist and rehabilitate individuals with neurological impairments [12].

Despite all of the endeavours in designing and deploying exoskeletons for medical purposes, compliant interaction between the robot and wearer is an important safety issue that still needs to be addressed [14]. In order to facilitate compliant and safe human-robot interaction (HRI), autonomous strategies are required to be investigated for generating motion trajectories. Note that, trajectories are joint angles and velocities that dictate the movement of the exoskeleton’s mechanical joints, such as those at the hip, knee, and ankle. Most commercial exoskeletons have been programmed to track pre-recorded trajectories to ensure repeatability and controllability of the movements. Therefore, next generations of the exoskeletons need to focus on the improvement of software to refine gait pattern based on the HRI. For that goal we have devoted our research in development of intelligent locomotion planning methods to

- Provide an approach that can facilitate real-time modifications in the exoskeleton’s gait
- Make the gait trajectories adaptive with the user’s target locomotion
- Adjust upper-body position and enhance postural stability

## **1.2 Contributions of this research**

### **1.2.1 Provide an approach that can facilitate real-time modifications in the exoskeleton’s gait**

The biological central pattern generator is a neural circuit located in the spinal cord and brainstem responsible for generating rhythmic motor patterns such as walking, swimming, and breathing, without requiring constant input from the brain. In humans, the CPG plays a crucial role in coordinating the complex sequence of muscle activations and movements involved in locomotion. Research suggests that the human CPG receives sensory feedback from various sources, including proprioceptive signals from muscles and joints, cutaneous feedback from the skin, and vestibular

input related to balance and orientation. These sensory signals provide important feedback to the CPG, influencing the timing and intensity of muscle activations during locomotion. Understanding the input signals to the human CPG is essential for elucidating the mechanisms underlying motor control and for developing therapies for movement disorders and rehabilitation strategies [15].

In robotics, Central Pattern Generators (CPGs) are modeled after their biological counterparts and implemented to generate rhythmic joint trajectories for robotic systems, particularly in tasks requiring repetitive or cyclic motion, such as legged locomotion or robotic swimming. By mimicking the principles of biological CPGs, these artificial systems can produce coordinated and stable rhythmic patterns of movement, enabling robots to walk, run, swim, or perform other locomotion tasks autonomously and efficiently [16]. While CPGs present a promising avenue for motion planning in lower-limb exoskeletons, a significant drawback lies in their lack of adaptability to human users.

Studying human walking, one can notice that there are considerable differences in walking patterns among different people. Additionally, even for one person, can vary within one day and over time for a variety of reasons, including aging, fatigue, load-carrying, etc. [17]. Using a pre-defined trajectory is one of the significant shortcomings of commercially available exoskeletons, limiting the willingness toward using these systems. To provide comfort for the exoskeleton users, the systems need to be automatically adapted to the user’s locomotion pattern. To address this challenge, we proposed the adaptable central pattern generators (ACPGs) method [18, 19].

In this study, the adaptable CPG structure was considered for modulating and controlling a lower-limb exoskeleton that results in a compliant and safe physical interaction with the human. The proposed ACPG dynamics had adaptable online features to update the gait characteristics in response to the pHRI torque. To estimate the pHRI torque, we introduced two distinct algorithms: one based on a nonlinear disturbance observer and the other utilizing a deep neural network (NN).

The contributions of these studies encompass:

- For the first time, we introduced adaptable CPGs which has the capability to refine exoskeletons gait trajectory in response to the pHRI torque while walking. It's important to note that the proposed algorithm isn't confined to a particular exoskeleton model but can be applied universally across various exoskeletons with differing degrees of freedom (DOFs) in their motion planning.
- The proposed ACPGs have the ability to adjust walking velocity, step length, and even the starting and ending positions for each joint of the exoskeleton, such as the hip and knee.
- For the first time, we introduced a nonlinear disturbance observer which aims to enhance the stability of exoskeletons concerning the uniform ultimate boundedness (UUB) of both trajectory tracking and pHRI estimation errors. Unlike previous disturbance observer designs for exoskeletons, which neglected the stability aspect of the controlled system, this approach prioritizes stability considerations to ensure robust performance.

### **1.2.2 Make the gait trajectories adaptive with the user's target locomotion**

The ACPGs mentioned earlier have the potential to address the adaptability challenge in exoskeleton motion planning, provided that the user-specific ACPG parameters are accurately identified, and the user's physical interaction behavior remains relatively stable over time. However, these two conditions impose constraints on ACPGs in delivering personalized locomotion trajectories. In simpler terms, individuals using exoskeletons must familiarize themselves with and adjust to the dynamics of ACPGs to modify their gait pattern, including factors such as frequency and amplitude of gait, to align with their preferences.

In order to address this challenge a reinforcement learning-based approach was introduced for exoskeleton motion planning. The reinforcement learning (RL) algorithm adjusted the user’s physical interaction with the exoskeleton. Put simply, if the user’s physical interaction wasn’t sufficient to achieve the desired gait within a reasonable timeframe, the proposed RL algorithm amplifies the interaction to expedite the process. Conversely, if the user’s physical interaction exceeds the necessary threshold for the ACPGs to achieve the target gait, the RL component reduces this interaction to prevent excessive oscillation around the desired values. Consequently, the integration of RL with ACPGs, referred to as intelligent CPGs (iCPGs), effectively resolves the personalization challenge in exoskeleton motion planning. Followings are the major contributions of these studies:

- We introduced a novel framework that merges RL with ACPGs for adaptive motion planning tailored to human users. This innovative algorithm addresses a significant limitation of ACPGs in accommodating users with varying levels of muscle strength.
- We have developed a simulation environment for the first time, which replicates human behavior during physical interactions with exoskeletons to alter gait trajectories using ACPGs. This environment is valuable for training RL algorithms or gathering data for training various supervised learning algorithms.

### **1.2.3 Upper-body position adjustment and postural stability**

Refining exoskeletons’ gait to be close to users’ walking patterns is integral to making these systems suitable for assistance/rehabilitation applications. However, although the ACPG method can address this issue, the algorithm also needs to monitor postural stability while reshaping the walking pattern. To this end, we introduced the divergent component of motion (DCM) for the lower-limb exoskeletons [20]. While walking with the exoskeleton, the DCM analysis monitors the position and velocity

of the exoskeleton’s center of mass (CoM) and adjusts the upper-body position to maintain postural stability. Therefore, the exoskeleton had the authority to ensure postural stability and viability of locomotion while the user reshape their gait pattern via pHRI.

In this project, an intelligent control strategy was developed and tested for lower-limb exoskeletons by introducing a new integration of DCM and CPG schemes to facilitate both posture stability and adaptable locomotion planning. The DCM analysis, which was previously developed for bipedal locomotion of humanoid robots, was extended and generalized for the human-exoskeleton system (HES) for the first time. To this end, the linear inverted pendulum flywheel (LIPF) model was replaced with a new 4-DOF body (4DB) model to address the following issues: (a) In the LIPF model, the CoM of the whole system is considered to be at the middle of the line that connects the right and left hips. However, for humans, the CoM is mostly higher than this level and can be different for users based on their body characteristics. Taking the 4DB model into account, the CoM of combination HES can be upper or lower than this level at any point. (b) Due to the attachment of exoskeleton to the human body, the mechanical properties (e.g., moment of inertia and mass) for different segments of the HES can be significantly different for various wearers. Using the proposed 4DB model, these dynamic parameters can be personalized for each user to make the locomotion control strategy case-specific.

Using the proposed DCM analysis, a hip joint correction was generated in real-time to amend the trunk position and consequently adjust the DCM on its desired value at the end of each step. The introduced ACPGs were used to shape joint trajectories in response to the human interaction torques by regulating the step length and velocity of walking. In addition, the ACPG dynamics were designed to guarantee that gait velocity is less than the maximum stable velocity of walking and the output trajectories are within the feasible movement ranges of the exoskeleton joints. Accordingly, the commands generated by the DCM and ACPG schemes were combined

to autonomously facilitate locomotion trajectories compatible with the user’s desired gait and ensure the viability of walking through the postural stability. summary of the main contributions of this study are as follows:

- We have introduced an algorithm for the first time to monitor and improve postural stability in exoskeletons. This algorithm is designed to work seamlessly with the previously introduced ACPGs, adjusting the upper-body position in response to modifications in the gait trajectory made via ACPGs.
- The proposed algorithm extends an existing model in bipedal robotics and introduces a new model that considers the body characteristics of exoskeleton users, such as limb weight and inertia. This incorporation is essential for studying postural stability in lower-limb exoskeletons.

The concepts of amplitude, frequency, and phase in walking will be consistently referenced throughout the thesis in all chapters. Amplitude indicates the range of motion for individual joints, such as the hip and knee, with higher values reflecting a broader range of motion and resulting in larger steps. Frequency measures the number of steps taken within a given timeframe, where higher frequencies correspond to faster walking speeds. Phase pertains to the coordination of movements among different joints in the exoskeleton, such as the synchronization between the right and left hips and knees.

### **1.3 Outline of this dissertation**

The subsequent chapters of this dissertation are structured as follows: In Chapter 2, an exploration of literature regarding motion planning algorithms for exoskeletons, methods for estimating pHRI torque, RL methods for exoskeletons, simulation environments for physical human-exoskeleton interaction, and postural stability in bipedal locomotion is undertaken. Chapter 3 introduces the first generation of ACPGs with the capability of adjusting step length and walking velocity. Additionally, a nonlinear

disturbance observer-based algorithm for estimating pHRI torque is presented in this chapter. Chapter 4 unveils our latest generation of ACPGs, which boasts the ability to update step length, walking velocity, and the start and end positions of each joint during walking. Safety terms have also been incorporated into this version of ACPGs to ensure that gait parameters remain within a safe range. In Chapter 5, the integration of RL with ACPGs is introduced, resulting in iCPGs that generate personalized locomotion trajectories. Chapter 6 serves as an extension of Chapter 5, addressing the incapability of the previous RL agent to decrease pHRI, particularly in scenarios of strong muscle engagement, further elaborated in Chapter 6, for facilitating personalized locomotion planning. Chapter 7 introduces a novel DCM structure designed to enhance postural stability for exoskeleton users. Finally, in Chapter 8, concluding remarks and future directions for this research are discussed.

# Chapter 2

## Literature review

### 2.1 Adaptive locomotion planning

Different nonlinear methods were proposed in the literature for high-level motion planning of robotic systems, including dynamic movement primitives (DMPs) and central pattern generators (CPGs). DMPs were defined in Schaal et al. [21] as a combination of several differential equations to mimic the stream of movements captured from humans and animals. Researchers employed DMPs for locomotion trajectory generation and position/torque control of powered lower-limb exoskeletons [22], [23], [24]. Yuan et al. [22] used a point-attractor DMP structure for the trajectory shaping of hip and knee joints, augmented by reinforcement learning (RL) to update the DMP parameters with the purpose of minimizing the error between the target and actual trajectories [22]. With a similar objective, the locally weighted regression (LWR) method was suggested in Qui et al. [23] to regulate the weights of basis functions in the DMP dynamics. Huang et al. [24] developed another DMP structure by embedding the HRI torque in the point-attractor DMP dynamics to shape the pilot locomotion trajectory online.

Among the strategies suggested for motion planning of lower-limb exoskeletons and bio-inspired robots, the CPG is an appropriate one because of its inherent feature of producing time-continuous rhythmic motions synchronized for adjacent joints similar to natural bipedal locomotion. CPGs are structured as connected modules that are

able to generate oscillatory movements with organized patterns in response to non-periodic inputs [16]. The functional capability of CPGs in generating fluctuating activities has been studied for the trajectory shaping of lower-limb exoskeletons in previous research studies [20, 25–27]. The CPG parameters were optimized by a genetic algorithm in Schrade et al. [25] for steady-state locomotion with a lower-limb exoskeleton implemented by a torque controller, where the knee stiffness was adjusted by activating stiffening CPG units. Gui et al. [26] benefited from CPGs and admittance control to provide flexibility in terms of the measured electromyography (EMG) signals while tracking pre-specified motion trajectories for the knee and hip joints. A robotic rehabilitation system was developed by incorporating functional electrical stimulation (FES) and torque control for a knee exoskeleton [27], where CPGs generated fixed rhythmic movements for both the FES feedforward controller and the feedback torque controller. Due to the tight coupling between the wearer and exoskeleton, it is essential to take HRI signals into account for CPG-based motion planning, which has not been addressed in most previously proposed high-level control strategies.

## 2.2 pHRI estimation methods

Obtaining the interaction torque between the human and exoskeleton is a pivotal point and a practical challenge to design appropriate control policies responsive to human physical behavior to enhance safety and compliance. To this end, two kinds of sensory information acquisition techniques have been used in the literature to estimate the human torque; embedding force/torque sensors in the exoskeleton structure and attaching electromyography (EMG) sensors to the human body. Electromechanical force/torque transducers and strain gauges mounted between the human and exoskeleton can not isolate the active portion of the human’s physical effort [28]. In other words, sensory data contains undesired components related to the human body’s gravity, friction, inertia, and also the passive portion of the muscles, which

makes the extraction of the human active torque out of data difficult [29, 30].

On the other hand, EMG as a biological signal represents the activity level of the muscle, which is effective in identifying the human motion intention. As the EMG signal is transferred through neural pathways, it can be detected before muscle action and motion generation. Accordingly, this signal has been utilized in intelligent control of assistive exoskeletons for estimation of the active HRI torque [30, 31]. In several studies, musculoskeletal models have been employed to estimate the active portion of the muscle force and determine the exerted torque on the corresponding joint [32–34]. Teramae et al. [32] have proposed a linear proportional model (LPM) to estimate the human active torque on the elbow joint based on the EMG activity of biceps and triceps muscles during the interaction with a robot. A model predictive control (MPC) approach was taken into account to derive deficient joint torque needed for tracking predefined desired trajectories considering the EMG-based estimation of the human torque [32]. Ao et al. [33] utilized a Hill-type neuromusculoskeletal model (HNM) for the tibialis anterior and gastrocnemius muscles in the actuation of the ankle joint, which resulted in more accuracy in EMG-based torque estimation compared to the LPM’s outcome. The obtained torque was amplified by a one-DOF exoskeleton to assist the wearer in a tracking task [33]. In a similar study [34], a radial basis function neural network (RBFNN) was trained to update the activation coefficient of the HNM in order to enhance the accuracy of human torque estimation in the presence of the time-varying EMG features [34].

Although model-based torque estimation methods can provide reasonable accuracy, identifying the corresponding model parameters necessitates a high volume of mathematical calculations in both offline and online data processing modes. In this regard, neural networks (NNs) have been employed for torque estimation, dynamic identification, trajectory shaping, and gait phase estimation for lower-limb exoskeletons in most of the recent studies. This is due to the fast training rate and the model-free aspect of learning using NN structures, making them desirable options for

distinguishing the underlying relations between various input and output data.

An individualized motion planning was developed in Wu et al. [35] based on NNs in which body parameters and target walking speed were fed to a Gaussian process regression to identify and classify gait characteristics [35]. Two radial basis function neural networks (RBFNNs) were suggested to approximate passive and active HRI torques in Gui et al. [30]. In this work, a passive torque model was presented and EMG signals were employed for training the RBFNNs to estimate the active human torque [30]. Kang et al. [36] proposed an NN-based strategy to estimate the locomotion phase based on the hip joint angle and thigh inertial measurement unit (IMU) data as the inputs and the heel contact information as the output for offline training of the NN [36]. In a similar approach, a nonlinear autoregressive network with exogenous inputs (NARX) was utilized to capture the ankle joint dynamics based on the collected data of a typical walking [37]. The EMG activity of shank muscles and knee joint position were considered the inputs, and the ankle joint position as the NARX structure’s output to be estimated [37]. In another study, NARX was employed in the estimation of the foot angular position for the purpose of controlling an active prosthetic [38]. The gait data from seven able-bodied people were used in the training process and the angular velocity of the shank was considered as the input of the network [38].

## 2.3 Reinforcement learning algorithms for exoskeletons

The inherent characteristic of reinforcement learning (RL) is learning while interacting in real-time making it a good fit for personalization applications. The method proposed by Shen *et al.* [39] modelled the human-exoskeleton system as a leader-follower system and used an RL-based control algorithm to adjust the walking assistant level. Huang *et al.* [40] used a mass-spring-damper model to estimate physical interaction between humans and exoskeletons, and they used RL to learn the spring and damper

coefficients in the model. They employed the estimated interaction in high-level control of an exoskeleton [40] (the impedance model changes the trajectory generated by dynamical movement primitives; DMPs). RL has also been used in manipulating motion planning algorithm parameters by Zhang *et al.* [41]. Here, the RL algorithm adjusted the gain in trajectory generated by DMPs while taking the stability of the system into consideration [41].

Among RL algorithms used for robotic applications, deep deterministic policy gradient (DDPG) has been commonly used, including control of a biped robot [35] and motion control of a six-degree-of-freedom arm robot [42]. However, DDPG suffers from overestimating future rewards, and optimal policy convergence [43]. The twin delayed deep deterministic policy gradient (TD3) addresses these limitations. TD3 is a model-free, off-policy, actor-critic algorithm used for online learning in an environment with continuous action spaces. Thus, TD3 is an improvement over DDPG, and related algorithms by increasing its robustness through clipped double-Q learning and decreasing the likelihood of Q-function exploitation via policy smoothing [43, 44].

## 2.4 Exoskeleton simulating environments for training RL agents

Despite the potential of personalized trajectory generation, the use of RL in exoskeleton control raises concerns about the stability and safety of the agent’s actions [45, 46]. RL agents are known to explore different actions in order to learn, which can lead to unpredictable and potentially dangerous behavior. This holds particular significance within the realm of exoskeletons, as any instability or unsafe actions pose significant risks to the well-being of the human user [47]. A widely adopted approach, that is extensively documented in the literature, involves leveraging simulation environments. These simulation environments serve as the foundational step in incorporating RL within exoskeleton control systems, ensuring that algorithms are thoroughly prepared for experimental testing. A method proposed by Peng *et al.* [48]

used a simulation environment to check whether the RL controller is adaptable to the disturbance or not. A 2-DOF manipulator was implemented in the simulation with an RL controller, and white noise was added to the controller as a disturbance. Rose et al. [49, 50] used the OpenSim API platform [51] to simulate RL for exoskeleton application. OpenSim-RL is the simulation environment designed for simulating RL as a controller of 3D objects. The simulation environment used in Huang et al. [52] was for testing the performance of the controller on a single DOF robot resembling 1-DOF in an exoskeleton robot. Dong et al. [53] designed a simulation environment where exoskeleton robots were able to interact with the environment where the controller manipulated the trajectories for the robot’s motion control.

## 2.5 Postural stability for bipedal locomotion

Divergent component of motion (DCM) analysis was employed in trajectory generation for the center of mass (CoM) in bipedal locomotion of humanoid robots [54–56]. In this method, a linear inverted pendulum (LIP) model was used to represent the bipedal movement and the divergent part of the LIP dynamics was introduced as the DCM [57]. Considering this model, two strategies have been used to overcome the disturbance applied during bipedal locomotion, including the adjustments of the step time and length that affected the frequency and amplitude of the gait, respectively [58]. However, these strategies are not applicable to the exoskeleton applications since the gait parameters (e.g., amplitude and frequency of walking) are desired to be regulated based on the wearer’s intention. Studies have designed optimal controllers to combine both of these adjustment strategies in order to realize a stable walking for bipedal robots. In Khadiv et al. [58] and Jeong et al. [59], a higher cost was allocated to the regulation of the foot landing position in the objective function to keep the preplanned foot-print as much as possible. Jeong et al. [56] employed a linear inverted pendulum flywheel (LIPF) model to extend the DCM adjustment strategy and introduce a hip strategy (applying torque to the upper-body) for that

purpose. Similar to the previous studies, an optimization approach was suggested to minimize the error between desired and actual DCM by regulation of the ankle and hip trajectories in addition to the step size and walking speed [56].

Englsberger et al. [60] presented an enhanced centroidal moment pivot (eCMP) and virtual repelling points to extend the DCM trajectory in 3D space. The DCM dynamics utilized to determine the required force for a stable bipedal walking over uneven ground and to generate a smooth path for the eCMP point [60]. In a similar approach 3D DCM planning [61], the foot landing position was controlled and the required ground reaction force (GRF) was determined based on a viscoelastic model for the foot contact. It is worth mentioning that DCM adjustment has not been utilized for the posture stability of users wearing lower-limb exoskeletons so far.

# Chapter 3

## Autonomous Locomotion Trajectory Shaping and Nonlinear Control for Lower-Limb Exoskeletons

### 3.1 Introduction

Millions of people all over the world are currently experiencing neurological impairments, including stroke, spinal cord injury, multiple sclerosis, and cerebral palsy [1]. Assisting these individuals in daily living activities by robotic systems (e.g., exoskeletons) will enhance their quality of life, and facilitate rehabilitation. In comparison with traditional physical therapies, powered exoskeletons have the ability to provide frequent, consistent and long-term assistance with minimal engagement of a therapist [6]. This leads to a lower cost and higher efficiency of task execution by accurately rendering the required assistance level to any subject with specific neurological conditions. Moreover, precise measurements of human limb movements can be collected for continuous monitoring of the user's condition by deploying embedded sensors in the exoskeleton's structure.

Due to the inability of passive orthoses to assist people with movement disorders to realize an appropriate upright walking, powered lower-limb exoskeletons (such as Indego [7], ReWalk [8], and GEMS [62]) have been designed and fabricated as an

alternative solution [12]. Although these developed exoskeletons are now deployed in some clinical settings to assist and rehabilitate people [12], a compliant interaction between the robot and wearer is an issue that still needs to be resolved [63]. To address this challenge, industrial exoskeletons such as Honda SML [64], Samsung Electronics [65], and Keeogo [66] have benefited from adaptive strategies to shape the exoskeleton’s walking trajectories based on user-specific gait patterns. However, these exoskeletons have not utilized any online estimation of pHRI torque in locomotion planning and they were designed for assisting/rehabilitating only one single joint (hip or knee). Control strategies for lower-limb exoskeletons play the most critical role in providing safe and comfortable interaction between the wearer and the robot, which are divided into high-level and low-level categories. The motion trajectory and sequence of locomotion are planned at the high level (based on the user’s intention and motor capacity) and are implemented at the low level using position, force or impedance controllers. To date, some studies have developed control schemes in both levels, while others focused only on the low-level control design by employing pre-specified reference gait trajectories [30, 67, 68].

In the present chapter, a novel nonlinear autonomous control strategy is proposed to realize compliant, safe and case-specific physical human-robot interaction (pHRI) for lower-limb exoskeletons by integrating ACPGs and a time-varying bounded-gain adaptive (TBA) disturbance observer. At the high level of this strategy, new ACPGs are investigated to shape rhythmic locomotion trajectories in real-time based on the interaction between the human (wearer) and exoskeleton. The initial gait trajectory is extracted from typical gait data of able-bodied individuals and mathematically represented by an eight-term expansion of the Fourier series. For the first time, the nonlinear ACPGs’ dynamics is augmented by pHRI torque estimation in order to update the amplitude, frequency, and phase of walking based on the wearer’s intention (physical behavior). Amplitude denotes the extent of motion for individual joints, such as the hip and knee. Higher amplitude values indicate a broader range of mo-

tion for the joints, leading to larger steps. Frequency quantifies the number of steps taken within a specific timeframe, with higher frequencies correlating to quicker walking speeds. Phase refers to the synchronization of movements among various joints in the exoskeleton, such as the right and left hips and knees. A new multi-layer TBA disturbance observer is formulated to estimate pHRI torque to be employed in (a) the low-level torque controller for motion tracking, and (b) the high-level ACPG-based locomotion planning for rendering human flexibility. The stability of this autonomous pHRI system, and the uniform ultimate boundedness (UUB) of trajectory tracking error and torque estimation error are guaranteed through a comprehensive Lyapunov analysis. The main contributions of this strategy over previous ones can be summarized as:

- The pHRI torque is employed in the defined nonlinear ACPG dynamics to generate adaptable reference trajectories for the gait cycles. Previous CPG-based controllers [25–27, 69, 70] for lower-limb exoskeletons have not taken pHRI torque into account in their CPG structures. This feature of the proposed strategy makes the exoskeleton significantly compliant with the wearer’s physical interaction and enhances safety by raising her/his high-level authority in motion planning.
- The nonlinear multi-layer TBA disturbance observer is designed to facilitate exoskeletons’ stability regarding the UUB of both tracking and estimation errors. Previous disturbance observer designs have not taken into account the stability of the controlled system [71]. Other disturbance observers [72], [73] have been developed for a single-joint (knee) exoskeleton with a scalar dynamic model and fixed adaptation gains that need to be determined through trial-and-error. In this study, a TBA disturbance observer is developed for multi-DOF exoskeletons with a nonlinear coupled matrix formulation. Moreover, a nonlinear adaptation is defined for automated online regulation of the time-varying bounded gain in

the observer’s structure to facilitate smooth torque estimation. In comparison with previous observers [72], [73], a first-order dynamics is also employed in this scheme for intermediate variables of the combined exoskeleton-human limb system to diminish undesired noise in these signals and avoid reflecting it in the torque observation.

The rest of this chapter is organized as follows. The nonlinear dynamic model of the lower limb exoskeleton and the structure of the ACPGs (high-level control) are presented in Sec. 3.2. The proposed TBA disturbance observer, the low-level torque control strategy and the closed-loop system’s stability are explained in Sec. 3.3. The experimental evaluations of the developed autonomous control scheme are presented in Sec. 3.4 and discussed in Sec. 3.5. The concluding remarks are provided in Sec. 3.6.

## 3.2 Exoskeleton Dynamics and Adaptive CPG-Based Online Trajectory Shaping

The nonlinear dynamics of a lower-limb exoskeleton shown in Fig. 3.1 with  $n$  joints together with the human user is given as

$$M_q(q)\ddot{q} + C_q(q)\dot{q} + G_q(q) = \tau_{mot} + \tau_{hum} \quad (3.1)$$

where  $q$  is the vector of exoskeleton joints’ (right and left hips and knees) position,  $M_q(q)$  is the inertia matrix,  $C_q(q)$  is the matrix of Coriolis, centrifugal and damping terms,  $G_q(q)$  is the vector of gravitational torques,  $\tau_{con}$  is the exoskeleton’s motor torque, and  $\tau_{hum}$  is the human torque generated by his/her muscles’ contractions.

*Property 1:* The inertia matrix  $M_q$  is positive definite and uniformly bounded such that there are a min-bound on the minimum singular value and a max-bound on the maximum singular value of this matrix [74]:

$$0 < M_1 \leq \|M_q\| \leq M_2 < \infty \quad (3.2)$$

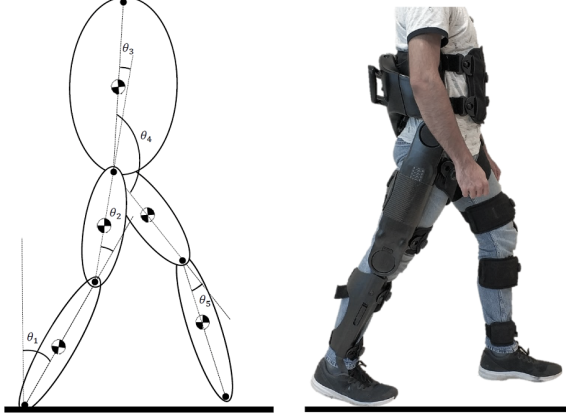


Figure 3.1: The employed lower-limb exoskeleton (Indego by Parker Hannifin Corporation), and joint consequences from the stance leg to the swing one based on pinned (point-feet) model

where  $M_1$  and  $M_2$  are the uniform bounds, and  $\|\cdot\|$  is the induced norm. The matrix  $\dot{M}_q - 2C_q$  is skew symmetric, and the left side of (3.1) can be linearly parameterized [75, 76] as

$$M_q(q)\phi_1 + C_q(q)\phi_2 + G_q(q) = Y_q(\phi_1, \phi_2, q, \dot{q})\theta_q \quad (3.3)$$

in which  $Y_q$  is the regressor matrix defined in terms of known variables including  $\phi_1$  and  $\phi_2$ , and  $\theta_q$  is the vector of unknown parameters of the robot dynamics.

For the high-level control of the exoskeleton, a learning-based locomotion path generation is developed by defining an ACPG, as illustrated schematically in Fig. 3.2. To this end, human physical behavior is taken into account during the motion and interaction with the exoskeleton. In order to interpret this behavior, the estimated pHRI energy is defined for each joint  $i$  as follows:

$$E_i(t) = \int_0^t \tau_{HRI_i}(t) \dot{q}_i(t) dt \quad (3.4)$$

where  $\dot{q}_i(t)$  is the velocity of the joint  $i = 1, \dots, n$ , and  $\tau_{HRI_i}(t)$  is the estimated value of the human torque on this joint of the exoskeleton after applying a dead-zone function:

$$\tau_{HRI_i} = \begin{cases} \hat{\tau}_{hum_i} - \tau_{thr_{pos}} & \text{for } \hat{\tau}_{hum_i} > \tau_{thr_{pos}} \\ 0 & \text{for } \tau_{thr_{neg}} \leq \hat{\tau}_{hum_i} \leq \tau_{thr_{pos}} \\ \hat{\tau}_{hum_i} - \tau_{thr_{neg}} & \text{for } \hat{\tau}_{hum_i} < \tau_{thr_{neg}} \end{cases} \quad (3.5)$$

in which  $\tau_{thr_{pos}}$  and  $\tau_{thr_{neg}}$  are the positive and negative thresholds of this dead-zone for the estimated human torque  $\hat{\tau}_{hum_i}$ . In other words, if human users apply any torque larger than these thresholds, they will be able to modify the locomotion trajectory's characteristics as explained below.

Suppose that both  $\tau_{HRI_i}$  and  $\dot{q}_i$  in (3.4) are either positive or negative. In this case, the operator applies a torque/force in the same direction as the joint's motion by injecting energy into the system ( $\dot{E}_i(t) > 0$ ) to accelerate this movement. On the other hand,  $\dot{E}_i(t) < 0$  implies dissipating energy by opposing torque/force of the human user with respect to the motion. Accordingly, the proposed ACPG dynamics for the phase  $\theta_i(t)$ , frequency  $\omega(t)$  and amplitude  $\mu(t)$  of locomotion trajectories is formulated as a coupled system of nonlinear oscillators as

$$\begin{aligned}\dot{\theta}_i(t) &= \omega(t) + \sum_{j=1}^{m_i} \gamma_{ij}(\dot{E}_i - \dot{E}_j) + \sum_{j=1}^{m_i} v_{ij} \sin(\theta_i(t) - \theta_j(t) - \phi_{ij}) \\ \ddot{\omega}(t) &= \beta_\omega \left( \frac{\beta_\omega}{4} (\Omega + \sum_{k=1}^n \psi_k E_k - \omega(t)) - \dot{\omega}(t) \right) \\ \ddot{\mu}(t) &= \beta_\mu \left( \frac{\beta_\mu}{4} (A + \sum_{k=1}^n \lambda_k E_k - \mu(t)) - \dot{\mu}(t) \right)\end{aligned}\quad (3.6)$$

in which  $m_i$  is the number of adjacent joints to the joint  $i$ , and  $n$  is the number of all joints.  $\gamma_{ij}$ ,  $\psi_k$  and  $\lambda_k$  are constant factors of pHRI energy effect on phase, frequency and amplitude variations of locomotion, respectively.  $v_{ij}$ ,  $\beta_\omega$  and  $\beta_\mu$  are other constant parameters of this dynamics. The desired trajectory for the joint  $i$  of the exoskeleton is defined as

$$q_{d_i}(t) = \mu(t) \left( a_{i_0} + \sum_{l=1}^{N_i} (a_{i_l} \cos(l\theta_i(t)) + b_{i_l} \sin(l\theta_i(t))) \right) \quad (3.7)$$

where  $a_{i_l}$  and  $b_{i_l}$  are the coefficients of Fourier series (with  $N_i$  terms) to initially match the desired trajectory of the joint  $i$  to a typical walking trajectory, as demonstrated in Fig. 3.2. The amplitude and phase of these oscillatory motions are updated in real-time by  $\mu(t)$  and  $\theta_i(t)$  obtained from (3.7). Note that the generated reference trajectory in (3.7) is continuous in time and differentiable, which are beneficial fea-

tures for the control scheme presented in the next section. To perceive the proposed adaptive autonomous trajectory shaping (3.6) and (3.7), the following characteristics can be mentioned.

A coupling between all joints is facilitated, having the same principal frequency of  $\omega(t)$  to synchronize generated locomotion trajectories. The scaling factor of these trajectories is specified to be the same  $\mu(t)$ , while the initial coefficients of the Fourier series  $a_{i_l}$  and  $b_{i_l}$  for each joint  $i$  are determined from typical experimental data. This mutual adjustment of  $\omega(t)$  and  $\mu(t)$  for all joints guarantees synchronized multi-DOF locomotion and provides the appropriate overground motion of the feet in the Cartesian space.

The pHRI energy  $E_k(t)$  injected to or dissipated from the system by the wearer through each joint  $k$  of the exoskeleton can affect the frequency  $\omega(t)$  and the amplitude coefficient  $\mu(t)$  of locomotion trajectory. Based on this feature, human users can physically demonstrate their compliance or resistance by applying accelerating or decelerating torques with respect to the implemented gait trajectories of all  $n$  joints of the exoskeleton. This effect can be regulated by  $\psi_k$  and  $\lambda_k$  as the authority factors of each joint torque over the generation of the overall gait pattern.

The other adjustable coupling in the proposed ACPG-based trajectory shaping is the online variation of phase lead/lag between adjacent joints. The difference between the rate of exerted energy by the human user on two adjacent joints ( $\dot{E}_i - \dot{E}_j$ ) will affect the phase difference between these joints ( $i$  and  $j$ ). In this regard, the human behavior on accelerating/decelerating the motion of one joint  $i$  with respect to its adjacent joints is perceived by the pHRI energy estimation  $E_i$ . Another harmonic term for connecting ACPGs correspond to adjacent joints is facilitated by  $\sin(\theta_i(t) - \theta_j(t) - \phi_{ij})$  based on the scheme presented in [77]. The coefficients  $\gamma_{ij}$  and  $v_{ij}$  specify the gains of this synchronized phase variation for each joint.

Regarding the requirement of torque estimation  $\hat{\tau}_{hum_i}$  in the proposed ACPG formulations (3.4), (3.5) and (3.6), a new adaptive disturbance observer is defined in the

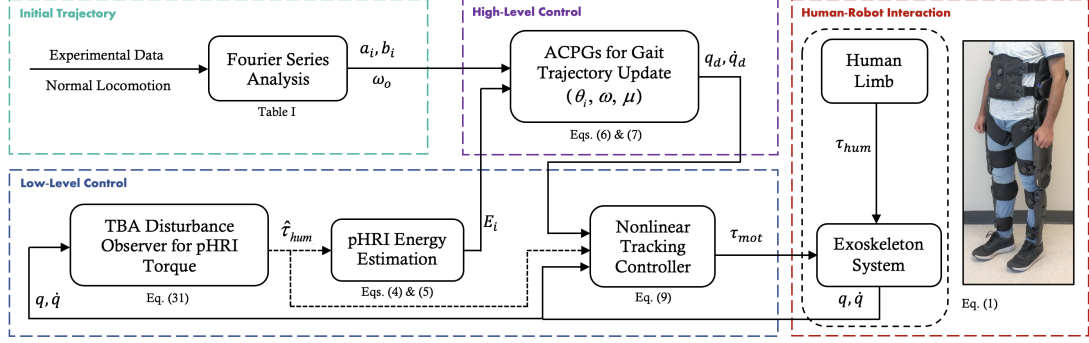


Figure 3.2: Autonomous two-level control strategy for lower-limb exoskeletons: Adaptive CPG-based gait trajectory update in high-level and nonlinear torque control in low-level, employing an adaptive HRI torque observer

next section together with a nonlinear low-level controller for trajectory tracking.

### 3.3 TBA Disturbance-Observer-Based Control

In this section, an autonomous observer-based strategy is developed for the low-level controller of the exoskeleton. In this strategy, the human interaction torque is estimated via a multi-layer TBA disturbance observer in order to be employed in the high-level gait generation (3.4) and (3.6). At the same time, this pHRI torque estimation is also utilized in the low-level control law for tracking the generated locomotion trajectory, as seen in Fig. 3.2.

#### 3.3.1 Controller and Observer Design

For the purpose of controlling motor torque and estimating HRI torque, the tracking error  $e_q$ , its dynamics  $\epsilon_q$  and the corresponding auxiliary variable  $\dot{q}_r$  are defined:

$$\begin{aligned}
 e_q(t) &= q(t) - q_d(t) \\
 \epsilon_q(t) &= \dot{e}_q(t) + \kappa_1 e_q(t) \\
 \dot{q}_r(t) &= \dot{q}_d(t) - \kappa_1 e_q(t)
 \end{aligned} \tag{3.8}$$

The proposed nonlinear trajectory tracking control law for the exoskeleton's motor torque is formulated as

$$\tau_{mot} = M_q(\ddot{q}_r - \kappa_2 \epsilon_q) + C_q \dot{q}_r + G_q - \hat{\tau}_{hum} \quad (3.9)$$

in which  $\kappa_1$  and  $\kappa_2$  are positive constant gains. Substituting the proposed controller (3.9) in the user-exoskeleton dynamics (3.1) leads to the following closed-loop dynamics:

$$M_q \dot{\epsilon}_q = -\kappa_2 M_q \epsilon_q - C_q \epsilon_q - \tilde{\tau}_{hum} \quad (3.10)$$

where  $\tilde{\tau}_{hum} = \tau_{hum} - \hat{\tau}_{hum}$  is the pHRI torque estimation error. Now, the multi-layer TBA disturbance observer is formulated in a couple of steps for estimation of  $\hat{\tau}_{hum}$ . The final adaptation law is proposed in (3.31), and required intermediate variables, their boundedness and mathematical derivations are mentioned as follows. Considering a state variable as  $z_1 = \epsilon_q$ , the dynamics (3.10) can be presented as

$$\dot{z}_1 = \Psi(z_1, \hat{\tau}_{hum}) + \chi \tau_{hum} \quad (3.11)$$

in which

$$\Psi = -\kappa_2 z_1 + M_q^{-1} C_q z_1 - M_q^{-1} \hat{\tau}_{hum}, \quad \chi = M_q^{-1} \quad (3.12)$$

Then, the filtered variables  $z_{1f}$ ,  $\Psi_f$  and  $\chi_f$  are defined, having  $\xi > 0$ , as

$$\begin{aligned} \xi \dot{z}_{1f} + z_{1f} &= z_1, & z_{1f}(0) &= 0 \\ \xi \dot{\Psi}_f + \Psi_f &= \Psi, & \Psi_f(0) &= 0 \\ \xi \dot{\chi}_f + \chi_f &= \chi, & \chi_f(0) &= 0 \end{aligned} \quad (3.13)$$

*Lemma 1:* According to the system dynamics (3.11) and the filters (3.13), the manifold  $[(z_1 - z_{1f})/\xi - \Psi_f - \chi_f \tau_{hum}]$  remains bounded for any finite positive value of  $\xi$  and converges to zero if  $\tau_{hum}$  is constant or  $\xi \rightarrow 0$ .

**Proof.** Considering (3.13), the filter  $1/(\xi s + 1)$  is applied on (3.11) as

$$\frac{1}{\xi s + 1}[\dot{z}_1] = \frac{1}{\xi s + 1}[\Psi] + \frac{1}{\xi s + 1}[\chi \tau_{hum}] \quad (3.14)$$

Based on (3.13) and the swapping lemma [78] for  $[1/(\xi s + 1)][\chi \tau_{hum}]$ , one can rewrite (3.14) as

$$\frac{z_1 - z_{1f}}{\xi} = \Psi_f + \chi_f \tau_{hum} + v_1 \quad (3.15)$$

where the residual term  $v_1$  is obtained as a filtered version of  $\dot{\tau}_{hum}$ :

$$v_1 = \frac{\xi}{\xi s + 1} [\chi \dot{\tau}_{hum}] \quad (3.16)$$

As a result, when  $\tau_{hum}$  is constant or  $\xi = 0$ , it is concluded that  $v_1 = 0$ . Moreover, since  $\chi = M_q^{-1}$  and due to *Property* (3.2) of the inertia matrix,  $\chi$  is bounded. Consequently, its filtered version  $\chi_f$  is also bounded, i.e.,  $\|\chi_f\| \leq \rho_\chi = 1/M_1$ . Regarding the boundedness of the human torque  $\|\tau_{hum}\| \leq \rho_\tau$  and its time derivative  $\|\dot{\tau}_{hum}\| \leq \rho_{\tau_d}$ ,  $v_1$  is bounded for any finite value of  $\xi > 0$ , i.e.,  $\|v_1\| \leq \gamma_1$ . ■

The dynamics of two new intermediate variables [79] are defined for the TBA observer design as

$$\begin{aligned} \dot{F}_1 &= -cF_1 + \chi_f^T \chi_f, & F_1(0) &= 0 \\ \dot{F}_2 &= -cF_2 + \chi_f^T \left( \frac{z_1 - z_{1f}}{\xi} - \Psi_f \right), & F_2(0) &= 0 \end{aligned} \quad (3.17)$$

in which  $c$  is a positive constant. Two other intermediate variables are also formulated in terms of  $F_1$  and  $F_2$  and the estimated pHRI torque  $\hat{\tau}_{hum}$  as

$$\begin{aligned} T_1 &= F_1 \hat{\tau}_{hum} - F_2 \\ T_2 &= \chi_f^T \chi_f \hat{\tau}_{hum} - \chi_f^T \left( \frac{z_1 - z_{1f}}{\xi} - \Psi_f \right) \end{aligned} \quad (3.18)$$

*Lemma 2:* The defined variables in (3.18) can be expressed as

$$\begin{aligned} T_1 &= -F_1 \tilde{\tau}_{hum} + v_2 \\ T_2 &= -\chi_f^T \chi_f \tilde{\tau}_{hum} - \chi_f v_1 \end{aligned} \quad (3.19)$$

where  $v_1$  was defined in (3.16) and  $v_2$  is presented as

$$v_2 = \int_0^t e^{-c(t-r)} \chi_f^T(r) [\chi_f(r) (\tau_{hum}(t) - \tau_{hum}(r)) + v_1(r)] dr \quad (3.20)$$

This residual error is bounded as  $\|v_2\| \leq \gamma_2 = (2\rho_\chi^2 \rho_\tau + \rho_\chi \gamma_1)/c$  in which  $\|\chi_f\| \leq \rho_\chi$ ,  $\|\tau_{hum}\| \leq \rho_\tau$  and  $\|v_1\| \leq \gamma_1$ .

**Proof.** The time integration of (3.17) results in

$$\begin{aligned} F_1 &= \int_0^t e^{-c(t-r)} \chi_f^T(r) \chi_f(r) dr \\ F_2 &= \int_0^t e^{-c(t-r)} \chi_f^T(r) \chi_f(r) \left( \frac{z_1 - z_{1f}}{\xi} - \Psi_f \right) (r) dr \end{aligned} \quad (3.21)$$

Employing (3.15) and substituting (3.21) into (3.18) leads to Eq. (3.19) where the boundedness of  $v_2$  is obtained as

$$\begin{aligned} \|v_2\| &\leq \int_0^t e^{-c(t-r)} \|\chi_f^T(r)\| [\|\chi_f(r)\| \|\tau_{hum}(t) - \tau_{hum}(r)\| \\ &\quad + \|v_1(r)\|] dr \\ &\leq \int_0^t (2\rho_\chi^2 \rho_\tau + \rho_\chi \gamma_1) e^{-c(t-r)} dr \\ &\leq \frac{2\rho_\chi^2 \rho_\tau + \rho_\chi \gamma_1}{c} = \gamma_2 \end{aligned} \quad (3.22)$$

■

*Lemma 3:* The matrix  $\chi_f$  is persistently exciting (PE) as  $\int_0^t \chi_f^T(r) \chi_f(r) dr \geq \eta_\chi I$  for  $t > 0$  and  $\eta_\chi > 0$ , and the matrix  $F_1$  in (3.17) is positive definite, i.e.,  $\lambda_{\min}(F_1) \geq \eta_F > 0$  for  $t > 0$ .

**Proof.** Based on the definition of the regressor matrix  $\chi = M_q^{-1}$  and *Property (3.2)* of the inertia matrix  $M_q$ , and due to the employed low-pass filter (3.13) with the stable minimum phase transfer function  $1/(\xi s + 1)$  [80], one can write:  $\|\chi_f\|_{\min} \geq (1/M_2)$ . As a result:

$$\begin{aligned} \int_0^t \chi_f^T(r) \chi_f(r) dr &\geq \int_0^t \|\chi_f^T\|_{\min} I \|\chi_f\|_{\min} I dr \\ &\geq \int_0^t \left( \frac{I}{M_2} \right) \left( \frac{I}{M_2} \right) dr = (t/M_2^2) I \end{aligned} \quad (3.23)$$

Considering  $\eta_\chi = t/M_2^2$ , the first proposition in *Lemma 3* is proven. Now, the variable matrix  $F_1$  in (3.21) is analyzed as

$$\begin{aligned} F_1 &\geq \int_0^t e^{-c(t-r)} \|\chi_f^T\|_{\min} I \|\chi_f\|_{\min} I dr \\ &\geq \left( \frac{I}{M_2^2} \right) \int_0^t e^{-c(t-r)} dr = \left( \frac{1 - e^{-ct}}{cM_2^2} \right) I \end{aligned} \quad (3.24)$$

Having  $\eta_F = (1 - e^{-ct})/(cM_2^2)$ , the positive definiteness of  $F_1$  with the minimum singular value of  $\eta_F$  is guaranteed. ■

The nonlinear dynamics of time-varying adaptation gain for the observer is formulated as

$$\dot{\mathcal{H}}_\tau = c\mathcal{H}_\tau - \mathcal{H}_\tau \chi_f^T \chi_f \mathcal{H}_\tau \quad (3.25)$$

According to the fact that  $(d/dt)\mathcal{H}_\tau \mathcal{H}_\tau^{-1} = \dot{\mathcal{H}}_\tau \mathcal{H}_\tau^{-1} + \mathcal{H}_\tau (d/dt)\mathcal{H}_\tau^{-1} = 0$  and using (3.25),  $(d/dt)\mathcal{H}_\tau^{-1} = -c\mathcal{H}_\tau^{-1} + \chi_f^T \chi_f$  and thereby:

$$\begin{aligned} \mathcal{H}_\tau &= \left[ e^{-ct} \mathcal{H}_\tau^{-1}(0) + \int_0^t e^{-c(t-r)} \chi_f^T(r) \chi_f(r) dr \right]^{-1} \\ &= [e^{-ct} \mathcal{H}_\tau^{-1}(0) + F_1]^{-1} \end{aligned} \quad (3.26)$$

Regarding (3.26), the gain matrix  $\mathcal{H}_\tau$  exponentially converges to  $F_1^{-1}$ , i.e.,  $\mathcal{H}_\tau F_1 \rightarrow I$ .

*Lemma 4:* The adaptation gain matrix  $\mathcal{H}_\tau$  is bounded with lower and upper bounds.

**Proof.** To investigate the boundedness of the adaptation gain  $\mathcal{H}_\tau$ , Eq. (3.26) is rewritten as

$$\mathcal{H}_\tau^{-1}(t) = e^{-ct} \mathcal{H}_\tau^{-1}(0) + F_1(t) \quad (3.27)$$

Based on *Lemma 3* and positive definiteness of  $F_1(t)$ ,

$$\mathcal{H}_\tau^{-1}(t) \geq \eta_F I \quad (3.28)$$

On the other hand, due to the upper boundedness of  $\|\chi_f\| \leq \rho_\chi$ , one can conclude from (3.27) that:

$$\mathcal{H}_\tau^{-1}(t) \leq \mathcal{H}_\tau^{-1}(0) + \rho_\chi^2 \int_0^t e^{-c(t-r)} I dr \leq \mathcal{H}_0^{-1} + \frac{\rho_\chi^2}{c} I \quad (3.29)$$

Therefore, the boundedness of time-varying observer gain is perceived from (3.28) and (3.29) as

$$R_1 I \leq \mathcal{H}_\tau(t) \leq R_2 I \quad (3.30)$$

in which  $R_1 = 1/(\lambda_{\min}(\mathcal{H}_0^{-1}) + \rho_\chi^2/c)$  and  $R_2 = 1/\eta_F$  are its upper and lower bounds, respectively. ■

The adaptation (estimation) law for the pHRI torque in this nonlinear TBA observer is defined as

$$\dot{\hat{\tau}}_{hum} = -\Gamma_\tau \mathcal{H}_\tau (T_1 + \alpha T_2) \quad (3.31)$$

where  $\Gamma_\tau > 0$  and  $\alpha > 0$  are the constant scaling factors.

### 3.3.2 Unified Stability Proof

*Theorem:* Combining the control law (3.9) that dictates the motor torque and the observer estimation of the pHRI torque (3.31) for the exoskeleton, the convergence of tracking error  $\epsilon_q$  and the torque estimation error  $\tilde{\tau}_{hum}$  to a compact region is achieved. In other words, the system response is uniformly ultimately bounded (UUB) in tracking the desired locomotion trajectory and estimating the bounded pHRI torque.

**Proof.** The following Lyapunov function candidate is utilized to ensure the stability of controlled exoskeleton:

$$V(t) = \frac{1}{2} (\epsilon_q^T M_q \epsilon_q + \Gamma_\tau^{-1} \tilde{\tau}_{hum}^T \mathcal{H}_\tau^{-1} \tilde{\tau}_{hum}) \quad (3.32)$$

and its time derivative is obtained as

$$\dot{V}(t) = \epsilon_q^T M_q \dot{\epsilon}_q + \Gamma_\tau^{-1} \tilde{\tau}_{hum}^T \mathcal{H}_\tau^{-1} (\dot{\tau}_{hum} - \dot{\hat{\tau}}_{hum}) + \frac{1}{2} (\epsilon_q^T \dot{M}_q \epsilon_q + \Gamma_\tau^{-1} \tilde{\tau}_{hum}^T \dot{\mathcal{H}}_\tau^{-1} \tilde{\tau}_{hum}) \quad (3.33)$$

Substituting the closed-loop dynamics (3.10), the adaptation gain's time variation (3.25) and the observer formulas (3.19) and (3.31) for the HRI torque into (3.33) results in

$$\begin{aligned} \dot{V}(t) = & -\kappa_2 \epsilon_q^T M_q \epsilon_q - \epsilon_q^T \tilde{\tau}_{hum} + \frac{1}{2} \epsilon_q^T (\dot{M}_q - 2C_q) \epsilon_q + \Gamma_\tau^{-1} \tilde{\tau}_{hum}^T \mathcal{H}_\tau^{-1} (\dot{\tau}_{hum} \\ & + \Gamma_\tau \mathcal{H}_\tau (-F_1 \tilde{\tau}_{hum} + v_2 - \alpha \chi_f^T \chi_f \tilde{\tau}_{hum} - \alpha \chi_f v_1)) \\ & + \frac{1}{2} \Gamma_\tau^{-1} \tilde{\tau}_{hum}^T (-\dot{c} \mathcal{H}_\tau^{-1} + \chi_f^T \chi_f) \tilde{\tau}_{hum} \end{aligned} \quad (3.34)$$

Considering *Property 1* of the exoskeleton dynamics, and the lower and upper bounds of matrices and vectors, one can obtain the following upper bound of  $\dot{V}(t)$ :

$$\dot{V}(t) \leq -\mathcal{D}_\epsilon \|\epsilon_q\|^2 - \mathcal{D}_{\tau_1} \|\tilde{\tau}_{hum}\|^2 + \|\epsilon_q\| \|\tilde{\tau}_{hum}\| + \mathcal{D}_{\tau_2} \|\tilde{\tau}_{hum}\| \quad (3.35)$$

in which the gains  $\mathcal{D}_i$  are defined in terms of matrices' and vectors' norms as

$$\begin{aligned}\mathcal{D}_\epsilon &= \kappa_2 \lambda_{\min}(M_q) = \kappa_2 M_1 \\ \mathcal{D}_{\tau_1} &= \eta_F + \frac{\alpha}{M_2^2} + \frac{c}{\Gamma_\tau R_2} - \frac{1}{\Gamma_\tau M_1^2} \\ \mathcal{D}_{\tau_2} &= \frac{\rho_{\tau_d}}{\Gamma_\tau R_1} + \gamma_2 + \frac{\alpha\gamma_1}{M_1^2}\end{aligned}\tag{3.36}$$

As a result, the time derivative of the Lyapunov function is negative definite  $\dot{V}(t) < 0$  outside of this compact region:

$$\begin{aligned}\|\epsilon_q\| &\leq \frac{-\mathcal{B}_2 + \sqrt{\mathcal{B}_2^2 + 4\mathcal{B}_1\mathcal{B}_3}}{2\mathcal{B}_1} \\ \|\tilde{\tau}_{hum}\| &\leq \frac{-\mathcal{B}_5 + \sqrt{\mathcal{B}_5^2 + 4\mathcal{B}_4\mathcal{B}_6}}{2\mathcal{B}_4}\end{aligned}\tag{3.37}$$

where  $\mathcal{B}_1 = \mathcal{D}_\epsilon$ ,  $\mathcal{B}_2 = \|\tilde{\tau}_{hum}\|$ ,  $\mathcal{B}_3 = \mathcal{D}_{\tau_2} \|\tilde{\tau}_{hum}\|$ ,  $\mathcal{B}_4 = \mathcal{D}_{\tau_1}$ ,  $\mathcal{B}_5 = \|\epsilon_q\| + \mathcal{D}_{\tau_2}$  and  $\mathcal{B}_6 = \mathcal{D}_\epsilon$ .

According to the above analysis, the positive definite Lyapunov function declines outside of the bounded region introduced in Eq. (3.37). Therefore, the convergence to this compact region is achieved whose dimensions are obtained regarding the bounded time derivative of the pHRI torque ( $\dot{\tau}_{hum}$ ). This guarantees the UUB of the system response in terms of the bounded trajectory tracking error  $\epsilon_q$  (and consequently  $e_q$ ) and the bounded pHRI torque estimation error  $\tilde{\tau}_{hum}$  in (3.37). Thereby, the closed-loop exoskeleton system interacting with the human user is stable under the assumption of bounded-varying interaction torque ( $\|\dot{\tau}_{hum}\| \leq \rho_{\tau_d}$ ) employing the proposed TBA disturbance-observer-based nonlinear strategy for the low-level control. ■

### 3.4 Experimental Studies

In order to evaluate the performance of the developed autonomous control scheme and assess its adaptive features in high and low levels, comprehensive experiments were conducted on the Indego exoskeleton (Parker Hannifin Corporation) as the testbed. Two able-bodied wearers (33 and 27 years of age) wore the exoskeleton as shown in Fig. 3.3 and performed the locomotion experiment with a minimum duration of 100



Figure 3.3: Indego lower-limb exoskeleton worn by two able-bodied users for over-ground walking: first participant (33 year-old) and second participant (27 year-old)

sec. To implement the proposed controller, the major computational effort consists of the time integration of the CPG dynamics (3.6) and Eqs. (3.17), (3.25), (3.31) in the disturbance observer structure, as well as performing the required calculations to command the control law (3.9) for each joint of the exoskeleton. The proposed strategy was implemented in the real-time MATLAB-Simulink environment running on a PC (Intel Core i7-8650U CPU @ 1.90GHz and 8.00 GB RAM) and required communications (between sensors, PC, and actuators), and the required computations were conducted with the sampling time of 5 msec. Preliminary tests were first conducted to identify the passive dynamic parameters of the combined exoskeleton-human limb system to implement the proposed torque control law accurately.

The initial hip and knee trajectories were extracted from motion capture data of typical human locomotion in the literature [81], [82]. To acquire this experimental data, the subject walked for at least 20 sec in each trial for a total of approximately 1 hour and 10 min (with more than 3600 gait cycles). A marker-based motion capture system was employed to obtain 2D joint angles and velocities. A Fourier analysis was conducted on the acquired trajectories to obtain the minimum adequate number of series and identify the best values of corresponding coefficients. Eight terms of

	Hip initial motion	Knee initial motion
Coefficients of Fourier series	$a_0 = 10.13$ $a_1 = 21.80, a_2 = -5.07$ $a_3 = -0.49, a_4 = -0.52$ $a_5 = 0.20, a_6 = -0.07$ $a_7 = -0.09, a_8 = -0.09$ $b_1 = -10.77, b_2 = -2.21$ $b_3 = 1.86, b_4 = 0.41$ $b_5 = 0.20,$ $b_6 = -0.06$ $b_7 = -0.05,$ $b_8 = -0.05$	$a_0 = 22.44$ $a_1 = -2.93, a_2 = -14.32$ $a_3 = 0.05, a_4 = -0.38$ $a_5 = 0.36,$ $a_6 = 0.20$ $a_7 = -0.01, a_8 =$ $0.03$ $b_1 = -26, 48, b_2 =$ $9.81$ $b_3 = 4.44, b_4 = 1.87$ $b_5 = 0.59, b_6 = -0.15$ $b_7 =$ $-0.08, b_8 = -0.07$

Table 3.1: Coefficients of the Fourier series (3.7) for the hip and knee initial motions based on the analysis of normal gait trajectories

the Fourier series ( $N_i = 8$  in (7.17)) were sufficient to estimate these hip and knee motions with the sine and cosine functions. Attained coefficients of the Fourier series for the hip and knee motions based on this analysis are listed in Table 3.1, which resulted in estimation of the typical gait [81, 82] with more than 98% accuracy for each joint.

Parameters and initial values of the proposed ACPG dynamics for the hip and knee joints of both legs are listed in Table 3.2. The initial phase difference of  $\pi$  rad was considered between the left and right legs' motions, as is the case for typical bipedal locomotion. The estimated pHRI torques of all joints, determined based on the TBA observer law (3.31) and the defined dead-zone function (3.5), are shown in Fig. 3.4a for the first wearer (33 year-old participant). The corresponding pHRI energy transferred through each joint and obtained by (3.4) and the total value of this energy are demonstrated in Fig. 3.4b for this experiment. As seen, this wearer applied the major torques over the first four steps (with a maximum magnitude of 7.1 N.m) to personalize the gait motion. According to Figs. 3.4a and 3.4b, he injected most of the pHRI energy by the right hip torque and then the right knee torque to accelerate the motion, while he applied decelerating torques on the left knee joint to control the gait. The effect of this interaction on the variation of the total locomotion

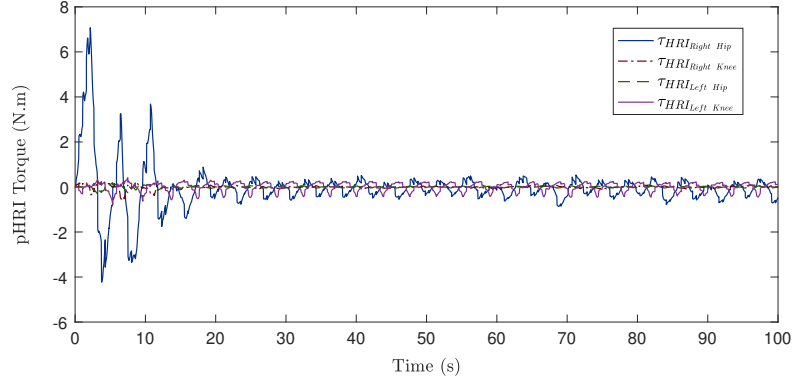
	Hip and knee CPGs' parameters
Dynamic parameter values	$\gamma_{h-h} = 0.0075, \gamma_{h-k} = 0.0075, \gamma_{k-h} = 0.0075, \beta_\omega = 10\pi, \beta_\mu = 10\pi, \psi = 0.0045, \lambda = 0.006, \Omega = \frac{\pi}{2}, A = 1$
Initial values	$\theta_{right}(0) = 2 \text{ rad}, \theta_{left}(0) = 2 + \pi \text{ rad}, \omega(0) = 1.26 \text{ rad/s}, \mu(0) = 1$

Table 3.2: Parameter and initial values of the proposed ACPGs dynamics (3.6) for the hip and knee joints

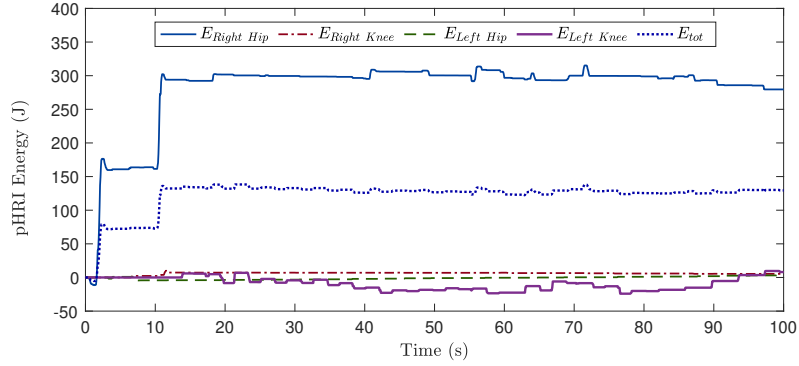
frequency  $\omega(t)$  is depicted in Fig. 3.4c. Rapid online response of the ACPG (3.6) to these interactions was achieved during each stride. The steady-state magnitude of the locomotion frequency in Fig. 3.4c had a 42% increase with respect to its initial magnitude of 1.17 rad/s and finally settled on  $1.66 \pm 0.02$  rad/s.

Due to this real-time update of ACPG and the obtained Fourier coefficients in Table 3.1, the desired locomotion trajectories, generated by (3.7) for the right knee and hip joints, are shown in Fig. 3.5a together with the exoskeleton response. The first human user applied the interaction torques in sequential steps (Fig. 3.4a) to modify and increase the gait amplitude (step size) by 15% (Fig. 3.5a) in addition to the walking frequency (Fig. 3.4c), which provided a synchronized variation of the generated bipedal locomotion cycles. The proposed TBA disturbance-observer-based torque controller could facilitate an appropriate convergence of joint positions to the desired gait trajectories with a small bounded tracking error  $e_q$  in the steady-state response (less than 1 degree for each joint), as presented in Fig. 3.5b. This is in accordance with the stability analysis in Sec. 3.3.2 and implies an appropriate estimation of the pHRI torque with a small bounded error  $\tilde{\tau}_{hum}$ , employing the disturbance observer defined in Sec. 3.3.1.

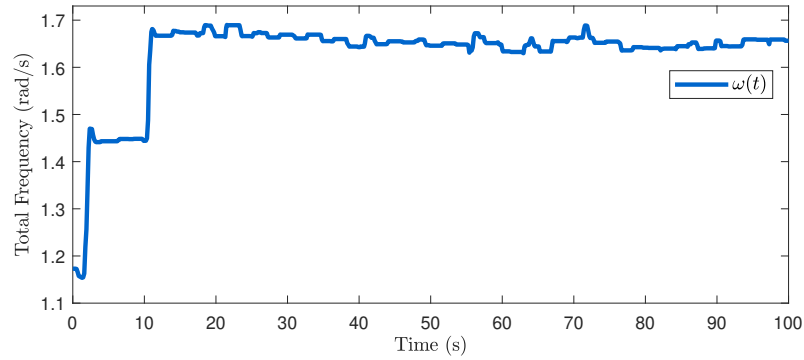
In order to elaborate more on the autonomous shaping of locomotion, the reference trajectory and phase variation of the right hip with respect to the left hip are plotted in Fig. 3.6 for the first wearer. The increase of 15% in total gait amplitude  $\mu(t)$  and its convergence to a steady-state response, together with the relative motion



(a)



(b)



(c)

Figure 3.4: Estimated pHRI (a) torque and (b) energy for different joints, and (c) total frequency of the locomotion, obtained from the proposed ACPG in the presence of HRI for the first wearer

adjustments of adjacent joints, are illustrated in these diagrams. Accordingly, the desired ranges of motion of the knee and hip joints were amended to 78.7 and 61.2 degrees, respectively, from 68.4 and 53.2 degrees. As shown in Fig. 3.6, an average

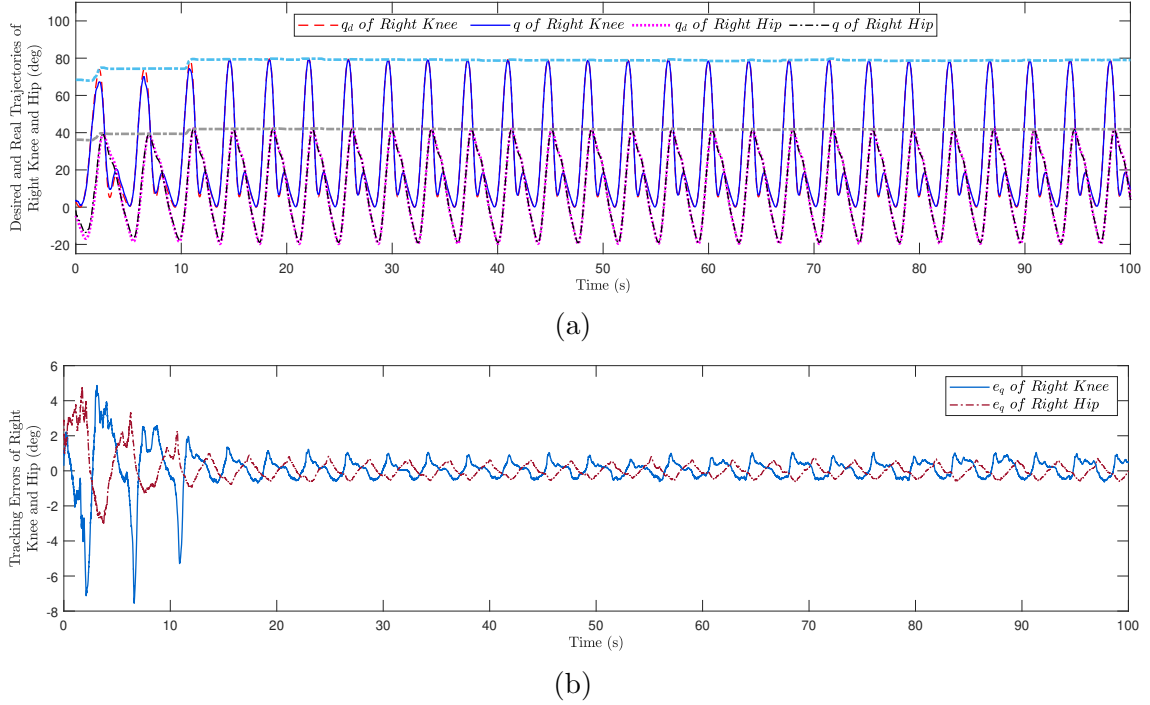


Figure 3.5: (a) Desired and actual trajectories, (b) and (c) tracking errors of the knee and hip joints for the right leg in the presence of pHRI for the first wearer

phase lead of 13.0 degrees in the right hip motion was eventually obtained over the left hip motion in addition to their initial phase difference of 180 degrees, due to the asymmetric rendering of the interaction torques (Fig. 3.4b).

For the second wearer (27 year-old participant), the estimation of pHRI torques and corresponding pHRI energy (3.4) transferred through different joints (hips and knees) are represented in Figs. 3.7a and 3.7b. This wearer exerted the major torques over the first six steps (with a maximum magnitude of 3.61 N.m) to adjust his locomotion pattern. As observed in Figs. 3.7a and 3.7b, this wearer transferred most of the energy through the left hip and then the right hip to accelerate the gait. The variation of the locomotion frequency  $\omega(t)$  in response to this HRI is shown in Fig. 3.7c with a steady-state variation of 53% compared to its initial magnitude of 1.17 rad/s. The generated reference trajectory and phase variation of the right hip with respect to the left hip is illustrated for the second participant in Fig. 3.8.

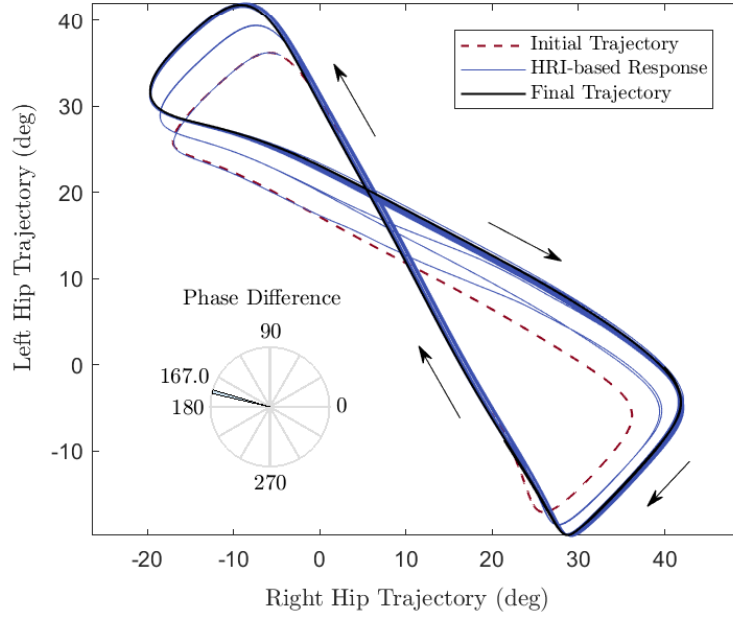
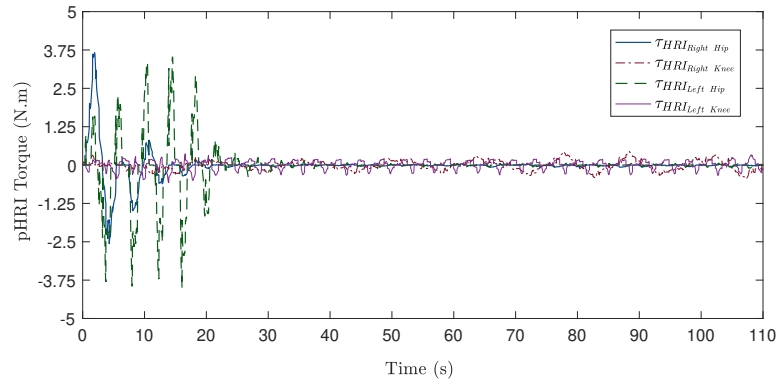


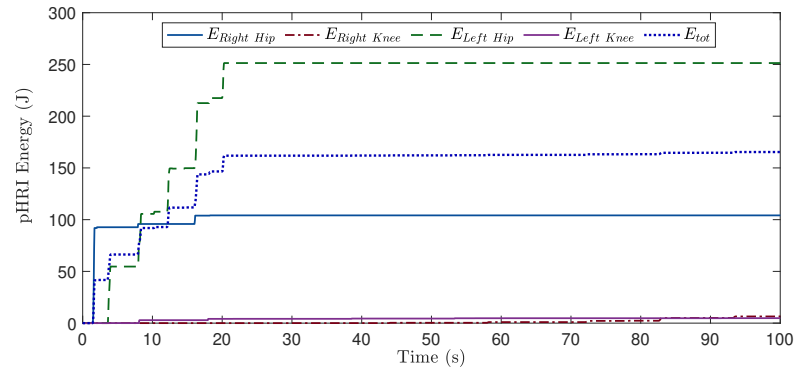
Figure 3.6: Trajectory and phase variation of the right hip with respect to the left hip for the first wearer

### 3.5 Discussion

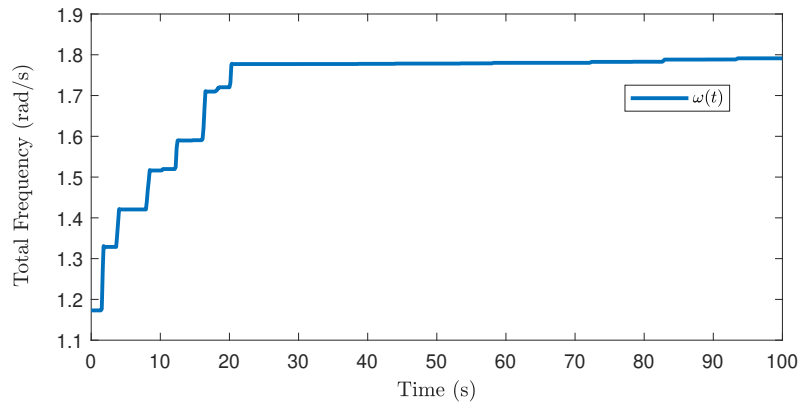
Due to the adaptiveness of the proposed ACPG-based control strategy, the obtained locomotion trajectories were personalized for the two participants engaged in this study. As seen in Fig. 3.4, the first wearer (33 year-old participant) injected 73% of accelerating energy by the right hip torque and 24% by the right knee torque. However, the second wearer (27 year-old participant) modified his gait frequency by transferring 69% and 29% of positive pHRI energy via the left hip and right hip joints, respectively, to accelerate the locomotion, as demonstrated in Fig. 3.7. This implies a significant difference in pHRI over hip joints of the lower-limb exoskeleton between the first and second wearers, in regard to the modification of the locomotion pattern. In addition to this pHRI difference in various joints, the second wearer came up with a final locomotion frequency with 11% more increase from its initial value in comparison with the one achieved by the first wearer. Furthermore, the second wearer made this gait adjustment in 23 sec (over 6 steps), which was 35% longer than



(a)



(b)



(c)

Figure 3.7: Estimated pMRI (a) torque and (b) energy for different joints, and (c) total frequency of the locomotion, obtained from the proposed ACPG in the presence of HRI for the second wearer

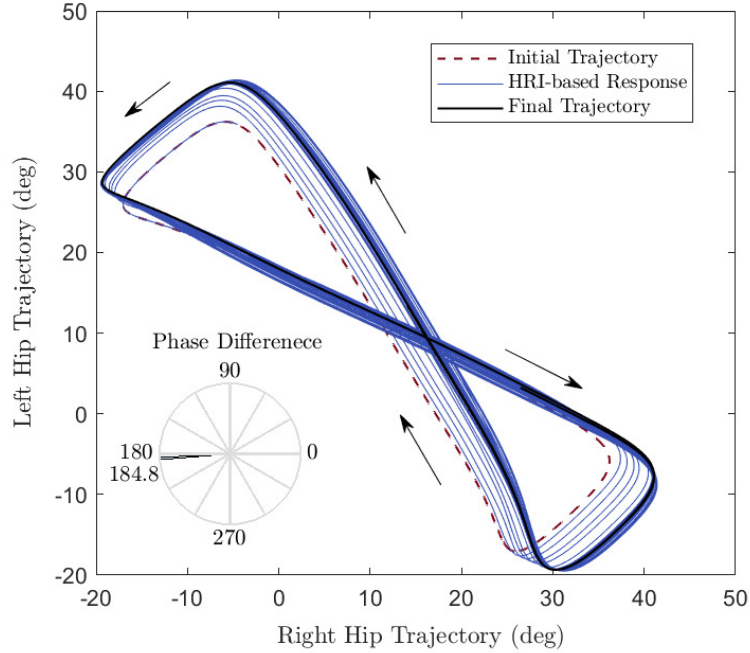


Figure 3.8: Trajectory and phase variation of the right hip with respect to the left hip for the second wearer

the time duration of 15 sec spent by the first wearer to modify his walking pattern (over 4 steps).

An analysis of the relative joint trajectories and phase variations in Figs. 3.6 and 3.8 can provide additional insight into this personalized gait amendment. The second participant decided to raise his steady-state gait amplitude  $\mu(t)$  by 13% (Fig. 3.8) which is slightly less than the 15% increment provided by the first participant (Fig. 3.6). This difference was due to the larger height (longer body segments of the lower limbs) of the first participant and their personal preferences for the step size in their natural walking. The other significant differences between two wearers' performance achieved by employing the proposed intelligent control strategy were the synchronization and phase shifts between the hip and knee joints. Figure 3.8 shows that the second participant made an average phase lag of 4.8 degrees in the right hip motion relative to the left hip; however, the first participant made an average phase lead of 13.1 degrees between these joints' motions (Fig. 3.8). As a result of this

difference, the distortion of the relative trajectories in Fig. 3.6 for the first wearer was more toward the bottom right as compared to the variation in Fig. 3.8 for the second wearer, which was more toward the top left. This is due to rendering most (73%) of the accelerating interaction torques on the right hip by the first wearer (Fig. 3.4b) rather than the left hip that was employed for applying 69% of the accelerating torques by the second wearer (Fig. 3.7b). This performance implies adjustable flexibility in locomotion speed and amplitude, and modification of the synchronization between different joints using the proposed APG-based control strategy for the lower-limb exoskeleton in response to the estimated interaction torques.

### 3.6 Conclusion

A new autonomous control scheme was developed in this work to facilitate flexible and personalized locomotion based on pHRI torque for lower-limb exoskeletons. At the higher level of this scheme, ACPGs were proposed to update the frequency and amplitude of desired gait trajectories for all exoskeleton joints (hips and knees). Simultaneously, the ACPGs were responsible for synchronizing adjacent joints' motions by adjusting their phase differences. These adaptations were defined based on the estimation of pHRI torque and its corresponding energy.

For the low-level control, a multi-layer TBA disturbance observer integrated into a nonlinear torque controller was investigated to estimate and compensate for the HRI torque and to track the desired locomotion trajectories. In addition, this torque estimation was also employed in high-level CPG-based motion planning. The exoskeleton's closed-loop stability was ensured via a Lyapunov analysis such that the UUB of the trajectory tracking error and the torque estimation error was guaranteed.

The developed autonomous control strategy was evaluated experimentally using the Indego exoskeleton (Parker Hannifin Corporation) and having an able-bodied wearer. Smooth and rapid shaping of the gait trajectories was achieved using the proposed ACPGs in real-time for various arbitrary interactions over different joints.

Wearers amended the locomotion frequency and amplitude by up to 53% and 15%, respectively, and modified the phase synchronization between hip motions by up to 13% due to their individual preferences. Appropriate tracking performance of the nonlinear torque controller with a small bounded error (less than 1 degree for each joint) was obtained due to the precise estimation of the interaction torque via the proposed TBA disturbance observer.

# Chapter 4

## Adaptive CPG-based Gait Planning and Control for Exoskeletons

### 4.1 Introduction

Globally, millions of people have experienced stroke, spinal cord injury, multiple sclerosis, and cerebral palsy resulting in physical impairments [83]. To improve their quality of life, assistive robotic systems are developed to help these individuals in routine activities as well as during therapy programs. In this regard, powered lower-limb exoskeletons (such as Indego [7], ReWalk [8], HAL [9], Ekso GT [10], and ExoH3 [11]) have been invented to assist and rehabilitate individuals with neurological impairments [12]. Despite all of the endeavours in designing and deploying these systems for medical purposes, compliant interaction between the robot and wearer is an important safety issue that still needs to be addressed [14]. In order to facilitate complaint and safe physical human-robot interaction (pHRI), autonomous strategies are required to be investigated for generating motion trajectories; however, most commercial exoskeletons have been programmed to track pre-recorded trajectories to ensure repeatability and controllability of the movements. These robotic systems have been controlled using various methods to conduct reproducible physical therapies and rehabilitation exercises [84], [85], [86], [87], in addition to performing safe interactions

in assistive and resistive tasks [88], [89], [90], [91], [92].

In the this chapter, an intelligent strategy is presented based on a new ACPG structure for modulating and controlling of a lower-limb exoskeleton that results in a compliant and safe physical interaction with the human. The ACPGs proposed in this chapter have been developed to address some of the shortcomings encountered while utilizing the ACPGs introduced in Chapter 3. One significant improvement in these ACPGs, compared to the previous version, is the ability to adjust the starting and ending positions of each joint. Additionally, a crucial feature added to these ACPGs is the incorporation of safety terms to ensure that gait characteristics remain within safe limits. Furthermore, despite the introduction of a disturbance observer in Chapter 3, a multi-layer neural network utilizing the NARX model is employed to estimate pHRI torque and energy transmitted through various joints. This approach aims to simplify the pHRI estimation task and avoid the use of complex model-based observers and controllers. The neural network is trained first in a supervised fashion to estimate the closed-loop nonlinear dynamics of the multi-DOF exoskeleton-limb system with various position and velocity trajectories. The responsive features of the proposed ACPGs that enable the wearers to accelerate/decelerate, magnify and shift the synchronized motions of all exoskeleton joints for the bipedal locomotion can be summarized as follows.

- The overall gait frequency is tunable in real-time in terms of the pHRI energy transmitted through all exoskeleton joints.
- The oscillation range for each joint trajectory is also adjustable online based on the pHRI energy, while its initial trend is determined by a Fourier series analysis on experimental sample gait data.
- The mean value of each joint's motion as its equilibrium position is regulated for each person in response to the time integral of pHRI torque.

Subtracting the learned passive dynamics from the simultaneous joint torque during the main gait cycle, the active pHRI torque is determined. Having a PD controller combined with the pHRI torque compensation, an appropriate tracking of joint trajectories (generated by ACPGs) is facilitated.

## 4.2 ACPG-Based Gait Planning

The nonlinear dynamics of a multi-DOF lower-limb exoskeleton interacting with the human user is represented as

$$M_q(q)\ddot{q} + C_q(q)\dot{q} + G_q(q) - \tau_{hum_{pas}} = \tau_{mot} + \tau_{hum_{act}} \quad (4.1)$$

where  $q$  is the vector of exoskeleton joints' position,  $M_q(q)$  is the inertia matrix,  $C_q(q)$  is the matrix of Coriolis, centrifugal and damping terms,  $G_q(q)$  is the vector of gravitational torques,  $\tau_{mot}$  is the exoskeleton's motor torque, and  $\tau_{hum_{pas}}$  and  $\tau_{hum_{act}}$  are passive and active portions of the human torque vector.

Our proposed ACPG is formulated for high-level control of the exoskeleton to manage both legs' locomotion trajectories in real-time. This ACPG dynamics is proposed for variations of the overall locomotion frequency  $\omega(t)$ , equilibrium position  $\xi_i(t)$  and oscillation amplitude  $\rho_i(t)$  of each lower-limb joint's motion and its phase

variation  $\phi_i(t)$  by a nonlinear coupled system as

$$\begin{aligned}
\ddot{\omega}(t) &= \gamma_\omega \left( \frac{\gamma_\omega}{4} (\Omega + \sum_{k=1}^n \psi_k E_k(t) - \omega(t)) - \dot{\omega}(t) \right) \\
\ddot{\rho}_i(t) &= \gamma_\rho \left( \frac{\gamma_\rho}{4} (A_{\rho_i} + \lambda_i E_i(t) - \rho_i(t)) - \dot{\rho}_i(t) \right) \\
&\quad + k_\rho u(\rho_i(t) - \rho_{i_{th+}}) \log \left( \frac{\rho_{i_{max}} - \rho_i(t)}{\rho_{i_{max}} - \rho_{i_{th+}}} \right) \\
\ddot{\xi}_i(t) &= \gamma_\xi \left( \frac{\gamma_\xi}{4} (A_{\xi_i} + \beta_i T_i(t) - \xi_i(t)) - \dot{\xi}_i(t) \right) \\
&\quad + k_{\xi_1} u(\xi_i(t) - \xi_{i_{th+}}) \log \left( \frac{\xi_{i_{max}} - \xi_i(t)}{\xi_{i_{max}} - \xi_{i_{th+}}} \right) \\
&\quad - k_{\xi_2} u(\xi_{i_{th-}} - \xi_i(t)) \log \left( \frac{\xi_{i_{min}} - \xi_i(t)}{\xi_{i_{min}} - \xi_{i_{th-}}} \right) \\
\dot{\phi}_i(t) &= \omega(t) + \sum_{j=1}^{m_i} \eta_{ij} \sin(\phi_i(t) - \phi_j(t) - \Delta\phi_{ij})
\end{aligned} \tag{4.2}$$

in which  $n$  is the number of active exoskeleton joints on the right and left legs, and  $m_i$  is the number of adjacent joints to the joint  $i$ .  $\gamma_\omega$ ,  $\gamma_\rho$  and  $\gamma_\xi$  are constant parameters.  $\rho_{i_{th+}}$  is the positive threshold value of  $\rho_i(t)$  that triggers the deceleration term with the gain  $k_\rho$  to avoid reaching the maximum allowable amplitude  $\rho_{i_{max}}$  of oscillation for each joint.  $\xi_{i_{th+}}$  and  $\xi_{i_{th-}}$  are the positive and negative thresholds  $\xi_i(t)$  that if exceeded the deceleration and acceleration terms with the gains  $k_{\xi_1}$  and  $k_{\xi_2}$  to not cross the maximum and minimum allowable magnitudes  $\xi_{i_{max}}$  and  $\xi_{i_{min}}$  for the equilibrium position of each joint.  $u(\cdot)$  is the step function that activates the  $\log(\cdot)$  function when the corresponding thresholds mentioned above are crossed.  $\psi_i$ ,  $\lambda_i$  and  $\beta_i$  are constant gains for updating frequency, amplitude and equilibrium of the gait cycles, respectively, based on the injected pHRI energy  $E_i$  and the time integral of corresponding pHRI torque  $T_i$ , which are defined for each joint  $i$  as

$$\begin{aligned}
E_i(t) &= \int_0^t \tau_{HRI_i}(t) \dot{q}_i(t) dt \\
T_i(t) &= \int_0^t \tau_{HRI_i}(t) dt
\end{aligned} \tag{4.3}$$

where  $\dot{q}_i(t)$  is the velocity of the exoskeleton's joint  $i$ , and  $\tau_{HRI_i}(t)$  is the estimated

human torque on this joint after applying a dead-zone function:

$$\tau_{HRI_i} = \begin{cases} \hat{\tau}_{humact_i} - \tau_{th_+} & \hat{\tau}_{humact_i} > \tau_{th_+} \\ 0 & \tau_{th_-} \leq \hat{\tau}_{humact_i} \leq \tau_{th_+} \\ \hat{\tau}_{humact_i} - \tau_{th_-} & \hat{\tau}_{humact_i} < \tau_{th_-} \end{cases} \quad (4.4)$$

in which  $\tau_{th_-}$  and  $\tau_{th_+}$  are the negative and positive thresholds of this dead-zone function. Wearers can modify the gait cycle characteristics if they apply any torque beyond these thresholds. The reference trajectory for the joint  $i$  of the exoskeleton is defined using Fourier series expansion as

$$q_{r_i}(t) = \xi_i(t) + \rho_i(t) \sum_{l=1}^{S_i} (c_{i_l} \cos(l\phi_i(t)) + d_{i_l} \sin(l\phi_i(t))) \quad (4.5)$$

where  $c_{i_l}$  and  $d_{i_l}$  are the coefficients of the Fourier series (with  $S_i$  terms) that initially harmonize the reference motion of the joint  $i$  with a typical walking trajectory. The equilibrium  $\xi_i(t)$ , amplitude  $\rho_i(t)$  and phase  $\phi_i(t)$  of each joint's oscillatory motion in (4.5) are amended in real-time by the proposed ACPG-based update rules (4.2), as illustrated in Figs. 4.1a and 4.1b. As the reference trajectory generated in (4.5) is time-continuous and differentiable, the proposed learning-based control strategy can facilitate a smooth tracking performance. Other features of the proposed adaptive locomotion planning (4.2) and (4.5) are mentioned as follows.

Synchronized gait trajectories are generated for different joints with the same overall frequency  $\omega(t)$ . The other coupling between phases of adjacent joints is defined by the  $\sin(\cdot)$  function in the connected dynamics of  $\phi_i(t)$  in (4.2), based on the methodology proposed in [16]. The amplitude of each joint trajectory  $\rho_i(t)$  is amended online based on (4.2), while the corresponding initial Fourier coefficients  $c_{i_l}$  and  $d_{i_l}$  are specified from the analysis of experimental data. The transmitted pHRI energy  $E_i(t)$  through each joint  $i$  of the exoskeleton can modify the range of oscillation  $\rho_i(t)$  for that joint. The gait frequency  $\omega(t)$  is also adjusted in real-time according to (4.2) in terms of the pHRI energy  $\sum_{k=1}^n \psi_k E_k(t)$  transmitted through all exoskeleton joints with the scaling factors of  $\psi_k$ . Due to this feature, by applying the interaction torques

and transferring energy  $E_i(t)$ , the wearer is capable of accelerating or decelerating the synchronized locomotion speed/frequency of all  $n$  joints of the exoskeleton. If the applied pHRI torque  $\tau_{HRI_i}$  is in the same direction as the velocity  $\dot{q}_i$  for each joint over time, the wearer will inject energy to the system based on (4.3) and this would increase the walking speed. Conversely, having the torque and velocity in opposite directions and making negative  $E_i$  in (4.3) would result in the speed reduction in (4.2). At the same time, human users can increase or decrease the range of motion for each joint with the authority factor of  $\lambda_i$  for any symmetric or asymmetric walking. In addition, a logarithmic barrier function is defined in (4.2) to control and decelerate the rising rate of  $\rho_i(t)$  after crossing the threshold  $\rho_{ith_+}$  to stay below the maximum allowable amplitude  $\rho_{i_{max}}$  of each joint oscillation regarding the exoskeleton's feasible range of movement.

The other variable that is adjusted in the proposed ACPG-based gait planning (4.2), in response to the time integral of pHRI torque  $T_i$ , is the equilibrium position  $\xi_i(t)$  of each joint's motion. This is due to the difference in mean values of joint trajectories for various individuals with or without disabilities. However, if a human user exceeds the upper or lower threshold ( $\xi_{ith_+}$  or  $\xi_{ith_-}$ ) of this mean value, a logarithmic barrier function in the dynamics of  $\xi_i(t)$  will be activated to decelerate its magnitude variation with the gains of  $k_{\xi_1}$  and  $k_{\xi_2}$ . These thresholds and barrier functions are devised to ensure that the maximum and minimum allowable magnitudes of equilibrium positions  $\xi_{i_{max}}$  and  $\xi_{i_{min}}$  are not crossed.

### 4.3 Learning-Based pHRI Torque Estimation and Tracking Controller

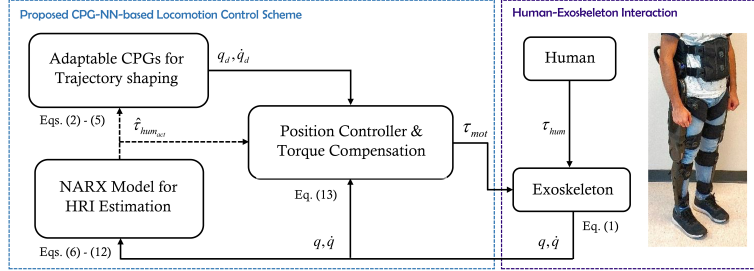
In this section, an NN-based technique is utilized in a supervised fashion to learn the dynamics of the exoskeleton-limb system (4.1) and finally estimate the active pHRI torque  $\tau_{hum_{act}}$ . To this end, the NARX neural network model is employed to learn the exoskeleton-limb dynamics and estimate HRI torque. The estimated pHRI torque is

employed in the proposed ACPG structure to shape the gait trajectories of all joints based on the wearer’s physical interaction with the exoskeleton. At the same time, the estimated pHRI torque is compensated in tracking control law to follow the generated reference trajectories properly, as depicted in Fig. 4.1a.

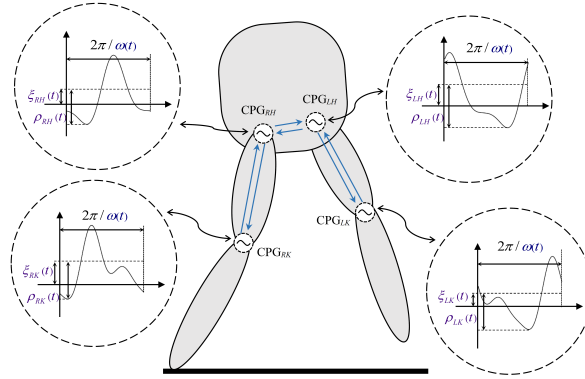
### 4.3.1 NARX Neural Network Scheme

Since the development of NNs, they have been explored as appropriate computing systems with generalization properties that are beneficial for identifying dynamic systems and predicting their time-series responses [93]. The NARX is a dynamic recurrent network which has been widely used in the dynamic identification of different robotic systems [37], [38], [94]. This network has outstanding capabilities in effective learning including fast convergence, high accuracy, and appropriate generalization compared to the conventional recurrent neural networks [93], [94]. Also, the employment of the historical data in the estimation of the system’s current output, makes the NARX an excellent tool for the identification of nonlinear dynamics. Accordingly, the NARX structure is taken into account in this study to learn the nonlinear passive dynamics of the human-exoskeleton system (the left side of (4.1)). This learning is organized based on preliminary experimental data gathered when the exoskeleton is worn by the user, and the whole system is driven and moved by motors  $\tau_{mot}$  with minimum active torque generation  $\tau_{humact}$  (by relaxing the lower-limb muscles). Position, velocity, and torque data for all joints of the human-exoskeleton system are collected for various locomotion patterns (frequencies and amplitudes). These data are used to train and assess the NN with the joint position and velocity considered as the input  $u(t)$  and the motor torques as the output  $y(t)$  of this network. The discrete-time nonlinear function of the NARX model [95] is defined as

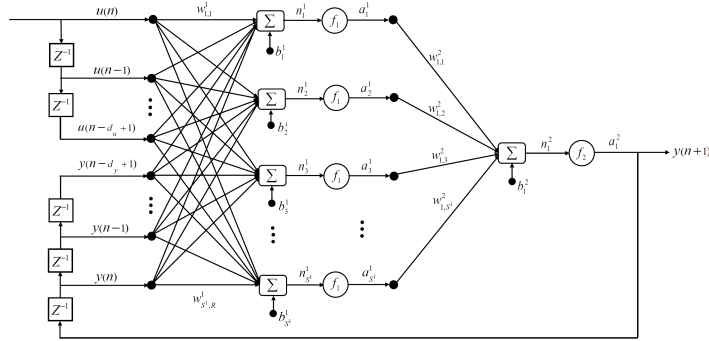
$$\begin{aligned}
 y(t) = & f[y(t-1), y(t-2), \dots, y(t-d_y); u(t-1), \\
 & u(t-2), \dots, u(t-d_u)]
 \end{aligned}
 \tag{4.6}$$



(a)



(b)



(c)

Figure 4.1: ACPG-based gait planning: (a) control architecture, (b) ACPG structure for online adjustment of the locomotion's frequency, amplitude and mean value, and (c) NARX model for the estimation of active pHRI torque

where  $u(t)$  and  $y(t)$  are input and output vectors of this model, and  $d_y$  and  $d_u$  denote the input and output memory orders, respectively. A schematic of the employed NARX neural network with one hidden-layer is depicted in Fig. 4.1c. Considering  $k$  as the current time step, the input of each neuron in the hidden layer at time  $k + s$  is given as [96]

$$\begin{aligned}
n_i^1(k+s-1) = & b_i^1 + \\
& \sum_{j=1}^{\min(s,d_u)} w_{i,j}^1 u(k+s-j) + \sum_{j=s+1}^{d_u} w_{i,j}^1 u(k+s-j) + \\
& \sum_{j=1}^{\min(s-1,d_y)} w_{i,j+d_u}^1 y(k+s-j) + \sum_{j=s}^{d_y} w_{i,j+d_u}^1 y(k+s-j)
\end{aligned} \tag{4.7}$$

where  $w_{i,j}^1$  are weights and  $b_i^1$  are biases of this network. The outputs of the hidden layer and output layer are defined respectively as

$$\begin{aligned}
n_1^2(k+s) = & \sum_{i=1}^{S^1} w_{1,i}^2 f_1 [n_i^1(k+s-1)] + b_1^2 \\
y(k+s+1) = & a_1^2(k+s+1) = f_2 [n_1^2(k+s)]
\end{aligned} \tag{4.8}$$

in which  $S^1$  denotes the number of neurons in the hidden layer.  $f_1$  and  $f_2$  are activation functions of hidden and output layers, set to be tangent-sigmoid and purelin functions, respectively.

Two different modes of the NARX neural network were suggested in the literature, including the parallel and series-parallel modes [37, 38, 93, 94]. The estimated output is fed back to the neural network's inputs in the parallel mode; however, the real values of output are used in the series-parallel mode [95]. In this study, the series-parallel mode is utilized to avoid error accumulation and achieve a more accurate pHRI torque estimation.

### 4.3.2 Learning Algorithm

Having  $m$  samples from one set of data, the mean square error (MSE) and the cost function ( $J$ ) are formulated as [96]

$$\begin{aligned} MSE(w, b) &= \frac{1}{m} \sum_{k=1}^m [y(k) - \hat{y}(k)]^2 \\ J(w, b) &= MSE(w, b) + \frac{1}{m} \lambda \sum_w w^T w \end{aligned} \quad (4.9)$$

where  $w$  and  $b$  are the weight and bias values in the NARX structure, and  $\lambda > 0$  is the regulation parameter. In order to determine the minimum amount of the cost function ( $J$ ), the partial derivatives of that with respect to  $w$  and  $b$  need to be minimized. The steepest descent method is used for this purpose, which results in the following update rule for the structural NARX parameters for each iteration [96]

$$\begin{aligned} b_{next} &= b_{current} - \alpha \frac{\partial}{\partial b} (MSE) \\ w_{next} &= \left(1 - \frac{\alpha \lambda}{m}\right) w_{current} - \alpha \frac{\partial}{\partial w} (MSE) \end{aligned} \quad (4.10)$$

in which  $\alpha$  is the learning rate of the steepest descent method. Note that the output of this learning technique is the estimated dynamics of the combined exoskeleton-limb system (the left side of (4.1)) for each joint  $i$  with minimum active torque  $\tau_{humact}$  obtained from preliminary experiments:

$$\hat{\tau}_{dyn_i}(t) = y(t) \quad (4.11)$$

Given this estimation, the active pHRI torque can be estimated in the main experiments based on (4.1) at any instance of the motion as

$$\hat{\tau}_{humact_i}(t) = \tau_{mot_i}(t) - \hat{\tau}_{dyn_i}(t) \quad (4.12)$$

which is employed in the proposed ACPG structure (7.16)-(4.4).

### 4.3.3 Tracking Controller with Torque Compensation

As a result of learning the exoskeleton-limb dynamics in various positions and velocities using the NARX model and estimating  $\tau_{humact}$ , this torque can be compensated

in the control law to achieve a precise trajectory tracking performance. Accordingly, the position controller is designed as a combination of an error-based proportional derivative (PD) term and a torque compensation term as the output of proposed learning-based torque estimation:

$$\tau_{mot_i}(t) = K_p(q_{r_i}(t) - q_i(t)) + K_d(\dot{q}_{r_i}(t) - \dot{q}_i(t)) + \hat{\tau}_{hum_{act_i}}(t) \quad (4.13)$$

where  $K_p$  and  $K_d$  are the constant gains of this tracking controller. Note that a typical PD controller, without any torque estimation/compensation or having any online trajectory shaping, is embedded in the Indego exoskeleton system (the tested in this work) for clinical gait therapy.

## 4.4 Experimental Evaluations

The proposed autonomous control strategy was assessed experimentally to evaluate its adaptive capabilities in gait trajectory planning and control using the Indego exoskeleton (Parker Hannifin Corporation). An able-bodied user (27-year-old male) wore the exoskeleton and used a safety harness connected to an overhead lift to avoid injury in the event of falling, as shown in Fig. 4.2. This experiment was planned to demonstrate the adaptability of locomotion trajectories in response to different arbitrary pHRI torques on different joints of the exoskeleton. MATLAB-Simulink was employed in the real-time mode as the control software to implement the proposed strategy, receiving the sensory data and sending the command to actuators at a sampling rate of 200 Hz. Using a CAN interface (Vector VN1610) with 2 channels, the exoskeleton was connected to the operating system (a Core i7 laptop with 16GB RAM) via USB to implement the control strategy. Preliminary tests were first carried out to learn the passive human-exoskeleton dynamics using the NARX model (presented in Sec. 4.3.1), which were required to estimate the active pHRI torque in the proposed strategy.



Figure 4.2: Indego lower-limb exoskeleton assisting a human user in overground walking with a safety harness

A Fourier analysis was carried out on the primary hip and knee motions captured from a typical human gait motion [81], in which eight terms of this series ( $S_i = 8$  in (4.5)) were sufficient to estimate trajectories accurately. The bipedal phase difference between the left and right legs' motions is  $\pi$  rad. Initial values and parameters of the proposed ACPG scheme for the hip and knee joints are provided in the Appendix. These values were specified by trial-and-error, and performing initial tests to achieve user comfort as well as smooth variation of the locomotion trajectory by applying interaction torques around different joints. Accordingly, the exoskeleton flexibility was assessed to display enough deviation from the primary trajectory based on the human's physical interaction by appropriate regulation of ACPG gains. In this trial-and-error method, increasing the gains  $\psi_i$ ,  $\lambda_i$  and  $\beta_i$  in (4.2) increased the human authority in modifying gait speed, and amplitude and equilibrium position of each joint. Moreover, by decreasing the gains  $\gamma_\omega$ ,  $\gamma_\rho$  and  $\gamma_\xi$ , the response of trajectory variation became smoother (with smaller accelerations) and more damped.  $\Omega$  in (4.2) is the pre-determined frequency of walking chosen by the user before online modification.  $\rho_{ith_+} = 1.1 - 1.15$  and  $\rho_{imax} = 1.2$  were regulated in (4.2) to avoid exceeding

the joint limits of the exoskeleton during the primary trajectory of locomotion, as described in Section 4.2.  $\xi_{ith_+}$  and  $\xi_{ith_-}$  were chosen to have a range of 10-12 degrees of variation to amend the equilibrium positions of the hip and knee joints for each person with respect to the typical gait cycle.

Preliminary experiments were performed while the human user wore the exoskeleton and relaxed his lower extremity muscles such that minimum active muscle force was generated. The motion (position and velocity) and actuation (motor torque) data for twenty repetitions, each for 300 seconds, were gathered and combined to include various walking scenarios. These preliminary tests were used to identify the nonlinear passive dynamics of the human-exoskeleton system, as described in Section 4.3.1. Between these empirical tests, the amplitude of walking for different joints had a maximum of 20% variation due to the motion limit of the exoskeleton joints, and the speed of walking experienced a 200% change from the original locomotion pattern (designed to have hip and knee amplitudes of 59 and 70 degrees, and walking frequency of 1.41 rad/s). Also, the equilibrium position for each joint motion had a variation of 100% from the initial value considered at the beginning of the main experiments to cover a wide range of joint motion for human locomotion. Seventy percent of the collected data in preliminary experiments was used for offline training of the NARX model, 15% of that was employed for assessment of the torque estimation, and 15% for validation. The NARX model was structured with ten hidden neurons and two steps of time delay. The Bayesian Regularization method was utilized for training and the maximum torque estimation error after 1 epoch of training (with less than 300 iterations) was  $1.5 \times 10^{-3}$  N.m, which is negligible.

After offline training of the NARX model using the obtained motion and actuation data from the passive dynamics of the human-exoskeleton system, this model was utilized in real-time by the Function Fitting Neural Network block in the Simulink environment. The passive dynamics  $\hat{\tau}_{dyn_i}(t)$ , approximated with high accuracy, was employed in (4.12) to estimate the active human torque  $\hat{\tau}_{hum_{act_i}}(t)$  in the main exper-

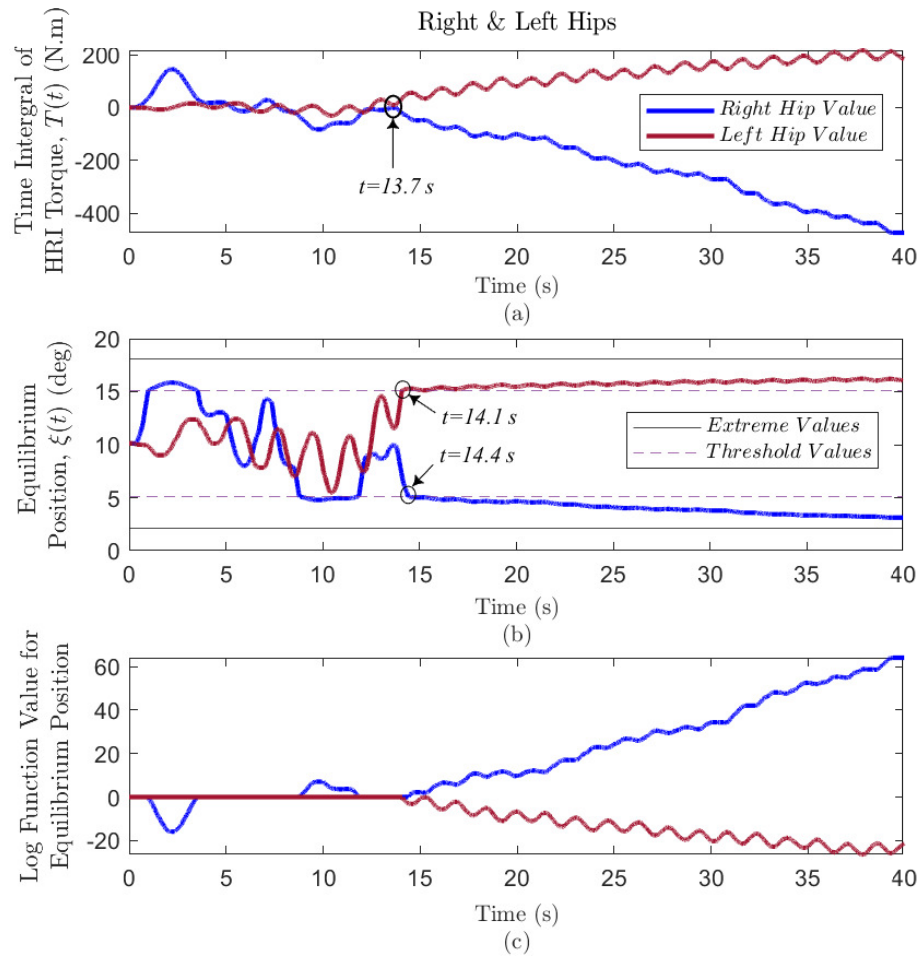


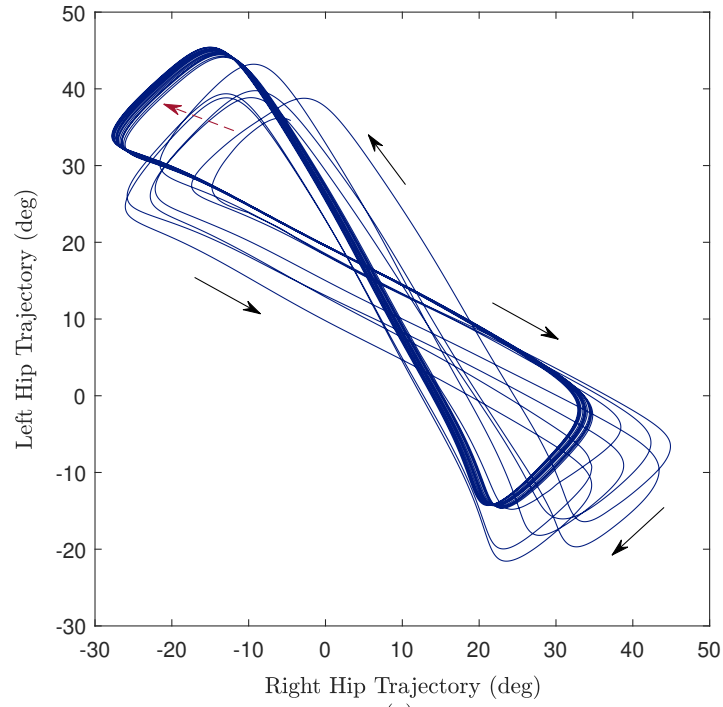
Figure 4.3: Variation of (a) interaction torque integral, (b) equilibrium position, and (c) corresponding logarithmic function value for the right and left hip joints

iments. For both preliminary and main tests, the user wore a safety harness attached to an overhead lift during walking that prevented injury in the case of falling as seen in Fig. 4.2. In this experiment, a human operator applied arbitrary torques on different joints (hips and knees) to change the equilibrium position  $\xi_i(t)$  of locomotion and make it personalized for user. The rapid variation of this equilibrium in response to the time integral of pHRI torques  $T_{RightHip}$  and  $T_{LeftHip}$  is demonstrated in Fig. 4.3 based on the proposed ACPG dynamics (4.2).

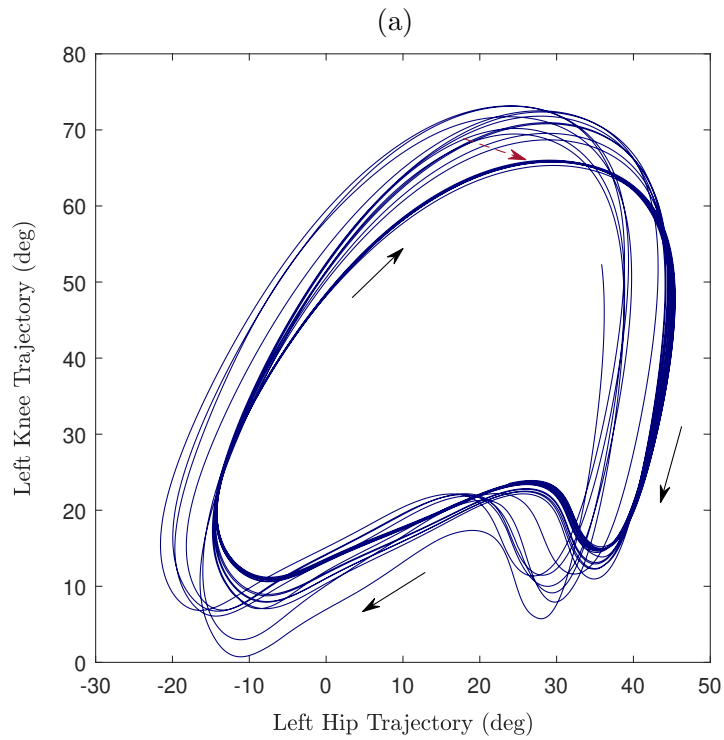
As seen, the pHRI torques of the right and left hips experienced variations at the beginning of walking while they became respectively negative and positive from  $t = 13.7$  s, resulting in a decline of  $\xi_{RightHip}(t)$  and an elevation of  $\xi_{LeftHip}(t)$ . Consequently,  $\xi_{RightHip}(t)$  passed its negative threshold value  $\xi_{H_{th-}} = 5.13$  degrees at  $t = 14.4$  s and  $\xi_{LeftHip}(t)$  exceeded its positive threshold value  $\xi_{H_{th+}} = 15.13$  degrees at  $t = 14.1$  s. In response, the logarithmic barrier functions in (4.2) were activated and returned non-zero values to decelerate these variations and avoid the extreme magnitudes  $\xi_{H_{min}} = 2.13$  degrees and  $\xi_{H_{max}} = 18.13$  degrees. The logarithmic function was zero when the equilibrium position variation for each joint was within its allowable range.

To elaborate more on the autonomous shaping of the gait cycles, the reference trajectory of the left hip with respect to the right hip and left knee motions are shown in Fig. 4.4. The smooth modification of the mean values for the right and left hip motions is observed by the movement of its relative trajectories. This implies a shift of the relative hip trajectories to the top and left due to the increase of the left hip's equilibrium position and the decrease of the right hip's equilibrium position, as illustrated by red arrows in Fig. 4.4a. In this regard, the pattern of left hip-knee trajectories experienced a movement toward the right and bottom in Fig. 4.4b.

The wearer also applied active torques on different joints of the exoskeleton to amend their oscillation ranges of motion  $\rho_i(t)$  according to (4.2). As illustrated in Fig. 4.5, the increase of pHRI energy transferred through the right and left hip joints



(a)



(b)

Figure 4.4: Variation of trajectories for (a) left hip with respect to right hip, and (b) left knee with respect to left hip (black arrows show the direction of locomotion and red arrows show the direction of trajectory deviation)

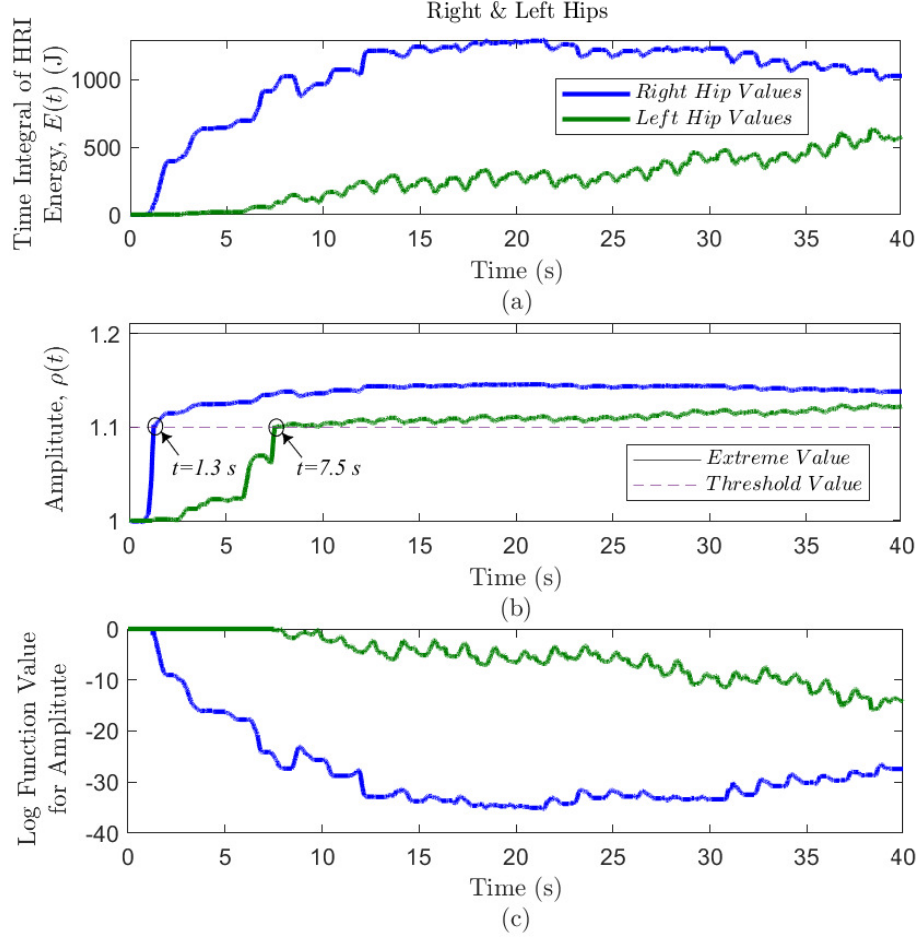


Figure 4.5: Variation of (a) injected pHRI energy, (b) motion amplitude, and (c) corresponding logarithmic function value for the right and left hip joints

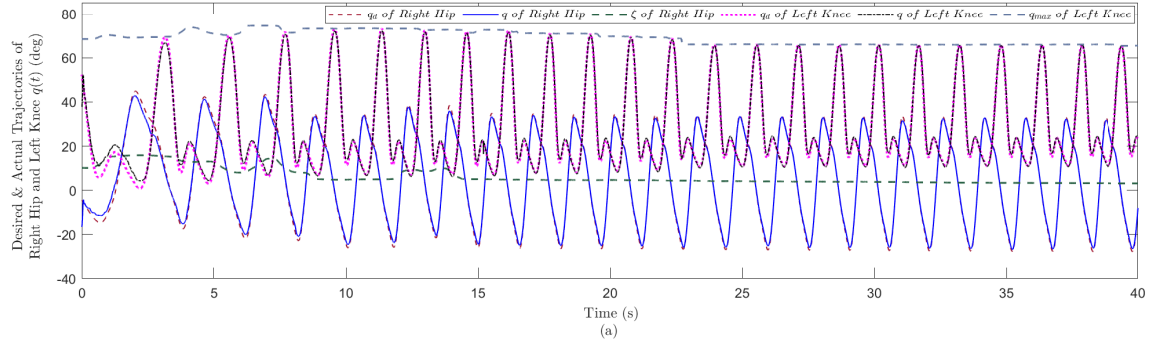
$E_{Right\ Hip}$  and  $E_{Left\ Hip}$  over the first stride resulted in a maximum growth of 14% and 11% in the amplitude  $\rho_{Right\ Hip}(t)$  and  $\rho_{Left\ Hip}(t)$  of these joints' motions. This variation exceeded the amplitude threshold  $\rho_{Hip_{th_+}} = 1.1$  at  $t = 1.3$  s and  $t = 7.5$  s for the right and left hips, respectively, and turned the corresponding logarithmic function on to restrict this escalation. This function gained negative values over the next steps to hold the amplitudes of hip joints below their maximum feasible magnitude  $\xi_{Hip_{max}} = 1.2$ .

Having these adjustable features for shaping the gait cycles and considering feasible motions for exoskeleton joints, the reference trajectories were generated in real-time as demonstrated in Fig. 4.6a for the right hip and left knee. Suitable tracking

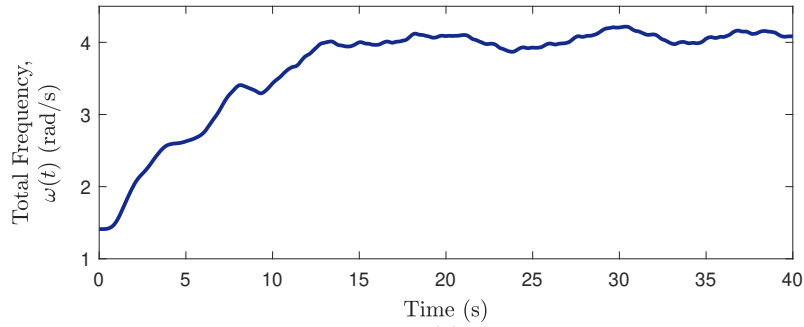
performance using the proposed PD controller with torque compensation (4.13) was attained with small bounded errors in their steady-state response (2 and 4 degrees for the right hip and left knee, respectively). The fluctuation of the right hip equilibrium position (illustrated in Fig. 4.3) and the variation of the maximum value of the left knee motion are also depicted in Fig. 4.6a. Regarding the speed of walking, the wearer torques on different joints could modify the overall locomotion frequency  $\omega(t)$  due to its dynamics (4.2). As seen in Figs. 4.6b and 4.6c, by transferring energy through all of the joints  $E_i(t)$ , the locomotion accelerated and the gait frequency increased from 1.41 rad/s to 4.08 rad/s. After this online adjustment in the first 15 s, the user continued walking with this higher speed for the rest of the path.

## 4.5 Conclusion

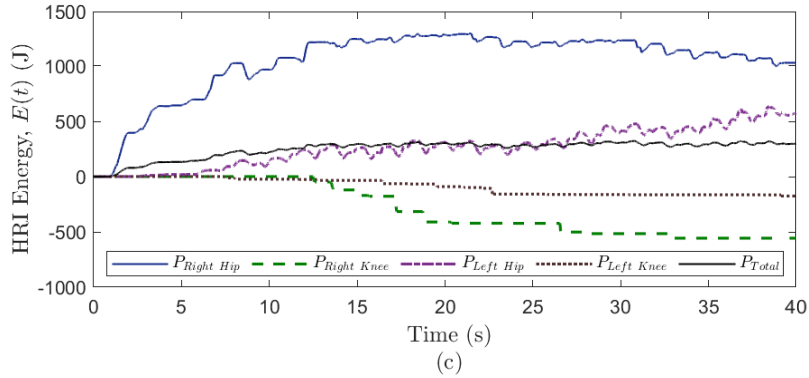
In this study, an intelligent control strategy was designed and tested to provide comfortable and safe bipedal locomotion using lower-limb exoskeletons. To this end, a new ACPG structure was proposed to generate synchronized oscillatory motions for different joints that are responsive to the active pHRI torque. This adaptiveness was facilitated by the amendment of the gait frequency, amplitudes of reference trajectories, and equilibrium positions in terms of the pHRI energy and torques transmitted through the exoskeleton joints. A supervised NN-based learning algorithm was utilized based on the NARX model to learn the passive exoskeleton-limb dynamics and then estimate the active pHRI torque in the joint space. This control strategy was implemented on the Indego exoskeleton (Parker Hannifin Corporation), and experimental results showed suitable flexibility for different locomotion features (with variations in amplitude, equilibrium, and frequency) in the presence of active human behavior. In this work, we gained the benefits of fast supervised learning of the pHRI dynamics and online trajectory shaping by designing a new ACPG structure that can adjust the gait cycles according to the wearer’s physical interaction with exoskeleton. However, the following technical challenges and limitations should be addressed in



(a)



(b)



(c)

Figure 4.6: Amendment of (a) response trajectories with adjustment of equilibrium position and amplitude of the motion for the right hip and left knee, (b) overall locomotion frequency, and (c) pHRI energy transferred through all joints

future studies: (i) designing a nonlinear controller for trajectory tracking that facilitates close-loop stability analysis (instead of the proposed PD controller with torque compensation), and (ii) employing reinforcement learning algorithms to update the approximation of system dynamics during the main walking task considering changes or disturbances in the environment or pHRI.

# Chapter 5

## Deep Reinforcement Learning based Personalized Locomotion Planning for Lower-Limb Exoskeletons

### 5.1 Introduction

Neurological impairments, such as spinal cord injury, stroke, and multiple sclerosis, result in mobility impairments that reduce the quality of life of millions worldwide. The use of assistive and rehabilitative exoskeletons can help individuals maintain their independence and improve their physical fitness. Several powered exoskeletons such as Indego [7], Exo H3 [11], ReWalk [8], HAL [9], and Ekso GT [10] have been developed in recent years for user assistance and rehabilitation in clinics. Despite the great capability of these devices, there still exists a need for software improvement to increase the demand for their use.

The ideal exoskeleton controller must understand a user's intention and adapt to their gait pattern. Que *et al.* [23] used electroencephalogram (EEG) and electrocardiogram (ECG) signals to determine a user's intention and appropriately adjust the exoskeleton's assistance level. The method developed by Gue *et al.* [97] used EEG and ECG signals to select between three predefined trajectories (static, normal walking, high leg lifting) with a neural network classifier. Although using these types

of sensors is a promising way of understanding intention, their usage is limited due to difficulties in attaching the sensors to the user’s body in addition to signal processing. In a different approach, some studies [35, 98] considered the body features, e.g., age and weight, to reshape the exoskeleton’s walking pattern. However, to be sufficiently accurate to capture all features of user’s locomotion, a large number of parameters need to be considered, which makes implementing the method challenging. An alternative solution for these challenges is to use advanced motion planning methods in combination with machine learning (ML) based intention estimation.

This chapter introduces the intelligent CPG (iCPG), which combines reinforcement learning with ACPGs for personalized motion planning of exoskeletons. This method resolves the need for precise initialization in ACPGs (introduced in chapters 3 and 4), which is necessary for effective human-robot interactions (HRIs). Furthermore, our proposed method can adapt to changes in the interaction behaviour of users. The contributions of the paper are summarized as follows:

- We introduce a novel RL-based method to modify pHRI energy based on the user’s interaction behaviour.
- The ACPG structure is improved, and the iCPG method is introduced for the first time to resolve challenges with previous ACPGs [18, 19].

Note that the pHRI torque estimation discussed in this chapter is identical to the algorithm introduced in Chapter 4. Additionally, apart from the modification of pHRI energy using RL in this chapter, the other components of iCPGs closely resemble the ACPGs introduced in Chapters 3 and 4.

## 5.2 Intelligent CPG dynamics

A multi-degree-of-freedom lower-limb exoskeleton interacting with a human user can be modeled as follows:

$$M_q(q)\ddot{q} + C_q(q)\dot{q} + G_q(q) = \tau_{\text{mot}} + \tau_{\text{hum,p}} + \tau_{\text{hum,a}} \quad (5.1)$$

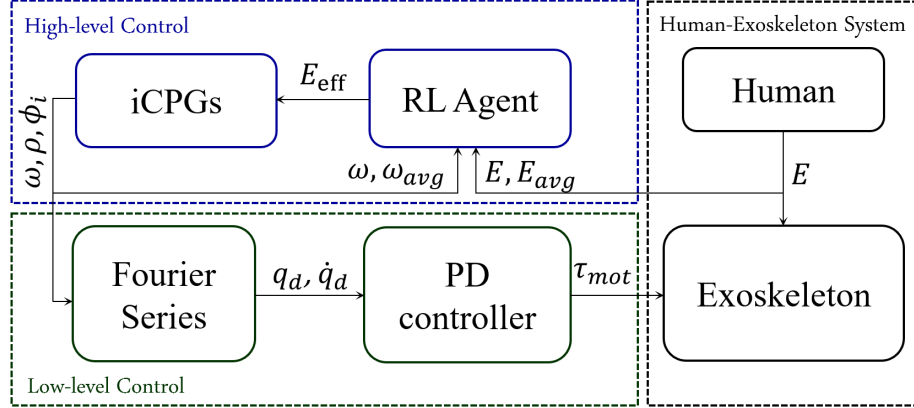


Figure 5.1: Schematic of the proposed iCPG method for personalized motion planning.

where  $M_q(q)$ ,  $C_q(q)$ , and  $G_q(q)$  are the inertia matrix, the matrix of Coriolis, centrifugal, and damping terms, and the vector of gravitational torques, respectively. Further,  $q$  is the vector of the exoskeleton joint positions,  $\tau_{\text{mot}}$  is the exoskeleton's motor torque, and  $\tau_{\text{hum,p}}$  and  $\tau_{\text{hum,a}}$  are the passive and active parts of the human torque vector, respectively.

The ACPG was used to plan the exoskeleton joints' motion in real-time during walking [18–20]. Although it could refine gait trajectories based on pHRIs, the parameter values play an important role in the method's effectiveness. Furthermore, precise parameter identification in conjunction with minimum changes in the user's interaction behaviour is critically important for the ACPG's performance. To address these issues and provide personalized motion planning, we have integrated RL with ACPGs and introduced iCPGs (see Fig. 5.1). The iCPG dynamics for encapsulating variations of the overall locomotion frequency  $\omega(t)$ , oscillation amplitude  $\rho(t)$ , and phase variation of each joint  $\phi_i(t)$  is

$$\begin{aligned}
\ddot{\omega}(t) &= \gamma_{\omega} \left( \frac{\gamma_{\omega}}{4} (\Omega + \psi_{\omega} E_{\text{eff}}(t) - \omega(t)) - \dot{\omega}(t) \right) + k_{\omega} u(\omega(t) - \omega_{th+}) \log \left( \frac{\omega_{\max} - \omega(t)}{\omega_{\max} - \omega_{th+}} \right) \\
\ddot{\rho}(t) &= \gamma_{\rho} \left( \frac{\gamma_{\rho}}{4} (A_{\rho} + \psi_{\rho} E_{\text{eff}}(t) - \rho(t)) - \dot{\rho}(t) \right) + k_{\rho} u(\rho(t) - \rho_{th+}) \log \left( \frac{\rho_{\max} - \rho(t)}{\rho_{\max} - \rho_{th+}} \right) \\
\dot{\phi}_i(t) &= \omega(t) + \sum_{j=1}^{m_i} \eta_{ij} \sin(\phi_i(t) - \phi_j(t) - \phi_{ij})
\end{aligned} \tag{5.2}$$

where  $m_i$  is the number of adjacent joints to the joint  $i$ , and  $\eta_{ij}$  is the coupling constant between the  $i$ th and  $j$ th adjacent joints.  $\Omega$  and  $A_{\rho}$  are the steady-state frequency and amplitude for  $\omega(t)$  and  $\rho(t)$ , and  $\gamma_{\omega}$  and  $\gamma_{\rho}$  are constant parameters. The parameters  $\psi_{\omega}$  and  $\psi_{\rho}$  are constant values for adjusting the effect of physical interaction in iCPG dynamics. The thresholds  $\omega_{th+}$  and  $\rho_{th+}$  are the positive threshold of  $\omega(t)$  and  $\rho(t)$ , respectively, that trigger the deceleration term with gains  $k_{\omega}$  and  $k_{\rho}$  to avoid reaching the maximum allowable frequency  $\omega_{\max}$  and amplitude  $\rho_{\max}$ . Furthermore,  $u(\cdot)$  is a step function that activates the log functions when the aforementioned thresholds are crossed. In real experiments with the able-bodied person wearing the Indego exoskeleton, these values will be determined based on the users' comfort.

Most notably, and the focus of this paper, is the effective pHRI energy,  $E_{\text{eff}}(t)$ , which is a function of the pHRI energy, and is determined via the TD3 algorithm, which will be presented in Sec. 5.3.1 [43]. The pHRI energy of joint  $i$ ,  $E_i(t)$ , is

$$E_i(t) = \int_0^t \tau_{\text{HRI},i}(t) \dot{q}_i(t) dt \tag{5.3}$$

where  $\dot{q}_i(t)$  is the velocity of the  $i$ th joint and  $\tau_{\text{HRI},i}(t)$  is the estimated human interaction torque on the  $i$ th joint, which is estimated using a trained neural network based on the method described in Sharifi et al. [18]. The total pHRI energy ( $E(t)$ ) is the summation of the interaction energies of all joints.

Using a Fourier series expansion, the described iCPG outputs are transformed into a reference locomotion trajectory,  $q_i(t)$ , for the  $i$ th joint of the exoskeleton:

$$q_i(t) = \xi_i(t) + \rho_i(t) \sum_{k=1}^{N_i} (a_{i_k} \cos k\phi_i(t) + b_{i_k} \sin k\phi_i(t)) \tag{5.4}$$

where  $N_i$  is the number of terms in Fourier’s series and  $a_{i_k}$  and  $b_{i_k}$  are the coefficients of that. The frequency  $\omega(t)$ , and amplitude  $\rho_i(t)$  of walking, and also phase  $\phi_i(t)$  of each joint’s oscillatory motion (see Eq. (5.2)) are modified in real-time via the iCPG-based update rules in (5.2).

### 5.3 Implementation of an RL agent to adjust energy contributions for trajectory shaping

Deep reinforcement learning was used to modify pHRI energy ( $E(t)$ ) and determine effective energy values ( $E_{\text{eff}}$ ) in (5.2) based on the physical interaction behaviour of lower-limb exoskeleton users. The RL algorithm employed in this project and the reward function used for determining the  $E_{\text{eff}}$  are introduced in the following subsections.

#### 5.3.1 Deep reinforcement learning

RL is a learning strategy that attempts to model an agent interacting with its environment while learning reward-maximizing behaviour. At each time step  $t$  in a given state  $s \in \mathcal{S}$ , an RL agent selects an action  $a \in \mathcal{A}$  with respect to a policy  $\pi : \mathcal{S} \rightarrow \mathcal{A}$ , and receives a reward  $r_t$  and transitions to a new state  $s' \in \mathcal{S}$  in its environment. The return,  $R_t$ , is defined as the discounted sum of rewards  $R_t = \sum_{k=t}^T \gamma^{k-t} r(s_k, a_k)$ , where  $\gamma$  is a discount factor determining the relative importance of future rewards and  $T$  is the end of an episode. The objective in reinforcement learning is to find the optimal policy which maximizes the expected return. To this end, the agent learns a value function  $Q$ , which maps the agent’s state and action to expected return,  $Q(s, a) \in \mathbb{R}, s \in \mathbf{S}, a \in \mathbf{A}$  [43].

A TD3 strategy was used to formulate the RL problem in this chapter. The characteristics of the TD3 algorithm make it a good fit for the personalized trajectory generation problem in this study. In particular, TD3 uses double critic networks to approximate the reward from a given state and action using the Bellman equation in

terms of the discounted sum of expected TD errors,  $\delta$  [43]:

$$\begin{aligned}
Q_\theta(s, a) &= r_t + \gamma \mathbb{E}[Q_\theta(s_{t+1}, a_{t+1})] - \delta_t \\
&= r_t + \gamma \mathbb{E}[r_{t+1} + \gamma \mathbb{E}[Q_\theta(s_{t+2}, a_{t+2})]] - \delta_t \\
&= \mathbb{E}_{\tau \sim \pi_\phi} \left[ \sum_{i=t}^T \gamma^{i-t} (r_i - \delta_i) \right]
\end{aligned} \tag{5.5}$$

where  $\sum_{i=t}^T \gamma^{i-t} (r_i - \delta_i)$  is the discounted sum of returns,  $Q_\theta(s, a)$  is the differentiable function approximator with the parameter  $\theta$ , and  $\mathbb{E}[\cdot]$  is the expectation from a sequence of states and actions following the policy  $\pi_\phi$ . During training, an actor network and two critic networks are initialized with random parameters  $(\phi, \theta_1, \theta_2)$ . To prevent divergence of agent behavior and ensure stability, target networks with parameters  $(\phi', \theta'_1, \theta'_2)$  are initialized and periodically updated through soft target updates. Additionally, a replay buffer  $\mathcal{B}$  is initialized to record a subset of tuples of the agent’s experiences  $(s_t, a_t, r_t, s_{t+1})$ , which are later randomly sampled for training updates to break temporal correlations in the data. At each timestep, an action is selected by the policy with added exploration noise to encourage exploration and prevent overfitting [43]:

$$a \sim \pi_\phi(s) + \epsilon, \quad \epsilon \sim \mathcal{N}(0, \sigma) \tag{5.6}$$

where  $\epsilon$  is the exploration noise sampled from a normal distribution with standard deviation  $\sigma$ . The resulting transition tuple  $(s_t, a_t, r_t, s_{t+1})$  is then stored in the replay buffer  $\mathcal{B}$ . Next, an action is selected with target policy smoothing applied. The action is clipped to the action space, and the noise is clipped between constants  $\pm c$  to keep the target close to the original action [43]:

$$\tilde{a} \leftarrow \text{clip}(\pi_{\phi'}(s') + \text{clip}(\epsilon, -c, c), a_{\text{low}}, a_{\text{high}}), \quad \epsilon \sim \mathcal{N}(0, \tilde{\sigma}) \tag{5.7}$$

Using this estimate of  $\tilde{a}$ , the target Q values from the double critic networks are computed using the smaller value of the two networks to prevent maximization bias. The loss function is then computed for the two critic networks by computing the

mean squared error between each critic and the target Q value. The networks are optimized using backpropagation [43]:

$$\begin{aligned} y &\leftarrow r + \gamma \min_{i=1,2} Q_{\theta'_i}(s', \tilde{a}) \\ \theta_i &\leftarrow \operatorname{argmin}_{\theta_i} N^{-1} \sum (y - Q_{\theta_i}(s, a))^2 \end{aligned} \quad (5.8)$$

The actor policy is optimized periodically when  $t \bmod d = 1$ , where  $d$  is the number of steps before an update. The mean of the Q values from the critic networks is used in the backpropagation of the actor networks [43]:

$$\nabla_{\phi} J(\phi) = N^{-1} \sum \nabla_a Q_{\theta_1}(s, a) |_{a = \pi\phi(s)} \nabla_{\phi} \pi_{\phi}(s) \quad (5.9)$$

where  $\nabla_{\phi} J(\phi)$  is the gradient of the expected return  $J(\phi)$  following the target policy  $\pi_{\phi}$ . Finally, the target networks are updated using a soft update as follows [43]:

$$\begin{aligned} \theta'_i &\leftarrow \tau \theta_i + (1 - \tau) \theta'_i \\ \phi' &\leftarrow \tau \phi + (1 - \tau) \phi' \end{aligned} \quad (5.10)$$

where  $\tau$  is the soft update coefficient selected to provide stable updates in the policy network.

### 5.3.2 Interaction energy modification via RL

The objective of the TD3 algorithm in our study was to control the effective pHRI energy,  $E_{\text{eff}}(t)$ , in (5.2) to facilitate reaching the user's desired locomotion trajectory via iCPGs. In particular, we designed a reward function,  $\mathcal{R}$ , which the RL agent attempted to maximize. In this section, we will first outline the reward function for the TD3 algorithm and then discuss how the proposed reward function can address challenges in different scenarios that the agent may face.

The state space for the RL agent is the pHRI energy ( $E(t)$ ) in Eq. (5.3) and its average ( $E_{\text{avg}}(t)$ ); and frequency ( $\omega$ ) in Eq. (5.2) and its average ( $\omega_{\text{avg}}$ ) which represents RL estimation about user's desired frequency. The action space is the effective HRI energy ( $E_{\text{eff}}(t)$ ) used in (5.2).

The following reward function was used to identify the optimal value of effective interaction energy for the user’s desired walking pattern via iCPGs:

$$\mathcal{R} = -\left(\mathcal{K}_E[E(t) - E_{\text{avg}}(t)]^2 + \mathcal{K}_\omega[\omega(t) - \omega_{\text{avg}}(t)]^2 + \mathcal{K}_{\ddot{\omega}}[\ddot{\omega}(t)]^2 + \mathcal{R}_p + \mathcal{R}_E\right) \quad (5.11)$$

where  $\mathcal{K}_E$ ,  $\mathcal{K}_\omega$ , and  $\mathcal{K}_{\ddot{\omega}}$  are constant values and  $\mathcal{R}_p$  and  $\mathcal{R}_E$  are defined as follows

$$\mathcal{R}_p = \begin{cases} \mathcal{P}_p, & \omega \notin [\omega_{\min}, \omega_{\max}] \text{ or } \rho \notin [\rho_{\min}, \rho_{\max}] \\ 0 & \text{otherwise} \end{cases} \quad (5.12)$$

$$\mathcal{R}_E = \begin{cases} \mathcal{P}_E, & (E(t) - E(t - \tau_E)) > \epsilon_E \\ 0, & \text{otherwise} \end{cases} \quad (5.13)$$

where  $\mathcal{P}_p > 0$  and  $\mathcal{P}_E > 0$  are constant values and  $\omega_{\max}$ ,  $\omega_{\min}$ ,  $\rho_{\max}$ , and  $\rho_{\min}$  are pre-defined safety thresholds to provide safe locomotion patterns.  $E(t)$  is the current pHRI energy state,  $E(t - \tau_E)$  is a delayed version of HRI energy and  $\tau_E$  represents the amount of delay. A step is detected if the difference  $E(t) - E(t - \tau_E)$  is greater than a threshold  $\epsilon_E$ . Note that this threshold value will be determined by trial and error in real experiments with the exoskeleton and able-bodied user.

$\mathcal{R}_p$  is the safety term that encourages RL agent to avoid transitions to unsafe states. The terms of difference between actual energy and frequency with their average values ( $E(t) - E_{\text{avg}}(t)$  and  $\omega(t) - \omega_{\text{avg}}(t)$ ), and the acceleration of the frequency ( $\ddot{\omega}(t)$ ), play an important role when the frequency is close to the user’s desired value and system is almost in steady state. However, they can make the system less responsive by introducing lower  $E_{\text{eff}}$ , which has been resolved by adding the term  $\mathcal{R}_E$ , which penalizes based on the number of interactions that a user has applied.

## 5.4 Results and Discussion

The hyperparameters for the TD3 algorithm were set experimentally, and they included a random seed of 10, starting exploration time steps of 64 on a random policy, standard deviation of 0.1 from a Gaussian distribution for exploration noise, batch size of 512,  $\gamma$  of 0.99,  $\tau$  of 0.005, policy noise of 0.2 from a Gaussian distribution for

critic updates, and policy update frequency of 2. The averages were calculated with a moving average with a window size of 10 s, and  $\tau_E$  0.05 s. The iCPG parameters were all set based on Sharifi et al. [19], except  $\psi_\omega$  and  $\psi_\rho$  were set 0.0072 and 0.0096, respectively in simulations and  $\psi_\omega = 0.0007$  and  $\psi_\rho = 0.0009$  in experiments.

### 5.4.1 Simulations

The simulation environment was created in MATLAB Simulink R2022a. The environment consisted of a frequency-dependent pHRI energy input in (5.3), which increases or decreases in rectangular steps at fixed intervals. The desired frequency was manually set and hidden from the RL agent. If the current frequency was below the desired frequency, the pHRI energy input increased until the desired frequency was obtained, and vice versa. The pHRI energy input remained constant while the frequency is close enough to the desired frequency. The RL agent receives the current state from the environment and takes an action that modulates the pHRI energy ( $E$ ) to determine  $E_{\text{eff}}$ . Simulations were divided into a training and testing phase, where the RL agent modulated the pHRI energy to meet the desired frequency. In both training and testing, the desired frequency was changed every 10 s. The training phase involved five episodes of training, with each episode lasting 30 s. Each episode consisted of 300 time steps corresponding to a sampling rate of 10 Hz. The testing phase consisted of 30 trials with the trained model, again for 30 s.

In real applications were the iCPG was initialized using experimental user data, and then the dynamics were updated when a new user interacted with the exoskeleton. Therefore there were two possible scenarios that need to be considered in the simulations. Firstly, there was the case of a new user with weaker muscles generating smaller interaction torques than the user with whom the initialization was performed. This is the main scenario we are trying to address in this research, as people with mobility impairments often have weaker muscles and are more easily fatigued by interacting with the exoskeleton than neurologically-intact individuals. The second case

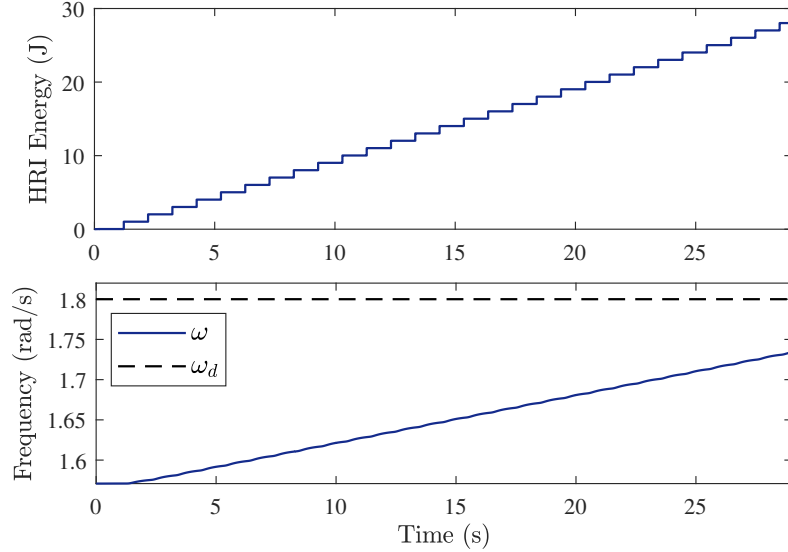


Figure 5.2: Variation of pHRI energy and frequency of walking for the weak muscle scenario without RL refinements.

was when a new user has stronger muscles than the person for whom the exoskeleton was initialized.

1. Weak muscles (small stepwise  $\tau_{\text{HRI}}$ ): This scenario represents individuals with weak muscles who apply rectangular pulses of  $\tau_{\text{HRI}}$  insufficient alone to reach their desired frequency. Note that the amplitude of walking is a function of the gait frequency. A constant stepwise torque input is simulated using the rect function with a positive unity gain for frequencies below the desired frequency and a positive unity gain for those greater than the desired values. To aid the user, a penalty term,  $\mathcal{R}_E$ , is applied for jumps in  $E_{\text{HRI}}$  to incentivize the RL agent to choose actions which minimize the number of jumps. This penalty plays the most critical role in cases where the user’s muscles are weak, so the RL agent amplifies the interaction energy to reach the user’s desired walking speed faster. Also, the other elements of the reward function improve the agent’s behaviour when it is close to the desired values.

The results for weak muscle scenario in the absence of RL modifications show that the user could not reach the desired frequency (1.8 rad/s) after 30 s (Fig. 5.2). However, the user reached the desired frequencies in less than five seconds by integrating

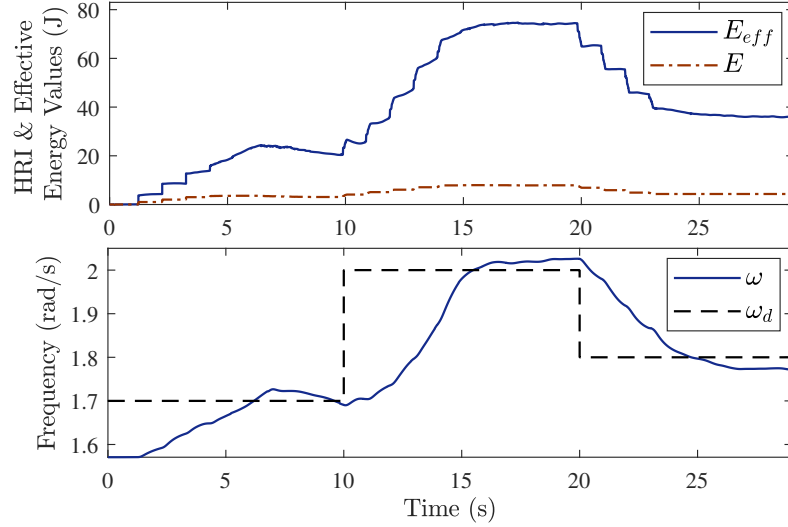


Figure 5.3: Variation of pHRI energy due to an RL agent selecting an effective energy to modify the frequency of walking for the weak muscle scenario.

an RL agent introduced in the effective energy term in the iCPG structure. As seen in Fig. 5.3, the RL agent amplified the user’s interaction energy,  $E(t)$  (brown dashed-dot line), and suggested higher values for the effective energy,  $E_{\text{eff}}(t)$  (solid blue line). This amplification rate is lower when the user is close to the steady-state behaviour (7-10s, 18-20s, and 27-30s). This is because of fewer jumps in this period (i.e., fewer jump penalties,  $\mathcal{P}_E$ ), which forces the agent to pay more attention to the other elements of the reward function. Note that the desired frequencies for the training phase for the weak muscle case was 2 rad/s, 1.7 rad/s, and 2 rad/s in this order. The testing phase had desired frequencies of 1.7 rad/s, 2 rad/s, and 1.8 rad/s, and acceptable frequency range of  $\pm 0.05$  rad/s around the desired frequency. The control case had the same acceptable frequency range.

2. Strong muscles (large stepwise  $\tau_{\text{HRI}}$ ): This scenario represents users with strong muscles who apply rectangular pulses of  $\tau_{\text{HRI}}$  to reach their desired frequency. The estimation of the desired values in RL were chosen as the average value over a constant time window. Our approach for the reward function was to minimize the sum of the mean squared error between the actual and desired  $E_{\text{HRI}}$  and iCPG frequency,

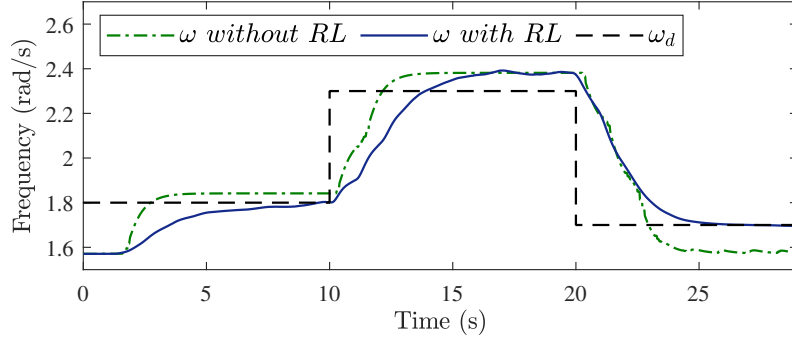


Figure 5.4: Variations of gait frequency in the absence and presence of RL modification for the strong muscle scenario.

i.e., maximizing the reward function. For the strong muscle scenario, the desired frequencies for the training phase were 2.2 rad/s, 1.7 rad/s, and 2.2 rad/s in this order. The testing phase had desired frequencies of 1.8 rad/s, 2.3 rad/s, and 1.7 rad/s. An acceptable frequency range of  $\pm 0.15$  rad/s around the desired frequency was implemented to prevent oscillations about the desired frequency. The control case had the same acceptable frequency range. The results showed that the trained agent could facilitate reaching desired frequency values by adjusting the effective energy over time (see Fig. 5.4). As it can be seen in Fig. 5.4, the integral of error between the user’s desired frequency and iCPGs output in the steady-state period (7-10 s, 18-20 s, and 27-30 s) was decreased by 65% for the case of using effective energy values which was determined via RL. Note that the desired frequency is hidden from the RL agent.

### 5.4.2 Experimental evaluations

The experimental set-up in Fig. 5.6a was used to evaluate the effectiveness of our proposed iCPG for lower-limb exoskeletons. A 29-year-old able-bodied user wore the Indego lower-limb exoskeleton (Parker Hannifin Corporation, Macedonia, OH). The user was asked to apply physical interactions to the exoskeleton joints to change the walking frequency to the user’s desired values. The desired frequency was hidden from the RL agent, and the agent used the average value of iCPGs frequency to estimate the user’s desired frequencies. Three different experiments were performed. The first

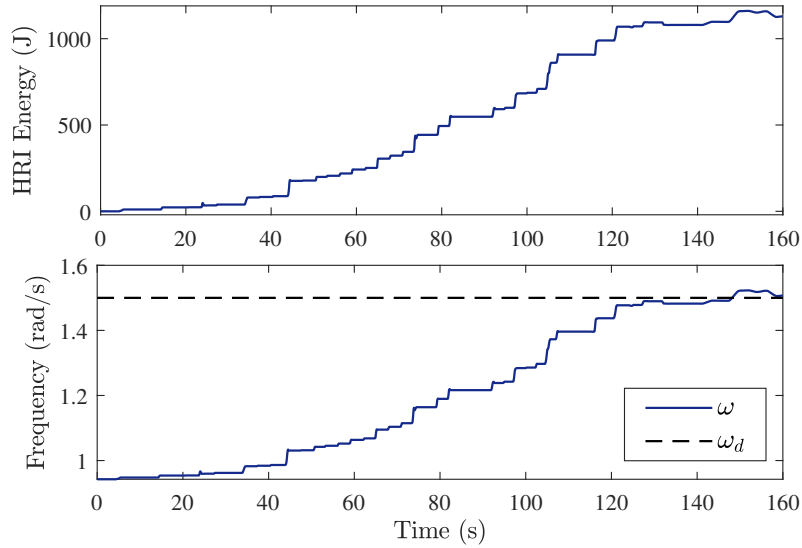


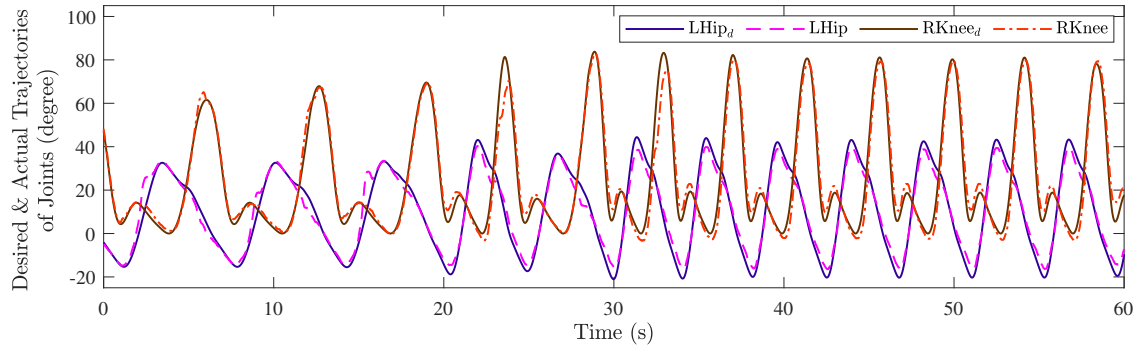
Figure 5.5: pHRI energy and walking frequency variations for a user interacting with a lower-limb exoskeleton in the absence of RL modifications.

experiment was the control case, which used only ACPGs without an RL agent. The second experiment trained the RL agent. In this experiment, the user interacted with the exoskeleton for 150 s to reach different desired frequency values. In addition, the actor-critic networks in the TD3 algorithm (see Sec. 5.3) were trained in this period and used in the final experiments for tuning the effective energy values. Note that the whole process for training RL can also be performed in our developed simulation environment for safety reasons.

As shown in Fig. 5.5, the user reached their desired frequency of 1.5 rad/s after about 150 s and increased the pHRI energy level to more than 1000 J by applying continuous interaction energies. Continuous energy inputs were necessary because the ACPG initialization was performed with a different user with much stronger muscles. However, the RL agent and iCPGs resolved this issue by adjusting the pHRI energy value and introducing effective energy in Fig. 5.7. As observed in Fig. 5.7, the maximum pHRI energy applied by the user (brown dashed-dot line) was about 125 J. However, the RL agent amplified that value (solid blue line) to about 1000 J, which facilitated reaching the user’s desired frequency. The results for the frequency showed



(a)



(b)

Figure 5.6: a) Experimental set-up: A 29-year-old neurologically-intact user wearing the Indego lower-limb exoskeleton, b) Desired and actual trajectories generated via iCPGs for the left hip and right knee joints.

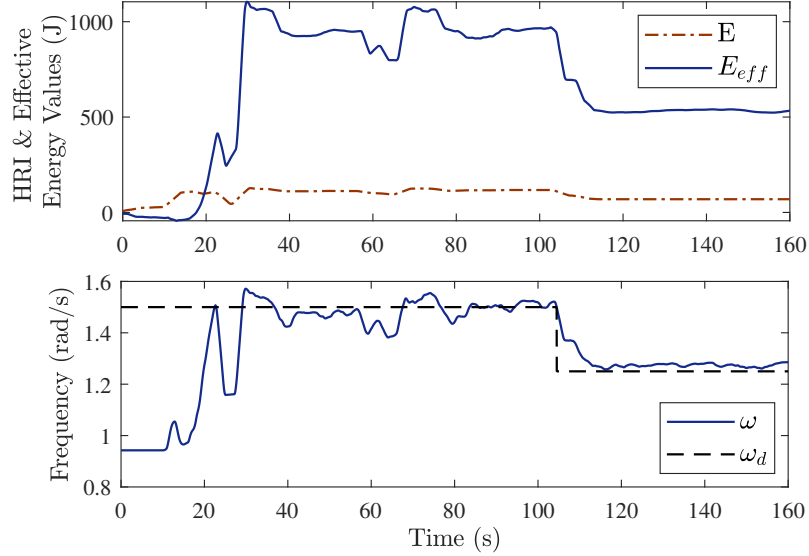


Figure 5.7: pHRI energy, effective energy, and walking frequency variations for a user interacting with a lower-limb exoskeleton in the presence of RL modifications.

that users could reach their desired frequencies on average in 10 s with iCPGs, only by modifying their effective energy. Furthermore, comparing the rate of amplification of pHRI energy shows that the RL agent introduced a lower energy amplification rate for the period that the user tended to walk at a constant frequency, which provided a smoother walking experience for the user.

The amplitude, frequency, and phase values determined by iCPGs were translated to the desired trajectories of joints via Fourier series in (5.4). Fig. 5.6b shows the results for the desired and actual trajectories of joints for the first 60 s of walking. The RL & iCPGs-based generated desired trajectories have been commanded to a PD position control to be tracked. As depicted in Fig. 5.6b, the maximum error between desired and actual trajectories was about  $6^\circ$  for the knee joint and  $4^\circ$  for the hip joint, which shows an appropriate tracking performance.

## 5.5 Conclusion

This study introduced iCPGs, which combined reinforcement learning with ACPGs to generate user-specific gait trajectories. The previously introduced ACPG algorithm

could change gait trajectories in response to a user's physical interaction. However, the effectiveness of ACPGs was limited to precise parameter identification and a lack of considerable change in the interaction behaviour of users. The proposed iCPGs employed RL to learn a user's interaction behaviour in real-time and adjusted the pHRI energy to facilitate reaching a user's desired gait pattern. The simulation results showed that the proposed RL agent could modify pHRI energy and introduce an effective energy term to the iCPGs, removing the need for precise parameter identification and fixed interaction behaviour. Furthermore, the results provided evidence for the effectiveness of the proposed iCPGs in scenarios of having weaker or stronger muscles than the user that has been used for identifying the parameters. Finally, the experimental results showed that the method could be used for personalized motion planning of lower-limb exoskeletons.

# Chapter 6

## Locomotion Planning for Lower-Limb Exoskeletons via Intelligent Central Pattern Generators and Reinforcement Learning

### 6.1 Introduction

Exoskeletons have emerged as promising tools in assisting individuals with neurological impairments, providing them with increased mobility, independence, and quality of life. These wearable devices can be used to assist patients experiencing neurological conditions such as stroke, spinal cord injuries, or multiple sclerosis. By augmenting or restoring impaired motor functions, exoskeletons assist users to augment their control over their movements, enhancing their ability to walk, stand, and perform daily activities [13]. The integration of advanced sensor technology, real-time feedback mechanisms, and adaptive algorithms in exoskeleton design allows for personalized and intuitive user interaction, promoting neuroplasticity and facilitating rehabilitation [13]. Furthermore, exoskeletons enhance the autonomy of individuals with functional impairments to participate more actively in social and occupational settings, fostering inclusivity and empowerment within their communities [99].

In this chapter, we present a simulation environment designed to emulate human

actions for generating physical interaction torques within the context of exoskeleton motion planning software. This innovative environment takes into account the maximum achievable torque and replicates human behavior when engaging with an exoskeleton, accounting for the applicable range of interactions and introducing an element of randomness in the applied torque. The proposed simulation environment can be used to train the RL agent before applying it to the real exoskeleton, which can prevent most of the possible unsafe actions from the RL agent. In addition, by combining the adaptability of RL with the rhythmic motion generation capabilities of ACPGs, we propose a new iCPGs for personalized motion planning of exoskeletons. Our iCPGs uses a ACPG-based motion planner to generate initial gait trajectories and an RL agent to learn and adapt to the user’s target gait pattern. The iCPG provides viability of walking and safety by generating predictable and synchronized gait patterns, while the RL controller allows for adaptability and personalization by learning from the user’s interactions. The iCPGs presented in this chapter extend the framework introduced in Chapter 5, aiming for faster convergence and improved performance, particularly in the context of the strong muscle scenario discussed in Chapter 5. The ACPG structure and pHRI torque estimation method remain almost identical to those in Chapter 5. However, the main distinction lies in the reinforcement learning (RL) states and actions utilized. Furthermore, the simulation environment proposed in this chapter enhances the previously introduced environment in Chapter 5, aiming to achieve behavior more closely resembling human pHRI with an exoskeleton. The summary of contributions of this study is as follows:

- For the first time, we introduce a simulation environment that imitates human behavior in having physical interactions with exoskeletons. This can be used for training RL algorithms or collecting data for training any kind of supervised learning algorithm.
- A new reward function was designed and implemented, which can facilitate

personalized locomotion planning for lower-limb exoskeletons. The new reward function has better performance in learning a strong muscle scenario in comparison with our previously developed algorithm [100]. The strong muscle scenario refers to the case that the user’s interaction energy is larger than the energy value required for reaching the desired frequency of locomotion. In other words, the user will always oscillate around the desired value by applying physical interactions.

- A new structure has been introduced for calculating the user/exoskeleton interaction energy, which has better stability in high frequencies of walking compared to our past work in Sharifi *et al.* [18].

The rest of this chapter is organized as follows. The simulation environment is introduced in Sec. 6.2. In Section 6.3, the proposed iCPGs and RL algorithms are described. The simulation and experimental evaluations of the developed intelligent motion planning scheme are presented and discussed in Sec. 6.4, and the concluding remarks are provided in Sec. 6.5.

## 6.2 Simulation Environment

For user safety, the RL algorithm needs to be first trained in a simulation environment rather than through actual experimentation on human users. For the first time, we propose a simulation environment which can mimic human behavior in changing an exoskeleton’s gait pattern via physical human-robot interaction. The proposed simulation environment receives the body specification of the user whom training is going to be done on and the desired gait pattern that the users will have in their mind. Note that these desired values are all hidden from the RL algorithm during the training process. The schematic of the proposed simulation environment is shown in Fig. 6.1.

The simulation environment user is required to input desired gait parameters, the

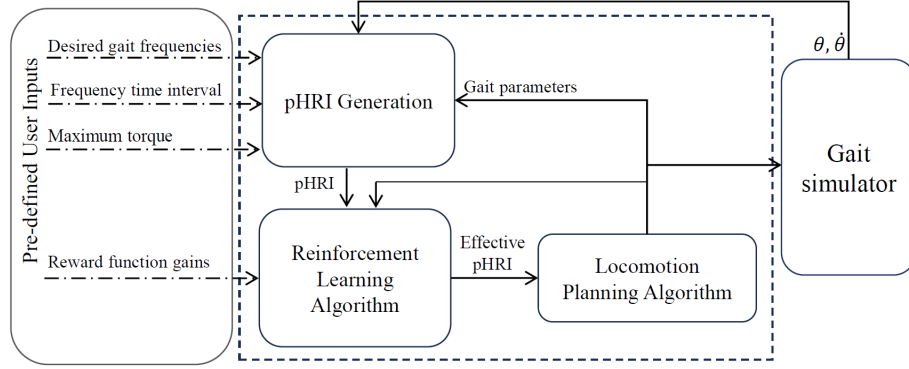


Figure 6.1: Schematic of the proposed simulation environment.

corresponding time periods for each desired value to be commanded to the physical human-robot interaction (pHRI) generation section, and the maximum torque allowed for each interaction in the simulator. The simulator can take either the amplitude or the frequency of walking as the desired gait parameter, provided as a vector with arbitrary length containing different values. Each value will be applied for the time period that is defined as a input to the simulator.

To enhance the realism, the pHRI torque generated by the simulator varies and is not consistently equal to the maximum input torque. Instead, the simulator calculates the pHRI torque as 90% of the maximum torque, with an added random number ranging from zero to 10%. Note that this level of randomness in pHRI generation can be tuned to any arbitrary value by the simulator user. This approach introduces variations in torque generation similar to human behavior when interacting with exoskeletons. Additionally, the simulator user must input the elements of any reinforcement learning reward function that is being used in the simulator.

The pHRI generation section operates by taking in both the desired gait parameters provided by the user and the simulated gait parameters obtained from the gait simulator. By comparing these values, the simulator applies either positive or negative interaction torques to compensate for any differences between the actual and desired parameters. Notably, torque exertion will cease when the error between the actual and desired gait parameters falls within a predefined threshold window. This

is the same behavior that exoskeleton users do in order to change the behavior of the exoskeleton.

Moreover, in cases where the user has input multiple gait parameters within the input vector, the simulator will modify the desired values under two specific conditions. Firstly, if the elapsed time for a particular gait parameter value surpasses the specified time interval. Secondly, if the error between the actual and desired gait parameter value falls within the pre-defined threshold value. In essence, the simulator will refrain from changing the desired gait parameter value when the actual gait parameter fails to reach the desired value. This aspect is crucial in effectively training RL algorithms, because it allows the agent to keep exploring until reaching specified desired value.

The pHRI torque and gait parameters generated are employed as inputs for the RL algorithm, enabling the creation of states and training the algorithm to generate adjusted pHRI torque values. Notably, this particular section of the simulator is implemented using Python code, and it communicates with the rest of the code via UDP communication, with the remaining code developed in MATLAB/Simulink. The decision to host the RL code within the Python environment streamlines the process for users to deploy various algorithms with convenience.

After receiving the modified effective energy from the RL agent, the locomotion planning algorithm proceeds to update the gait parameters. These newly adjusted gait parameters are then inputted into the gait simulator, specifically employing iCPGs in this research, which calculates the position and velocity for each joint. The gait simulator utilizes multiple Fourier series, with each series responsible for generating the trajectory of its corresponding joint.

The pHRI torque generation component operates by receiving the angular positions of the joints and exerts interaction only when the joints are in a position capable of exerting force. Put differently, the simulation environment refrains from applying interaction torques in specific body configurations where it is impossible to create

physical interactions in the real world, such as during the double stance phase. This design ensures that the simulator’s physical interaction behavior closely resembles human behavior.

## 6.3 Methodology

By combining RL and adaptable CPGs (ACPGs) [18], we introduce intelligent CPGs (iCPGs) that aim to enhance motion planning capabilities, adapting to individual users’ needs and interactions and offering more robust and efficient exoskeleton control during walking activities.

### 6.3.1 Intelligent Central Pattern Generators

The dynamics of a lower-limb exoskeleton and a human user is:

$$M_q(q)\ddot{q} + C_q(q)\dot{q} + G_q(q) = \tau_{\text{mot}} + \tau_{\text{hum,p}} + \tau_{\text{hum,a}} \quad (6.1)$$

where  $M_q(q)$ ,  $C_q(q)$ , and  $G_q(q)$  respectively stand for the inertia matrix, the matrix encompassing Coriolis, centrifugal, and damping terms, and the vector representing gravitational torques. The vector  $q$  signifies the exoskeleton’s joint positions, while  $\tau_{\text{mot}}$  denotes the motor torque applied to the exoskeleton. Additionally, the terms  $\tau_{\text{hum,p}}$  and  $\tau_{\text{hum,a}}$  correspond to the passive and active components of the human torque vector, respectively.

In our previous work [18–20], the ACPG was introduced for real-time modification of the exoskeleton joint trajectories during walking. While the ACPG could provide adaptability for the gait trajectory of exoskeletons based on pHRIs, still the human user needed to adapt to the ACPG dynamics. To address this challenge and enable personalized motion planning, we propose an innovative integration of RL with ACPGs, resulting in a novel approach termed iCPGs (illustrated in Fig. 6.1). The iCPG dynamics encompass the adaptation of overall locomotion frequency  $f(t)$ , oscillation amplitude  $\gamma(t)$ , and phase variation of each joint  $\theta_i(t)$ , and can be expressed

as follows:

$$\begin{aligned}
\dot{\theta}_i(t) &= f(t) + \sum_{j=1}^{m_i} v_{ij} \sin(\theta_i(t) - \theta_j(t) - \phi_{ij}) \\
\dot{f}(t) &= \mu_f \left( \frac{\mu_f}{4} \left( F + \eta \sum_{k=1}^n E_{\text{mod}_k} - f(t) \right) - \dot{f}(t) \right) - k_f \frac{DZ^+(f(t) - f_{th})}{(f_{\max} - f(t))^3} \\
\dot{\gamma}(t) &= \mu_\gamma \left( \frac{\mu_\gamma}{4} \left( A + \eta \sum_{k=1}^n E_{\text{mod}_k} - \gamma(t) \right) - \dot{\gamma}(t) \right) - k_\gamma \frac{DZ^+(\gamma(t) - \gamma_{th})}{(\gamma_{\max} - \gamma(t))^3}
\end{aligned} \tag{6.2}$$

Here,  $n$  is the number of all joints and  $m_i$  denotes the number of adjacent joints to the joint  $i$ .  $f_{\max}$  and  $\gamma_{\max}$  are the maximum frequency and amplitude values, taking into consideration both the exoskeleton's capabilities and user limitations. Passing the threshold values ( $f_{th}$  and  $\gamma_{th}$ ) will trigger the dead-zone function ( $DZ^+$ ) and that will prevent passing the maximum frequency and amplitude (see [20] for more details).  $v_{ij}$ ,  $\mu_f$  and  $\mu_\gamma$  are constant values that play a crucial role in fine-tuning the system's agility to reach new amplitude and frequency values.

A primary focus of this research is the concept of modified human-robot interaction energy, denoted as  $E_{\text{mod}}(t)$ . This energy function is derived from three crucial elements:

1. The time-varying gain ( $\mathcal{K}_{RL}$ ) determined through the twin delayed DDPG (TD3) algorithm (to be described in Section 6.3.2).
2. The pHRI torque ( $\tau_{\text{pHRI}}$ ), computed using a neural network-based method as described by Sharifi et al. [18].
3. The sign of joint velocity ( $\dot{q}_i$ ). Unlike what was repeated in our previous studies [18–20, 100], the joint velocity was replaced with the sign of the joint velocity in the calculation of the physical interaction energy. This aims to prevent unintentional variations in gait parameters at higher walking speeds.

$$E_{\text{mod}_i}(t) = \mathcal{K}_{RL} \int_0^t \tau_{\text{pHRI},i}(t) \text{sgn}(\dot{q}_i(t)) dt \tag{6.3}$$

To transform the outputs of the described iCPG into a reference locomotion trajectory,  $q_i(t)$ , for the  $i$ th joint of the exoskeleton, a Fourier series expansion was employed:

$$q_i(t) = \xi_i(t) + \rho_i(t) \sum_{k=1}^{N_i} (a_{i_k} \cos k\phi_i(t) + b_{i_k} \sin k\phi_i(t)) \quad (6.4)$$

In this equation,  $N_i$  represents the number of terms in the Fourier series, and  $a_{i_k}$  and  $b_{i_k}$  are the corresponding coefficients. The frequency  $f(t)$ , amplitude  $\gamma_i(t)$  of walking, and the phase  $\theta_i(t)$  of each joint’s oscillatory motion (as shown in Eq. (6.2)).

### 6.3.2 Implementation of an RL agent to adjust energy contributions for trajectory shaping

Deep RL was used to modify pHRI torque ( $\tau_{\text{pHRI}}$ ) and determine modified energy values ( $E_{\text{mod}}$ ) in (6.3). The RL algorithm employed in this project and the reward function used to determine the  $E_{\text{mod}}$  are introduced in the following subsections.

#### Reinforcement learning

RL is an approach that seeks to emulate an agent’s interaction with its environment as it learns to optimize reward-gaining actions. In a specific state  $s \in \mathcal{S}$  at each time step  $t$ , an RL agent chooses an action  $a \in \mathcal{A}$  according to a policy  $\pi : \mathcal{S} \rightarrow \mathcal{A}$ , and obtains a reward  $r$  while transitioning to a new state  $s' \in \mathcal{S}$ . The return,  $R_t$ , is characterized as the discounted accumulation of rewards  $R_t = \sum_{k=t}^T \gamma^{k-t} r(s_k, a_k)$ , where  $\gamma$  is a discount factor that establishes the significance of future rewards and  $T$  signifies the episode’s conclusion. The goal in RL is to identify the optimal policy that maximizes the expected return following the policy. To this end the agent learns a value function  $Q$ , which associates the agent’s state and action with expected return,  $Q(s, a) \in \mathbb{R}, s \in \mathbf{S}, a \in \mathbf{A}$ . In this study, we utilize deep RL to adjust pHRI torque  $\tau_{\text{pHRI}}$  and ascertain modified energy values  $E_{\text{mod}}$  in (6.2) based on the physical interaction patterns of lower-limb exoskeleton users. The TD3 algorithm which was

---

**Algorithm 1** TD3 [43]

---

Initialize critic networks  $Q_{\theta_1}, Q_{\theta_2}$ , and actor network  $\pi_\phi$  with random parameters  $\theta_1, \theta_2, \phi$   
Initialize target networks  $\theta'_1 \leftarrow \theta_1, \theta'_2 \leftarrow \theta_2, \phi' \leftarrow \phi$   
Initialize replay buffer  $\mathcal{B}$   
**for**  $t = 1$  **to**  $T$  **do**  
    Select action with exploration noise  $a \sim \pi_\phi(s) + \epsilon$ ,  
     $\epsilon \sim \mathcal{N}(0, \sigma)$  and observe reward  $r$  and new state  $s'$   
    Store transition tuple  $(s, a, r, s')$  in  $\mathcal{B}$   
  
    Sample mini-batch of  $N$  transitions  $(s, a, r, s')$  from  $\mathcal{B}$   
    Select action with target policy noise:  
     $\tilde{a} \leftarrow \pi_{\phi'}(s') + \epsilon, \quad \epsilon \sim \text{clip}(\mathcal{N}(0, \tilde{\sigma}), -c, c)$   
    Use Clipped Double Q-learning target:  
     $y \leftarrow r + \gamma \min_{i=1,2} Q_{\theta'_i}(s', \tilde{a})$   
    Update  $\theta_i$  to minimize  $N^{-1} \sum (y - Q_{\theta_i}(s, a))^2 \{Q_{\theta_i}\}_{i=1}^2$   
    Update critics  $\theta_i \leftarrow \text{argmin}_{\theta_i} N^{-1} \sum (y - Q_{\theta_i}(s, a))^2$   
    **if**  $t \bmod d$  **then**  
        Update  $\phi$  by the deterministic policy gradient:  
         $\nabla_\phi J(\phi) = N^{-1} \sum \nabla_a Q_{\theta_1}(s, a)|_{a=\pi_\phi(s)} \nabla_\phi \pi_\phi(s)$   
        Update target networks:  
         $\theta'_i \leftarrow \tau \theta_i + (1 - \tau) \theta'_i$   
         $\phi' \leftarrow \tau \phi + (1 - \tau) \phi'$   
    **end if**  
**end for**

---

used to address the RL problem in this study is summarized in Algorithm 1 (for more details refer to Mehr *et al.* [100]).

### Reward function

The TD3 algorithm was used to modulate the pHRI torque, in (6.3) and generate modified interaction energy,  $E_{mod}$  to aid in achieving the user’s preferred locomotion frequency and amplitude through iCPGs. We formulated a reward function,  $\mathcal{R}$ , to achieve this objective. The state space and action space for our RL agent are defined as follows:

- *State Space.* Three states have been defined in this problem, including inter-action indicator, frequency ( $f(t)$ ) and average ( $f_{avg}(t)$ ) values of that over a

window of 200 sampling time.

- *Action Space.* The actions include the pHRI gain  $K_{RL}$  defined in (5.3). The raw action being generated with the RL agent is in the range of 0.01-10. In order to do the exploration in uniform space,  $K_{RL}$  is calculated based on the raw action as follows

$$\mathcal{K}_{RL} = \begin{cases} 0.2 * \text{action}_{\text{raw}}, & \text{action}_{\text{raw}} < 5 \\ 2 * \text{action}_{\text{raw}} - 9, & \text{action}_{\text{raw}} > 5 \end{cases} \quad (6.5)$$

The following reward function was used to identify the optimal value of pHRI gain and modified energy for the user's desired walking pattern via iCPGs:

$$\mathcal{R} = -(\mathcal{K}_i \text{Int}_{\text{pen}} + \mathcal{K}_f [f(t) - f_{\text{avg}}(t)]^2 + \mathcal{K}_g \text{Gain}_{\text{pen}} + \mathcal{R}_p) + \mathcal{K}_n \text{NoInt}_{\text{rew}} \quad (6.6)$$

where  $\mathcal{K}_i$ ,  $\mathcal{K}_f$ ,  $\mathcal{K}_g$ , and  $\mathcal{K}_n$  are constant values defining the weight of each element inside the reward function. The variable  $\text{Int}_{\text{pen}}$  represents the count of physical interactions that occurred before reaching the desired value, and as a result, no interaction torque is applied to the joints. This count is reset to zero if there were no interactions in the last two consecutive steps. By using this term, the agent is incentivized to minimize the number of physical interactions during its operations. The purpose of the  $\text{Gain}_{\text{pen}}$  value is to motivate the agent to employ the lowest achievable RL gain. It is essential to be mindful that utilizing extreme maximum or minimum gain values, although they may expedite reaching the desired values, can result in an overly agile or sluggish system, which is not desirable for exoskeleton users. The mathematical formulation of  $\text{Gain}_{\text{pen}}$  value is:

$$\text{Gain}_{\text{pen}} = \begin{cases} \exp(0.5 * (5 - \text{action}_{\text{raw}})), & \text{action}_{\text{raw}} < 5 \\ \exp(0.5 * (\text{action}_{\text{raw}} - 5)), & \text{action}_{\text{raw}} > 5 \end{cases} \quad (6.7)$$

$\mathcal{R}_p$  is the safety term that encourages our RL agent to avoid transitions to unsafe states and is mathematically defined as:

$$\mathcal{R}_p = \begin{cases} \mathcal{P}_p, & f \notin [f_{\text{min}}, f_{\text{max}}] \text{ or } \gamma \notin [\gamma_{\text{min}}, \gamma_{\text{max}}] \\ 0 & \text{otherwise} \end{cases} \quad (6.8)$$

where  $\mathcal{P}_P > 0$  is constant and  $\omega_{\max}$ ,  $\omega_{\min}$ ,  $\rho_{\max}$ , and  $\rho_{\min}$  are safety thresholds set *a priori* to ensure patient safety with the exoskeleton. Despite all of the previously introduced terms in the reward function, the term  $\text{NoInt}_{\text{rew}}$  incentivizes the agent for not having interaction. The mathematical formulation for calculating this term is:

$$\text{NoInt}_{\text{rew}} = \exp(0.1(t - T)) \tag{6.9}$$

where  $t$  represents the current time, and  $T$  is the time that system has detected no interactions in the previous two consecutive steps. The utilization of the  $\exp(\cdot)$  function is motivated by the intention to mitigate the inadvertent reinforcement of the system over an extended period when the user wishes to remain on their present trajectory.

## 6.4 Results and discussion

The simulation environment described in section 6.2 was utilized for training the RL agent under two distinct scenarios. The generated pHRI torque randomly varied from 1.9 to 2 N.m. The initial scenario involved a weak muscle condition, where the user’s muscles lacked the necessary strength to achieve the desired frequency within a reasonable time frame. This is the most prevalent scenario for clinical exoskeletons, which have been designed for users with mobility impairments. In the second scenario, the user’s muscles were stronger than those used to identify ACPG parameters. Consequently, a single physical interaction from the user led to a frequency higher than their intended target frequency. To elaborate more on the performance of the proposed algorithm, three able-bodied users performed several empirical experiments. Each user did four experiments including weak and strong muscle scenarios in the absence and presence of RL modifications.

iCPG parameters	$v_{h-h} = 0.0075$ , $v_{h-k} = 0.0075$ , $v_{k-h} = 0.0075$ , $\mu_f = 10\pi$ , $\mu_\gamma = 10\pi$ , $F = \pi/2$ , $A = 1$ , $f_{th} = 2.8$ , $f_{\max} = 3$ , $\gamma_{th} = 1.5$ , $\gamma_{\max} = 1.6$
RL parameters	$k_i = 4$ , $k_f = 0.1$ , $k_g = 0.3$ , $k_n = 150$ , $P_p = 1000$ ,

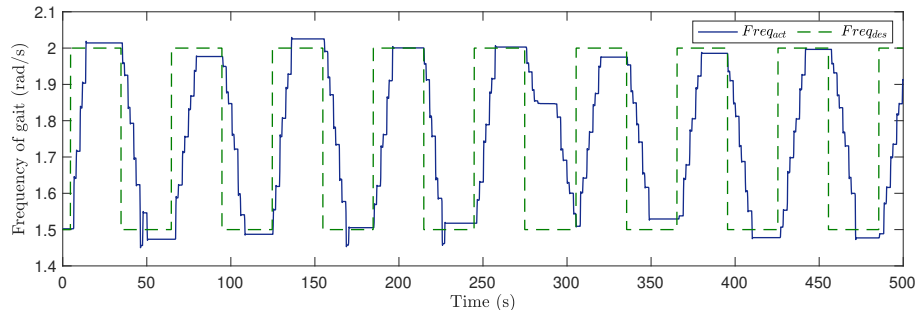
Table 6.1: Parameters of the proposed iCPGs and RL.

### 6.4.1 Simulation results

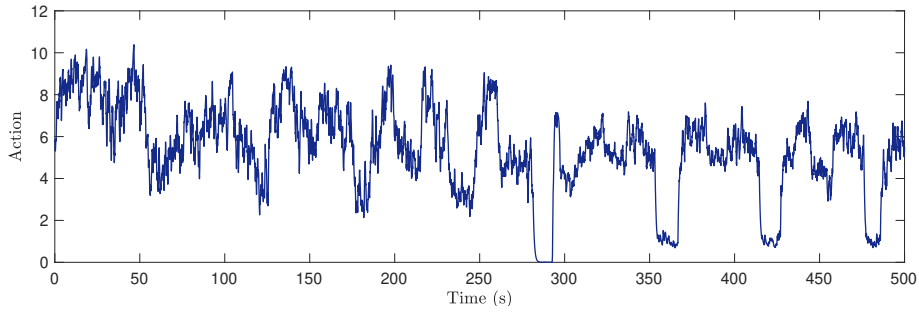
The iCPG and RL parameters employed in the simulation and experiment are summarized in Table 6.1. Also, the coefficients of the Fourier series in (6.4) were calculated based on the gait data of a neurologically intact person [18].

#### Weak muscle scenario

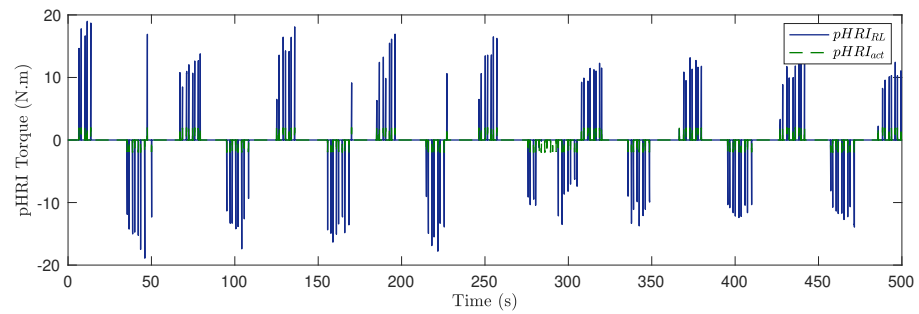
Figure 6.2 shows the results for training RL agent for 500 s in the weak muscle scenario. Note that  $\eta$  in (6.2) was set to 0.003 to represent weak muscle behavior in the simulation. For almost 300 s, the RL agent was exploring, and the introduced actions (Fig. 6.2b) did not follow a specific pattern. The RL agent found the optimal policy after 300 s as shown in Fig. 6.2b, suggesting a higher gain ( $K_{RL}$  in (6.5)) during physical interaction and a lower gain when there is no pHRI. The reason for this behavior is the existence of the  $\text{gain}_{\text{pen}}$  in the reward function, which encourages the RL agent to use the minimum possible RL gain. This helps the system avoid drastic changes in the gait pattern and provide higher comfort and safety. The commanded actions by the RL agent (Fig. 6.2b) modified the pHRI torque (Fig. 6.2c) and increased that to facilitate reaching the desired frequency. The modified pHRI torque was used to calculate the modified interaction energy via Eq. (6.3) and update the gait frequency via iCPGs as seen in Fig. 6.2a.



(a)



(b)



(c)

Figure 6.2: (a) Frequency, (b) RL action, (c) pHRI torque, and (d) modified interaction energy, for weak muscle scenario during the training process in the simulation.

### Strong muscle scenario

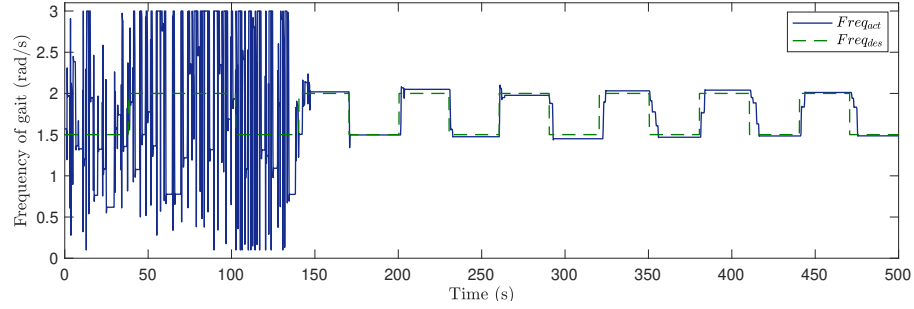
To represent the strong muscle scenario,  $\eta$  in (6.2) was set to 0.05. The outcomes of training the strong muscle scenario in the proposed simulation environment are illustrated in Fig. 6.3. During the initial 200 s, the agent explored the action space, testing various gain values. After this period, it settled into a more optimal pattern for modifying pHRI, as shown in Fig. 6.3b. The recommended modifications via RL were then applied to pHRI, resulting in decreased user physical interactions (see Fig. 6.3c) and facilitating attainment of the desired frequency shown in Fig. 6.3a.

### 6.4.2 Empirical results

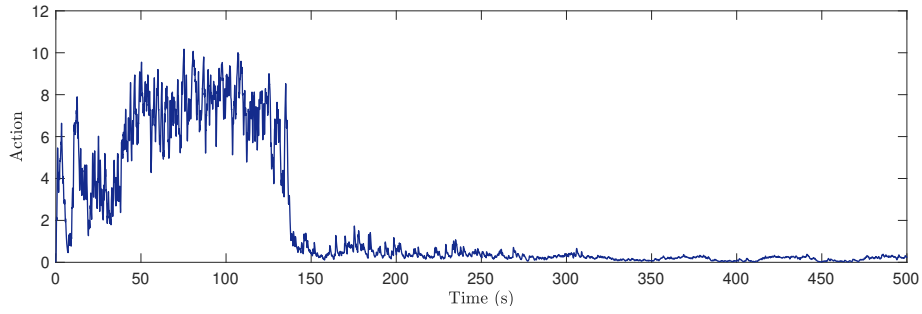
To evaluate the proposed intelligent personalized motion planning algorithm, three neurologically intact users were involved in the experiments. The users wore the Indego lower-limb exoskeleton (Parker Hannifin Corporation, Macedonia, OH) and also used a custom-made walker for safety while walking. The experimental setup is shown in Fig. 6.4. To run the iCPG code, a desktop real-time Simulink was used with a sampling frequency of 1 kHz. For running the reinforcement learning algorithm, a Python script was used with a sampling frequency of 100 Hz. To create both weak and strong muscle scenarios, the  $\eta$  in (6.2) was set to be 0.003 and 0.05, respectively, for all three users during the experiments.

#### First user

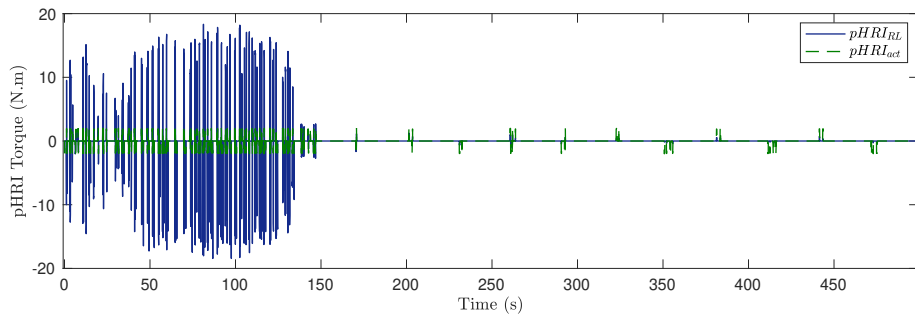
Four different experiments were conducted with this user in order to evaluate the performance of the proposed iCPGs and RL in motion planning. The user's pHRI torque was within the range of 1.8 – 2.1 N.m. For the weak muscle scenario, the average action suggested by the RL agent ( $K_{RL}$  in (6.5)) was 4.12 for the time period shown in Fig. 6.5a. This meant that the user's applied pHRI was amplified by the factor of 4.12. This amplification facilitated the transition between desired frequencies of 1.5 and 2.2 rad/s. As shown in Fig. 6.5a, the transition between two desired



(a)



(b)



(c)

Figure 6.3: (a) Frequency, (b) RL action, (c) pHRI torque, and (d) modified interaction energy, for strong muscle scenario during the training process in the simulation.

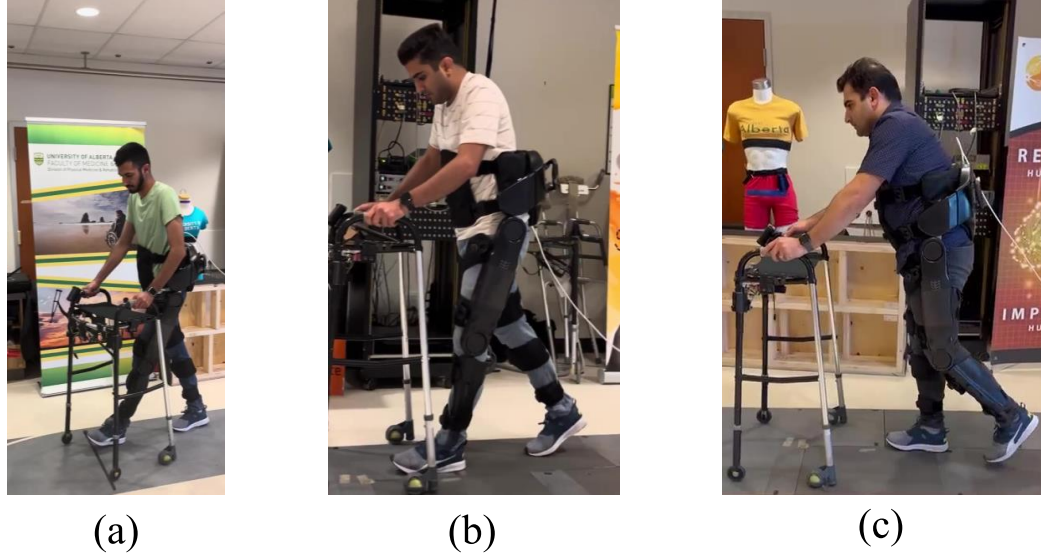


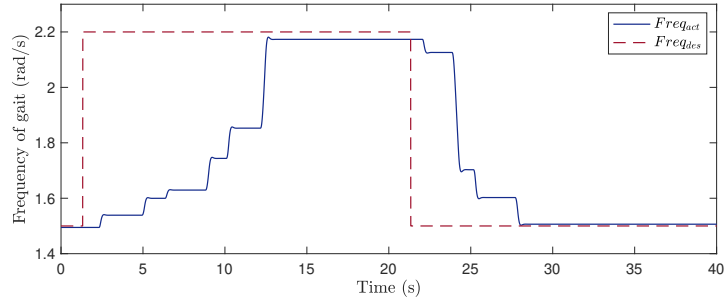
Figure 6.4: Experimental set-up used for empirical experiments with a) first, b) second, and c) third users.

frequencies took a maximum of 13 s in the presence of RL modification. The same transition took more than 30 s in the absence of the RL agent.

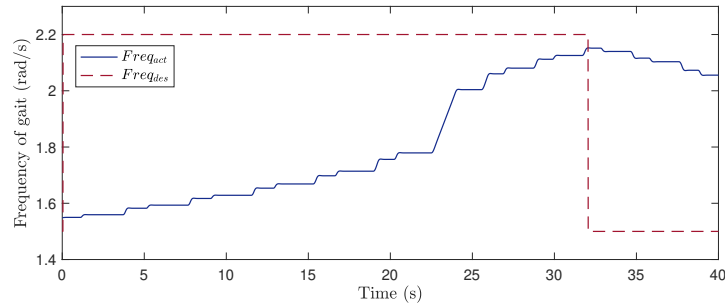
For the strong muscle scenario, the user’s applied interaction was decreased to almost half of its actual value via RL modifications. As shown in Fig. 6.5b, the user oscillated around the desired frequency and did not converge to that in the allocated 40 s. However, by adding the RL modification, the user could reach the desired value in a maximum of 4 s (see Fig. 6.6a).

### Second user

Similar to the first user, the second user performed four different experiments, including weak and strong muscle scenarios in the presence and absence of the proposed RL-based modifications. The pHRI torque applied by the user was within the range 1.6 – 1.9 N.m, and the desired frequencies were 1.3 and 2.1 rad/s. For the weak muscle scenario, the average modification suggested by the RL agent was 3.81 around the 40 s mark shown in Fig. 6.7a. In the absence of the RL modification, the user could not reach the desired frequency in the 40 s allocated time as shown in Fig. 6.7b. However, taking into account the RL modification in pHRI, the maximum elapsed

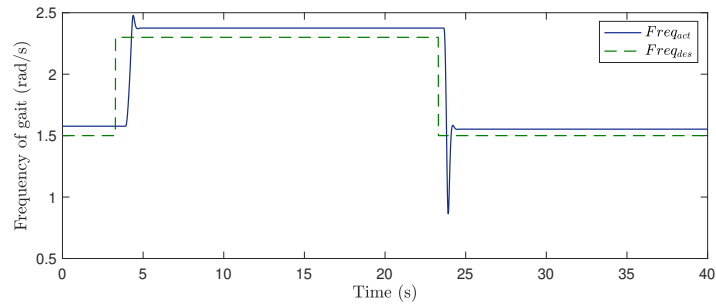


(a)

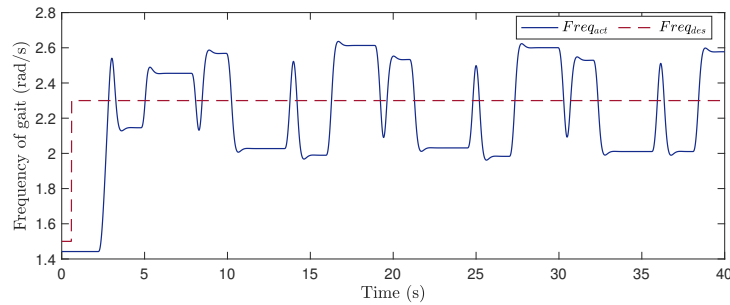


(b)

Figure 6.5: Actual and desired frequency of the first participant in the a) presence and b) absence of RL modification to the pMRI torque for weak muscle scenario.

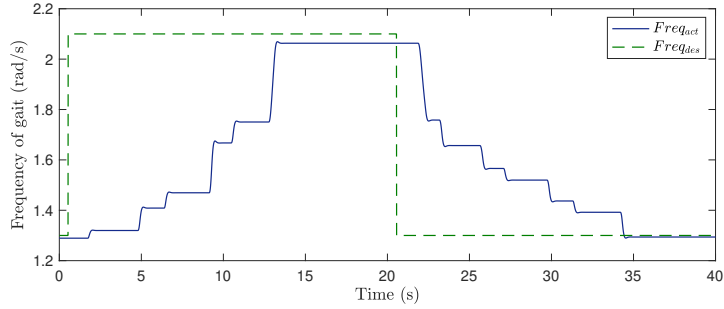


(a)

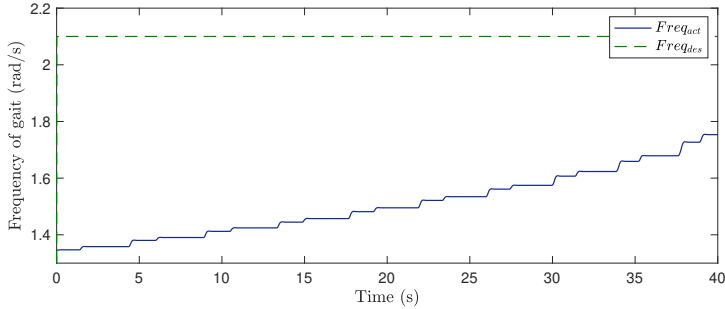


(b)

Figure 6.6: Actual and desired frequency of the first participant in the a) presence and b) absence of RL modification to the pMRI torque for weak muscle scenario.



(a)



(b)

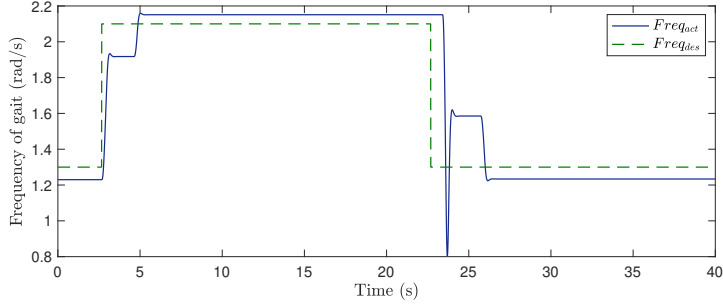
Figure 6.7: Actual and desired frequency of the second participant in the a) presence and b) absence of RL modification to the pHRI torque for weak muscle scenario.

time in reaching the desired frequency is 14 s as shown in 6.7a.

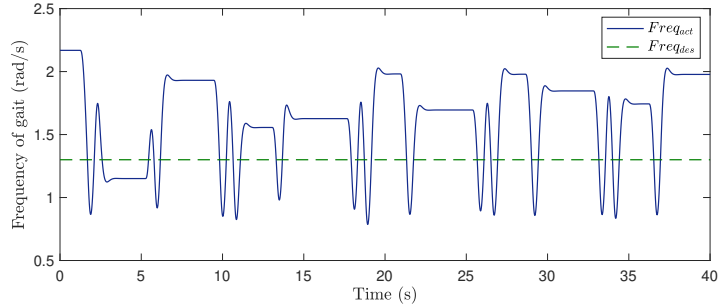
For the strong muscle scenario, the RL decreased the actual pHRI torque by a factor of 0.35 on average. Due to these modifications, the user reached their desired value in less than 4 s as shown in Fig. 6.8a. However, in the absence of the RL modifications, the user oscillated around the desired value for 40 s and has never reached the desired value.

### Third user

The aforementioned four scenarios were also tested with the third user. While the other two users displayed symmetric interaction behavior in both positive and negative directions, this user exhibited positive pHRI torque within the range of 1–1.5 N.m and negative pHRI torque within the range of 2 – 2.2 N.m. In the weak muscle scenario, the user’s physical interactions never reached the desired frequency of 1.35 rad/s, as illustrated in Fig. 6.9b. However, the user was able to transition



(a)



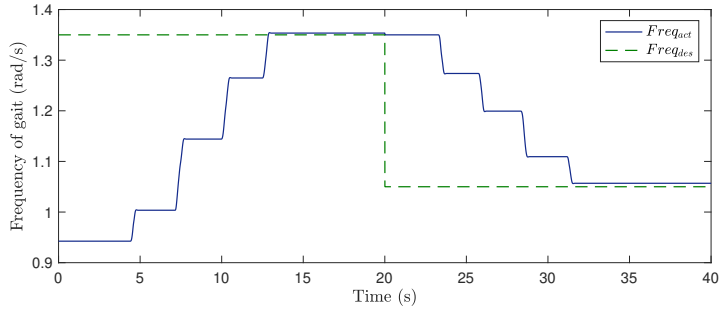
(b)

Figure 6.8: Actual and desired frequency of the second participant in the a) presence and b) absence of RL modification to the pHRI torque for weak muscle scenario.

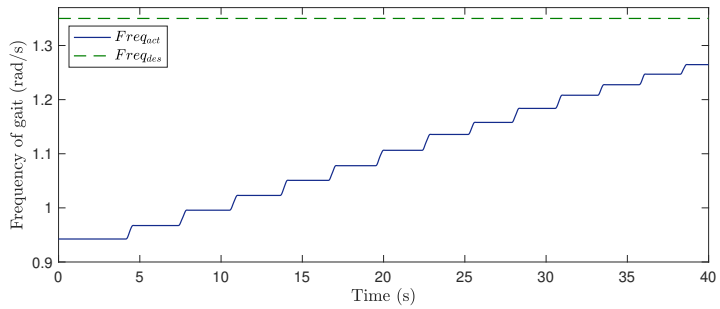
between two desired values of 1.35 rad/s and 1.05 rad/s in under 15 s through amplification from the RL agent, with an average amplification factor of about 3.9, as shown in Fig. 6.9a. It is important to note that smaller desired frequencies were selected for this user in order to evaluate the performance of the proposed method across various scenarios.

Within the context of the strong muscle scenario, the user’s applied pHRI torque was, on average, reduced by a factor of 0.3. This modification significantly improved the user’s ability to attain the desired frequencies, achieving them in under 10 s as depicted in Fig. 6.10a. In contrast, without the RL modification, the user was unable to make the same transition to the desired frequency, even though they physically interacted with the exoskeleton, as evident in Fig. 6.10b.

Upon reviewing the outcomes for all users, we found that, despite minor variations in the physical interaction behavior of individuals, our trained RL agent effectively

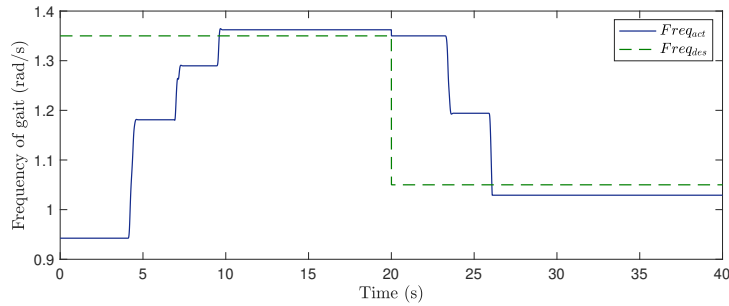


(a)

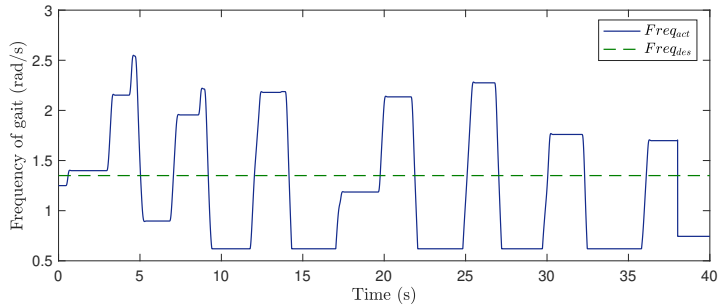


(b)

Figure 6.9: Actual and desired frequency of the third participant in the a) presence and b) absence of RL modification to the pMRI torque for weak muscle scenario.



(a)



(b)

Figure 6.10: Actual and desired frequency of the third participant in the a) presence and b) absence of RL modification to the pMRI torque for weak muscle scenario.

facilitated the transition between different desired frequencies.

## 6.5 Conclusion

In this study, we introduced a novel approach that integrated RL with iCPGs to develop personalized motion planning strategies for exoskeleton-assisted mobility. By leveraging an ACPG algorithm, we addressed the challenge of precise parameter identification, significantly bolstering the method’s robustness. Furthermore, we refined the RL reward function and concept of interaction energy, placing user safety and responsiveness at the forefront of exoskeleton system design. The introduction of a dedicated simulation environment for agent training, faithfully replicating user-exoskeleton interactions, has marked a critical milestone in our research. In addition to our own work, this environment can be used by other researchers for training any RL-based or neural network-based algorithms. Extensive simulations and trials involving neurologically intact participants have yielded remarkably promising results, underscoring the potential of our approach.

# Chapter 7

## Intelligent Locomotion Planning with Enhanced Postural Stability for Lower-Limb Exoskeletons

### 7.1 Introduction

Spinal cord injuries, stroke, and multiple sclerosis are some causes of neurological impairments in the human gait. Millions of people affected by these conditions will be able to handle their daily activities and enhance their physical abilities by taking advantage of assistive and rehabilitative wearable systems (e.g., exoskeleton) developed in recent years [101]. The capabilities of exoskeletons in providing long-term repetitive movements, facilitating physical assistance and collecting users' motion data by their embedded sensory systems make them unique for lower-limb rehabilitation purposes [102]. Despite all of the advantages of employing exoskeletons in medical applications, providing adaptable trajectories and gait features that can be amended by the wearer while preserving the postural stability autonomously still needs to be addressed to provide compliant and safe human-robot interaction (HRI) [14].

In the present chapter, an intelligent control strategy was developed and tested for lower-limb exoskeletons by introducing a new integration of DCM and ACPG schemes to facilitate both postural stability and adaptive locomotion planning. The DCM analysis, which was previously developed for bipedal locomotion of humanoid

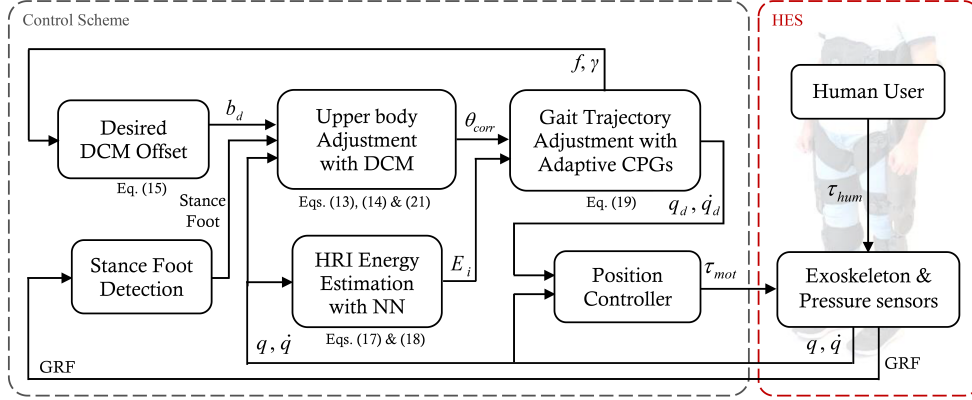


Figure 7.1: Structure of the proposed intelligent control strategy with combination of DCM and ACPG schemes for upper body adjustment and trajectory shaping

robots, was extended and generalized for the human-exoskeleton system (HES) for the first time. To this end, the LIPF model was replaced with a new 4-DOF body (4DB) model to address the following issues: (a) In the LIPF model, the CoM of the whole system is considered to be at the middle of the line that connects the right and left hips. However, for the humans, the CoM is mostly higher than this level and can be different for users based on their body characteristics. Taking 4DB model into account, the CoM of combination HES can be at any point higher or lower than this level. (b) Due to the attachment of exoskeleton to the human body, the mechanical properties (e.g., moment of inertia and mass) for different segments of the HES can be significantly different for various wearers. Using the proposed 4DB model, these dynamic parameters can be personalized for each user to make the locomotion control strategy case-specific.

Using the proposed DCM analysis, a hip joint correction was generated in real-time to amend the trunk position and consequently adjust the DCM on its desired value at the end of each step. ACPGs were defined to shape joint trajectories in response to the human interaction torques by regulating the amplitude and frequency of walking. In addition, the ACPG dynamics was designed to guarantee that gait frequency is less than the maximum stable frequency of walking and the output trajectories are within the feasible movement ranges of the exoskeleton joints. Accordingly, the set of com-

mands generated by the DCM and ACPG schemes were combined to autonomously facilitate locomotion trajectories that are compatible with the user’s intention (active physical interaction) and also ensure the viability of walking through postural stability. The NARX neural network was employed to learn the passive dynamics of the HES in offline training sessions similar to method introduced in Chapter 4. Various position and velocity trajectories (inputs), and associated joint torques (outputs) of the multi-DOF exoskeleton were fed to this NN for training. The network was then used to estimate the active portion of the human physical interaction torque online and obtain pHRI energy for the ACPG-based trajectory shaping. The rest of the chapter is organized as follows. The DCM and ACPG formulations for upper-body and gait adjustments are described in Section 7.2. The experimental results of the proposed strategy having an able-bodied wearer are demonstrated and discussed in Section 7.3, and concluding remarks are mentioned in Section 7.4.

## 7.2 Methodology

In this section, the mathematical formulations and different components of the proposed intelligent control strategy with their interconnections are explained. Using this strategy, the exoskeleton’s wearer has the authority to adjust and personalize the gait parameters by applying torques and ACPGs that translate this pHRI torque into compliant locomotion trajectories. In order to guarantee the viability of walking, the exoskeleton modifies the upper body position using a hip correction approach based on a new DCM analysis. The structure of this control strategy with the combination of DCM and ACPG schemes is shown in Fig. 7.1.

### 7.2.1 DCM Analysis with 4DB Model

The linear inverted pendulum flywheel model has been widely used to simulate and analyze bipedal walking for humanoid robots. In this model, the center of mass is considered to be exactly in the middle of the imaginary line that connects the right

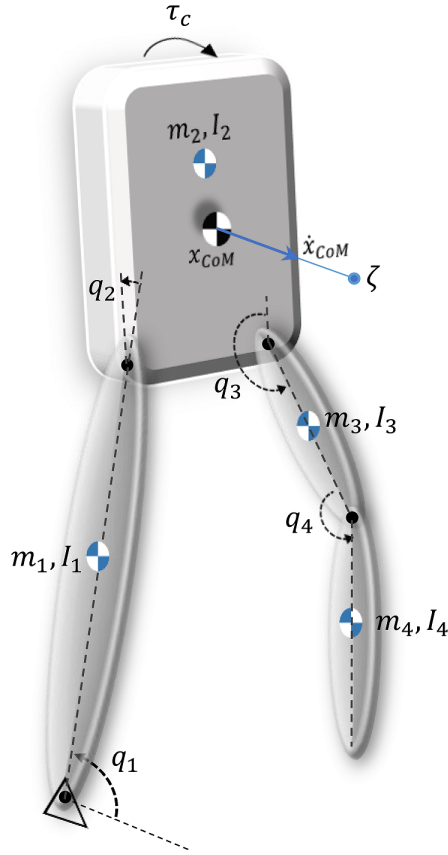


Figure 7.2: Schematic of the proposed 4-DOF body (4DB) model for DCM analysis and left hip joints. Also, the mass-less inverted pendulum and flywheel represent the legs and upper body, respectively, which are simplistic assumptions. To study a collaborative human-exoskeleton walking, due to the human body characteristics, the center of mass can be at any point (not necessarily the hip joint). In order to address this issue, a new 4-DOF body (4DB) model was developed to represent the bipedal locomotion of the HES. As demonstrated in Fig. 7.2, the first link represents the stance leg, which is pivoted on the ground at the foot's center of pressure (CoP). The second segment in this model is the upper body, and the third and fourth links are devoted to the thigh and shank of the swing leg. The center of mass (CoM) of the HES is person-specific, which can be obtained based on the mechanical specifications of the user and exoskeleton. Using the Euler-Lagrange equation, the motion dynamics of the 4DB model was derived as

$$\begin{aligned}
& \overbrace{\begin{bmatrix} M_{11} & M_{12} & M_{13} & M_{14} \\ M_{12} & M_{22} & M_{23} & M_{24} \\ M_{13} & M_{23} & M_{33} & M_{34} \\ M_{14} & M_{24} & M_{34} & M_{44} \end{bmatrix}}^M \overbrace{\begin{bmatrix} \ddot{q}_1 \\ \ddot{q}_2 \\ \ddot{q}_3 \\ \ddot{q}_4 \end{bmatrix}}^{\ddot{q}} + \\
& \overbrace{\begin{bmatrix} G_{11} & G_{12} & G_{13} & G_{14} \\ 0 & G_{22} & G_{23} & G_{24} \\ 0 & 0 & G_{33} & G_{34} \\ 0 & 0 & 0 & G_{44} \end{bmatrix}}^G \overbrace{\begin{bmatrix} \cos(q_1) \\ \cos(q_1 + q_2) \\ \cos(q_1 + q_2 + q_3) \\ \cos(q_1 + q_2 + q_3 + q_4) \end{bmatrix}}^p = \overbrace{\begin{bmatrix} 0 \\ \tau_c \\ 0 \\ 0 \end{bmatrix}}^\tau
\end{aligned} \tag{7.1}$$

where the elements of the inertia ( $M$ ) and gravity ( $G$ ) matrices are defined in the Appendix A. Note that in the derivation of the 4DB model, the segments were considered to be close to their vertical positions ( $q_1 \simeq \frac{\pi}{2}$ ,  $q_2, q_3, q_4 \simeq 0$ ) in the upright configuration of the body. Similar assumptions were considered in the previous models, e.g., LIP and LIPF [57], [56]. Given the 4DB model, the position and acceleration of the Center of Mass (CoM) are

$$x_{CoM} = \overbrace{\begin{bmatrix} \varphi_1 & \varphi_2 & \varphi_3 & \varphi_4 \end{bmatrix}}^\varphi \begin{bmatrix} p \end{bmatrix} \tag{7.2}$$

$$\ddot{x}_{CoM} = \overbrace{\begin{bmatrix} -\varphi_1 - \varphi_2 - \varphi_3 - \varphi_4 \\ -\varphi_1 - \varphi_2 - \varphi_3 \\ -\varphi_1 - \varphi_2 \\ -\varphi_1 \end{bmatrix}}^\psi \begin{bmatrix} \ddot{q}_1 \\ \ddot{q}_2 \\ \ddot{q}_3 \\ \ddot{q}_4 \end{bmatrix} \tag{7.3}$$

in which  $\varphi_i$  for  $i = 1 - 4$  are defined as

$$\begin{aligned}
\varphi_1 &= \frac{m_1 l_{c1} + m_2 l_1 + m_3 l_1 + m_4 l_1}{\sum_{i=1}^4 m_i} & \varphi_2 &= \frac{m_2 l_{c2}}{\sum_{i=1}^4 m_i} \\
\varphi_3 &= \frac{m_3 l_{c3} + m_4 l_3}{\sum_{i=1}^4 m_i} & \varphi_4 &= \frac{m_4 l_{c4}}{\sum_{i=1}^4 m_i}
\end{aligned} \tag{7.4}$$

Given (7.1), the joint acceleration vector can be summarized as

$$\ddot{q} = M^{-1}[\tau - Gp] \tag{7.5}$$

Note that the inertia matrix  $M$  is positive definite and always invertible. Therefore, substituting (7.5) into (7.3), the acceleration of CoM is obtained as

$$\ddot{x}_{CoM} = \psi M^{-1} \tau - \psi M^{-1} G p \quad (7.6)$$

Having (7.2), the acceleration of CoM can be rewritten as a function of the CoM position ( $x_{CoM}$ ) and the torque applied to the trunk ( $\tau$ ) as

$$\ddot{x}_{CoM} = \alpha x_{CoM} + \beta \tau \quad (7.7)$$

where  $\alpha$  and  $\beta$  are

$$\alpha = -\psi H x_{CoM} \quad \beta = \psi M^{-1} \quad (7.8)$$

and  $H = M^{-1} G \varphi^\dagger$ , in which  $\varphi^\dagger$  is the right pseudo-inverse of  $\varphi$ , defined as  $\varphi^\dagger = \varphi^T (\varphi \varphi^T)^{-1}$ .

Similar to the definition proposed in Jeong et al. [56], the extended DCM for the new 4DB model is defined as (see Appendix A for detailed description)

$$\zeta = x + \frac{\dot{x}}{\sqrt{\alpha}} \quad (7.9)$$

Substituting the CoM acceleration in the 4DB model (7.7) into the time derivative of (7.9), the extended DCM dynamics is obtained as

$$\dot{\zeta} = \sqrt{\alpha} \left( \zeta + \frac{\beta}{\alpha} \tau \right) \quad (7.10)$$

In order to facilitate stable locomotion, the DCM value ( $\zeta$ ) at the end of each gait cycle needs to be controlled [103]. To this end, an optimization problem was defined to minimize the error between the actual and desired values of the DCM at the end of each step by adjusting the correction torque applied to the upper body.

$$\min_{\tau_c} w_1 \|\tau_c\|_2^2 + w_2 \|\zeta_T - \zeta_{T_d}\|_2^2 \quad (7.11)$$

where  $\zeta_T$  and  $\zeta_{T_d}$  are the actual and desired end-of-step values of the DCM, respectively, and  $w_1$  and  $w_2$  are the optimization gains. Due to the attachment of the

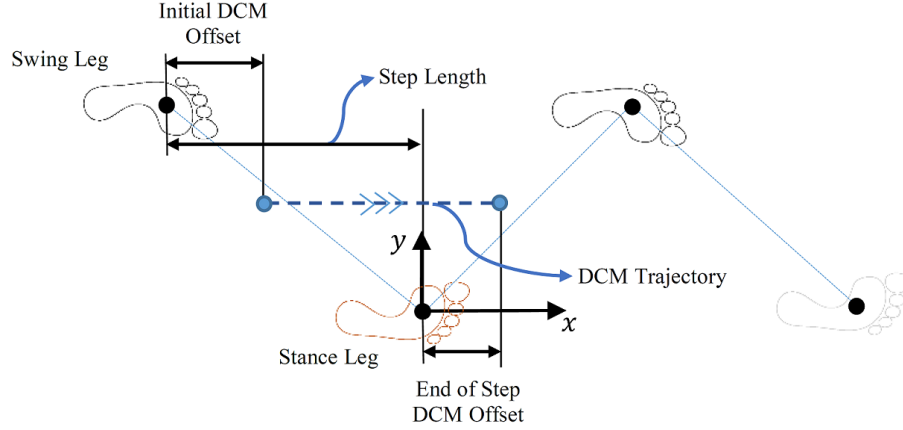


Figure 7.3: Demonstration of footprints and DCM trajectory and offset during locomotion

relative reference frame to the stance foot (shown Fig. 7.3), the desired DCM value at the end of the step ( $\zeta_{T_d}$ ) is equal to the desired DCM offset at that moment ( $b_d$ ), which is defined in the next section.

## 7.2.2 DCM Offset for Viability of Walking

The DCM offset was defined as the difference between the landing location of the foot at the end of its swing phase and the point that DCM arrives at the end of that step. This offset is known as the key factor to address the most important characteristic of the bipedal locomotion, which is postural stability ensuring the viability of walking [104]. For instance, the higher gait velocities require larger DCM offset values and vice versa [56]. Figure 7.3 depicts the schematic of footprints and DCM offset in one stride.

The desired DCM offset for the 4DB model was determined based on the amplitude and frequency characteristics of the walking as described by Jeong et al. [56], and Khadiv et al. [105]

$$b_d = \frac{L}{e^{\sqrt{\alpha}T} - 1} \quad (7.12)$$

where  $L$  is the stride length and  $T$  is the step time. By reaching the desired offset value at the end of the step, in the absence of any disturbance, the CoM will travel

the desired distance during the next step [104]. Using the ACPG dynamics in the proposed strategy, the user can modify the amplitude and frequency of locomotion based on his/her desired gait pattern, by applying pHRI torque. Therefore, the desired DCM offset will be affected by any change in the amplitude and frequency of walking. Accordingly, the physical HRI can alter the desired DCM value/offset at the end of each step.

Considering the kinematic and dynamic constraints of the human-exoskeleton system, the maximum possible DCM offset is calculated as

$$b_{max} = \frac{L_{max}}{e^{\sqrt{\alpha}T_{min}} - 1} \quad (7.13)$$

where  $L_{max}$  is the maximum feasible stride length and  $T_{min}$  is the minimum step time.

### 7.2.3 ACPG Dynamics for Synchronized and Feasible Locomotion

ACPG dynamics was used for shaping stable gait parameters based on the pHRI torque. In order to prevent the loss of postural stability during locomotion, threshold terms were added to the ACPG dynamics to confine the amplitude and frequency of walking to the kinematic limits of the human-exoskeleton system. Therefore, the user has the authority to adjust the gait parameters over the stable limit by applying the interaction torque. In order to determine the pHRI torque, an autoregressive network with exogenous inputs (NARX) was used to learn the passive dynamics of human limbs and exoskeleton. To collect motion and motor actuation data, a neurologically intact user was asked to walk with an exoskeleton over the ground for several trials. The data were classified for the stance phases of the right and left legs based on heel strike moments from pressure sensors embedded in insoles. Also, the user was asked to not apply any active interaction torque, so that the whole system was actuated using the motor torque applied to the joints. The position, velocity and torque values of the joints were collected for different frequency and amplitude values to be used for training the NARX. For the training process, the

position and velocity of the joints were considered as the inputs  $u(t)$ , and the motor torques of the joints as the output  $y(t)$ . The trained NARX had the capability of estimating the passive dynamics of the human limbs and exoskeleton ( $\tau_{pass}$ ) during the online experimental process. Therefore, the interaction torque was determined as the difference between the current joint torque of the joint ( $\tau_i$ ) and the passive joint torque that was estimated by the NARX ( $\tau_{pass}$ ) as [37]

$$\tau_{HRI_i} = \tau_i - \tau_{pass} \quad (7.14)$$

Given the pHRI torque, the pHRI energy for each joint  $i$  was determined by taking the time integral of the multiplication of pHRI torque and velocity as

$$E_i(t) = \int_0^t \tau_{HRI_i}(t) \dot{q}_i(t) dt \quad (7.15)$$

in which  $\dot{q}_i(t)$  is the velocity and  $\tau_{HRI_i}(t)$  is the estimated human torque of the joint  $i = 1, \dots, n$ . When the interaction torque had the same sign as velocity, the applied torque accelerated and when they had opposite signs, this torque caused deceleration of walking. The ACPG dynamics for the joint trajectory generation, considering maximum gait frequency and amplitude, was defined as

$$\begin{aligned} \dot{\theta}_i(t) &= f(t) + \sum_{j=1}^{m_i} v_{ij} \sin(\theta_i(t) - \theta_j(t) - \phi_{ij}) \\ \ddot{f}(t) &= \mu_f \left( \frac{\mu_f}{4} (F + \sum_{k=1}^n \eta_k E_k - f(t)) - \dot{f}(t) \right) - k_f \frac{DZ^+(f(t) - f_{th})}{(f_{max} - f(t))^3} \\ \ddot{\gamma}(t) &= \mu_\gamma \left( \frac{\mu_\gamma}{4} (A + \sum_{k=1}^n \lambda_k E_k - \gamma(t)) - \dot{\gamma}(t) \right) - k_\gamma \frac{DZ^+(\gamma(t) - \gamma_{th})}{(\gamma_{max} - \gamma(t))^3} \end{aligned} \quad (7.16)$$

where  $m_i$  is the number of adjacent joints to the joint  $i$ , and  $n$  is the number of all joints.  $f_{max}$  and  $\gamma_{max}$  are the maximum frequency and amplitude values considered based on the motion constraints of the exoskeleton and walking safety concerns. If the frequency and amplitude exceed their threshold values  $f_{th}$  and  $\gamma_{th}$ , the dead-zone function  $DZ^+$  is triggered to control them below their maximum values. Note that  $DZ^+(x) = x$  for positive values of  $x$  and  $DZ^+(x) = 0$  for any non-positive  $x$ . The  $\eta_k$

and  $\lambda_k$  are constant gains for the effect of pHRI energy on the locomotion frequency and amplitude, respectively.  $v_{ij}$ ,  $\mu_f$  and  $\mu_\gamma$  are other constant parameters of the dynamics. Using (7.16), the knee joint  $i$ 's desired trajectory was formulated as

$$q_{d_i}(t) = \gamma(t)(a_{i_0} + \sum_{l=1}^{N_i}(a_{i_l} \cos(l\theta_i(t)) + b_{i_l} \sin(l\theta_i(t)))) \quad (7.17)$$

where  $a_{i_l}$  and  $b_{i_l}$  are the coefficients of the Fourier series (with  $N_i$  terms) to initially coordinate the desired knee trajectory of the joint  $i$  with a typical one, as presented in Fig. 7.1.

The correction trajectory for the hip joints is affected by the obtained torque from the DCM adjustment strategy (see Eq. (7.11)).

$$\tau_c = J\ddot{\theta}_{corr} \quad (7.18)$$

where  $J$  is the moment of inertia for the upper-body of HES. By integrating the DCM torque in (7.18) over time, the trajectory correction for the hip joints ( $\theta_{corr}$ ) was determined. This time-varying correction adjusts the upper body position to reach the desired DCM value at the end of each step. Therefore, the desired trajectories of the stance and swing legs' hip joints were defined in terms of variables in (7.16) and (7.18) as

$$\begin{aligned} q_{d_{h_{ST}}}(t) &= \gamma(t)(a_{i_0} + \sum_{l=1}^{N_i}(a_{i_l} \cos(l\theta_i(t)) + b_{i_l} \sin(l\theta_i(t)))) + \theta_{corr} \\ q_{d_{h_{SW}}}(t) &= \gamma(t)(a_{i_0} + \sum_{l=1}^{N_i}(a_{i_l} \cos(l\theta_i(t)) + b_{i_l} \sin(l\theta_i(t)))) - \theta_{corr} \end{aligned} \quad (7.19)$$

where  $q_{d_{h_{ST}}}$  and  $q_{d_{h_{SW}}}$  are the desired trajectories of stance and swing legs' hip joints, respectively.

Given all of the desired joint trajectories, which are generated in real-time from the combination of DCM and ACPG schemes, a position tracking controller can be employed to follow this comfortable and safe locomotion. Note that because of the ACPG dynamics, the wearer has enough authority to adjust the gait parameters,

but the intelligent controller of the exoskeleton limits the amplitude and frequency to ensure the viability of walking. Figure 7.1 demonstrates the structure of the proposed autonomous trajectory shaping and postural stability control.

### 7.3 Results & Discussion

In order to evaluate the effectiveness of the proposed autonomous trajectory shaping strategy, experimental studies were conducted using the Indego lower-limb exoskeleton (Parker Hannifin Corporation) [7] and an able-bodied human subject (height: 173 *cm*; weight: 67 *kg*) shown in Fig. 7.4. Note that the body characteristics of the exoskeleton wearer in (7.1) were estimated based on the provided formulations in Winter [106] according to the height and weight of the subject. The subject is asked to put a safety harness on, which is connected to an overhead lift to prevent injury in the case of falling. Real-time Desktop Simulink was utilized as the control software to implement the proposed intelligent control strategy (it received the sensory data, processed them and commanded the motor torques) on the exoskeleton with a sampling frequency of 100 Hz. For following the generated online trajectory, the built-in proportional-derivative (PD) position controller of the Indego was employed with appropriately adjusted gains. A pair of insole pressure sensors were embedded inside the shoes for detecting heel strike and stance leg to switch the pivot point of the 4DB model (Fig. 7.2) between the right and left legs. As soon as the switching of the stance phase occurred from one leg to the other, all DCM calculations switch correspondingly such that the pivot point, shifted to the new stance foot.

The experimental results are presented in two parts. In the first part, trunk position adjustment using the proposed DCM analysis was evaluated for postural stability. In the second section, the effect of human interaction torque on the ACPG-based shaping of the gait characteristics (frequency and amplitude) and providing safe locomotion trajectories was investigated. The parameters of the DCM dynamics (7.10) were determined as  $\alpha = 4.95$  and  $\beta = 0.76$  based on the mechanical properties identified



Figure 7.4: Experimental set-up: Indego lower-limb exoskeleton in a user study (having a safety harness) during over-ground walking

for the HES. The optimization gains were also specified as  $w_1 = 10^{-7}$  and  $w_2 = 1$  using a trial-and-error method to have an appropriate trade-off between the obtained torque ( $\tau_c$ ) for the trunk and the DCM error ( $\zeta_T - \zeta_{T_d}$ ) at the end of a step.

### 7.3.1 Trunk Adjustment Using DCM Analysis

The desired DCM offset value at the end of each step was a function of the step length and total frequency of walking based on Eq. (7.12). Due to the variation of landing positions, the optimization approach (Sec. 7.2.1) was utilized to obtain the upper-body torque ( $\tau_c$ ) and determine the hip trajectory correction (Eq. 7.18) in order to minimize the DCM error at the end of each step. The correction value of the upper body position ( $\theta_{corr}$ ) was added to the reference ACPG trajectory for the hip joint of the stance leg. Note that, the negative value of the  $\theta_{corr}$  was added to the reference CPG trajectory of the hip joint of the swing leg, in order to not affect the swing trajectory of the walking.

The primary amplitudes of the hip and knee motions were considered 59 and 70 degrees, and the locomotion frequency was set to  $2.6 \text{ rad/s}$  based on typical gait cycles. Figure 7.5 represents trajectories of the right and left hips with and without

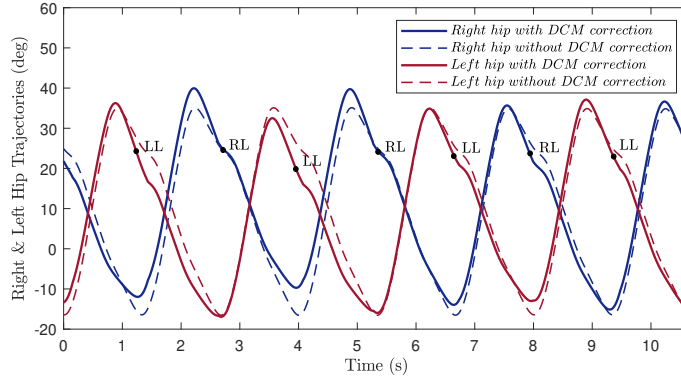


Figure 7.5: Right and left hip trajectories in the presence and absence of DCM corrections

applying the DCM correction for them. This motion correction at the beginning of the stance phase of each leg decreased the desired hip angle of that leg. As seen in Fig. 7.5, the desired trajectory of the swing leg’s hip was also increased in the opposite direction to preserve the landing position of the next step (as described in Sec. 7.2.3). The landing moments of the left and right feet are pointed out in Fig. 7.5, where the acceleration of hip corrections was changed. This behavior is also illustrated in Fig. 7.6, where the modifications can be seen in the relative motion of the hips. From the beginning of the stance phase, the synchronization of the right and left hip joints became distorted as highlighted in Fig. 7.6.

In order to elaborate more on the trunk position correction obtained from the DCM analysis, Fig. 7.7 depicts the DCM values for the stance phases of the right and left legs. Note that in the calculation of DCM magnitude, the stance foot’s CoP was considered as the Cartesian coordinates’ origin (shown in Fig. 7.3). As seen in Fig. 7.7, for the first four steps of walking ( $t = 0 - 5.17$  s), the DCM has a disorganized translation from the initial value to the end-of-step one due to the wearer’s interaction with the exoskeleton. In order to minimize the DCM end-of-step error, the highest position correction for upper body was suggested during this period in comparison to the latest four steps as observed in Fig. 7.5. Similarly, in all of the other steps of walking, the upper body’s position correction adjusted the hip joints’ trajectories

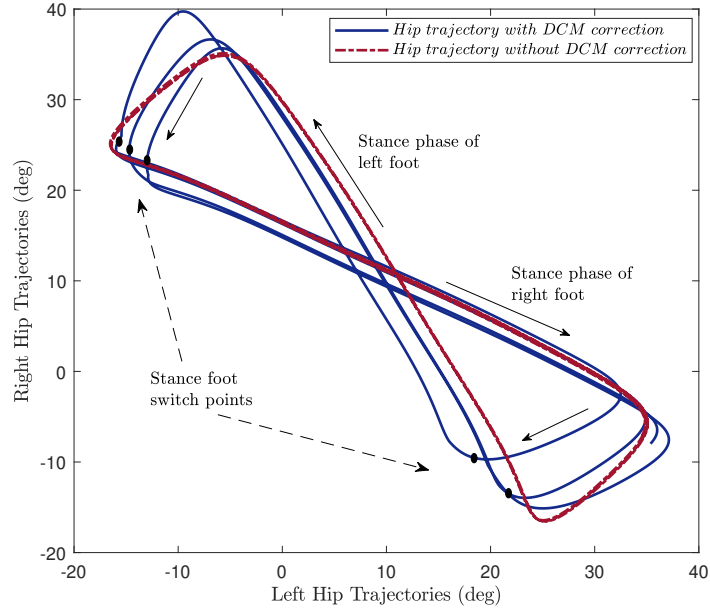


Figure 7.6: Relative motion of the right and left hips with and without considering DCM corrections

generated by ACPGs to reach the desired DCM value at the end of each step. In order to evaluate how the end-of-step DCM error was affected by the upper body adjustment, the result of DCM values in the absence of applying the proposed DCM correction was investigated in another experiment. As demonstrated in Fig. 7.8, the average end-of-step error without upper body adjustment was  $0.05\text{ m}$ , which was considerable and caused unstable walking that would raise the risk of falling down without employing a safety harness. However, using the proposed DCM correction strategy, this error was reduced to  $0.002\text{ m}$  and the DCM trajectory experienced more organized variations (Fig. 7.5).

The desired trajectories for the hip and knee joints, obtained from the combined ACPG and DCM schemes, were commanded to a PD position controller to be tracked by the exoskeleton. The performance of this controller in following the desired values of the right hip and knee (with the maximum errors of  $0.6\text{ degree}$  and  $1.1\text{ degrees}$ , respectively) are shown in Fig. 7.9.

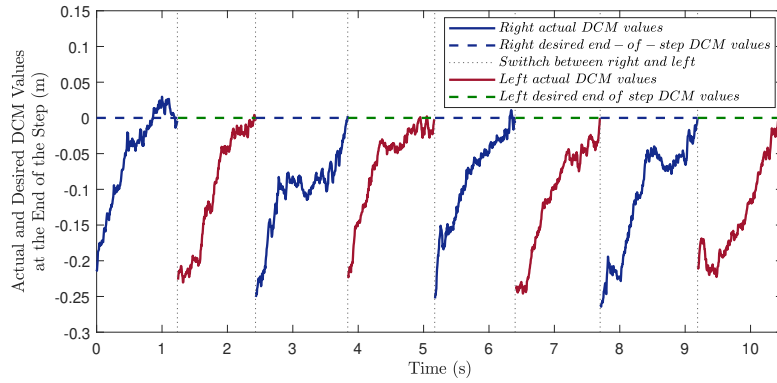


Figure 7.7: Actual and desired end-of-step values of DCM for right and left feet in the presence of DCM correction

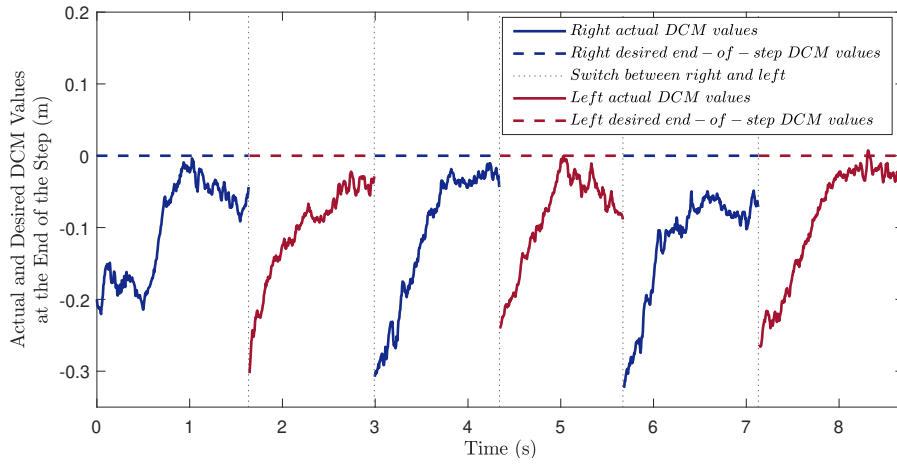


Figure 7.8: End-of-step values of DCM in the absence of DCM correction

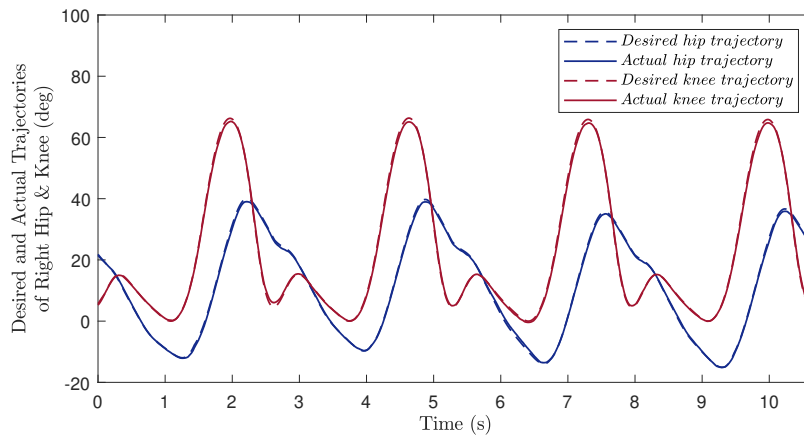
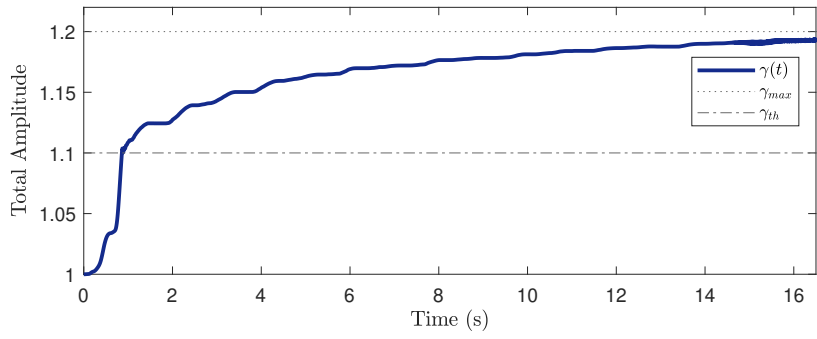


Figure 7.9: Performance of the position controller in tracking the desired right hip and knee trajectories

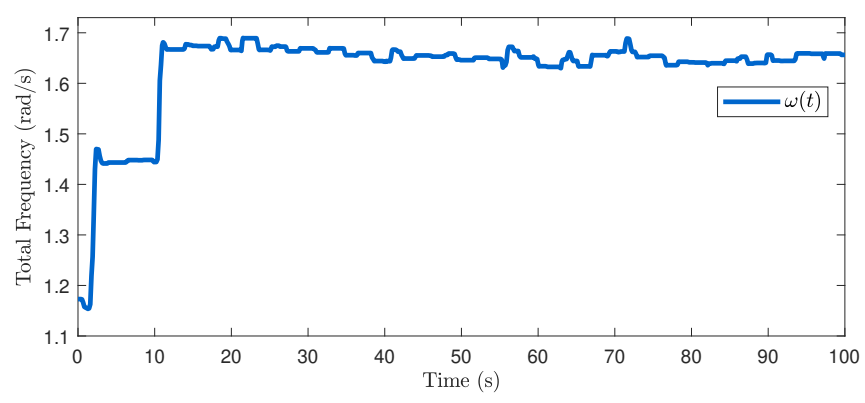
### 7.3.2 Locomotion Shaping with Maximum Walking Frequency

The performance of the proposed ACPGs in online shaping of gait parameters was investigated while preserving the postural stability. During this experiment, the wearer applied accelerating torques on different joints in order to speed up his walking. Although he was able to increase the amplitude and frequency of locomotion, the threshold and maximum values of these variables were set to be  $\gamma_{th} = 1.1$ ,  $\gamma_{max} = 1.2$  and  $f_{th} = 1.04\pi \text{ rad/s}$ ,  $f_{max} = 1.08\pi \text{ rad/s}$  in (7.16) based on practical limitations of the exoskeleton movement and the safety of the human user. As seen in Fig. 7.10a, the total gait amplitude  $\gamma$  increased and reached its threshold value at  $t = 0.85 \text{ s}$ . After this time, the threshold regulation term in (7.16) was activated to detract the increment rate of the amplitude and saturate it around 1.19 at  $t = 14.5 \text{ s}$ . Similar behavior can be seen in Fig. 7.10b for the total frequency of walking according to (7.16), where its threshold regulation term was triggered at  $t = 2.15 \text{ s}$  and then the frequency is saturated below  $f_1(t) = 3.39 \text{ rad/s}$  until 18.5 s. Also, in order to further evaluate the effectiveness of ACPG in facilitating the user's intention, the wearer could change the frequency of walking to a desired value less than the threshold in another experiment. As seen in Fig. 7.10b, the total frequency of walking reached the desired value of  $f_2(t) = 2.4 \text{ rad/s}$  at  $t = 7.5 \text{ s}$  and the user retained this walking frequency for the rest of his locomotion.

As discussed in Sec. 7.2.2, the DCM offset is a function of the walking frequency and the step length. Given the maximum feasible amplitude and frequency of walking as  $\gamma_{max} = 1.2$  and  $f_{max} = 1.08\pi \text{ rad/s}$ , the maximum DCM offset was obtained as  $b_{max} = 7.5 \text{ mm}$ . As is observed in Fig. 7.11, after  $t = 2.17 \text{ s}$  both amplitude and frequency threshold terms were activated in (7.16), the variation rate of  $b_d$  decreased drastically and finally plateaued at  $t = 18.5 \text{ s}$  around 6.6 mm which is less than the maximum offset value ( $b_{max} = 7.5 \text{ mm}$ ).



(a)



(b)

Figure 7.10: Control of (a) the amplitude and (b) the frequency of locomotion between their threshold and maximum values using ACPG dynamics

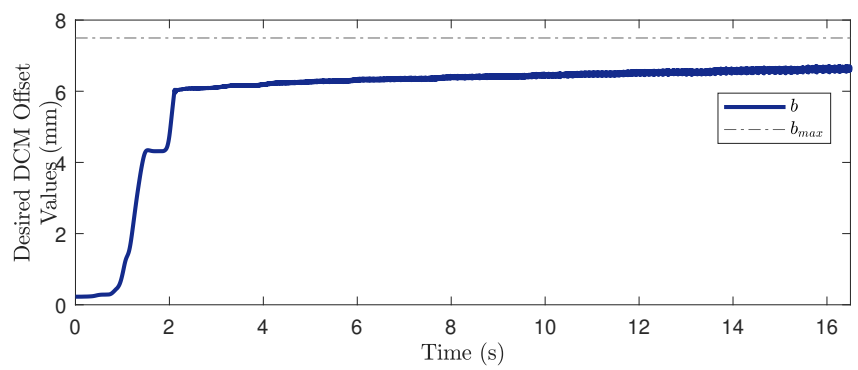


Figure 7.11: Variation of DCM offset below its maximum value

## 7.4 Conclusions

In the present study, a novel intelligent control strategy was developed for the human exoskeleton system, which can revise the locomotion trajectories in real-time for preserving postural stability. In the proposed shared autonomy between the human and robot, the user has the authority of adjusting the amplitude and frequency of walking, while the exoskeleton has enough autonomy to correct the trunk position to guarantee the viability of walking and limit the gait amplitude and frequency within their feasible ranges. For these purposes, the DCM analysis was extended by presenting a new 4-DOF body (4DB) model to be compatible with the human-exoskeleton system's dynamics. Taking the advantage of this 4DB model, the locomotion control was personalized by considering the dynamic parameters of the body segments (moment of inertia, mass and CoM) for each user.

The pHRI torque was employed in the ACPG structure to update the locomotion based on the user's intention. Also, the desired DCM value at the end of each step was calculated based on the user's demanded amplitude and frequency, which is facilitated by adjusting the upper body position using a hip correction strategy for the exoskeleton. To this end, an optimization problem was defined to minimize the DCM end-of-step error by determining the required upper body motion correction that should be added to the desired gait trajectories. This revised trajectory generated by combination of DCM and ACPG schemes was tracked by the exoskeleton's motor controller. The proposed strategy was tested experimentally on the Indego lower-limb exoskeleton, and the obtained results proved its effectiveness in providing postural stability and the adaptation of gait motion. Accordingly, this control method enhanced the user's safety and comfort in walking (as one of the most essential activities) using an assistive exoskeleton by offering a trade-off between the robot autonomy and human authority. The upper-body position adjustment was designed to provide postural stability with slight changes in the gait parameters (amplitude

and frequency) in response to the active pHRI torque. However, for the case of large disturbances, e.g., having a collision with the environment, an extended control approach with the ankle joint's actuation will be required. This strategy can be investigated in future studies using fully actuated exoskeletons.

# Chapter 8

## Conclusions, Recommendations, and Future Work

### 8.1 Conclusions

This dissertation centered on the development of advanced motion planning algorithms with the aim of enhancing adaptability for lower-limb exoskeletons. The research encompassed comparative studies of users' gait patterns, revealing substantial variations in locomotion among individuals. Furthermore, it was evident that an individual's gait could be influenced by factors such as fatigue and aging, causing it to evolve over time. Consequently, an effective exoskeleton should possess the capability to adapt to its wearer's walking pattern, a feature notably absent in the majority of commercially available exoskeletons.

Chapters 1 and 2 were dedicated to presenting the project's underlying motivations and a comprehensive review of prior research efforts that had addressed various challenges. In both Chapter 3 and Chapter 4, the focal point was the introduction of Adaptable Central Pattern Generators (ACPGs) designed to facilitate the generation of walking patterns. These ACPGs operated in synchronization across different joints and were dynamically updated in response to the physical interactions of human users, with the primary aim of enhancing their walking comfort while utilizing exoskeletons.

Within the framework of the proposed ACPGs, an overarching locomotion fre-

quency was established to govern the motion of all joints, modulated in accordance with the energy derived from physical human-robot interactions (pHRI). This system allowed for real-time adjustments to the amplitude and equilibrium positions of joint oscillations based on pHRI torque, all while incorporating safety measures to prevent joint motions from exceeding predetermined safety limits. Furthermore, a Proportional-Derivative (PD) low-level controller was employed to faithfully track the high-level trajectories commanded by the ACPGs.

In the course of evaluating the effectiveness of this intelligent control strategy through experimentation, a group of able-bodied individuals, wearing the Indego exoskeleton, demonstrated the ability to significantly customize and personalize gait characteristics within a brief time frame. This was achieved through the application of active torques to various joints, underscoring the adaptability and real-time responsiveness of the system.

Chapters 5 and 6 described the iCPGs which designed to chart personalized walking trajectories for lower-limb exoskeletons. This novel approach fused RL with the previously established ACPGs, enabling a comprehensive understanding of a user’s physical interaction behavior and the subsequent refinement of the exoskeleton’s walking trajectories. The ACPG method, deeply rooted in the incorporation of pHRI within CPGs, facilitated real-time adaptability of gait trajectories. However, the precise identification and dynamic updating of ACPGs parameters remained a critical prerequisite for the effective refinement of gait trajectories, especially in response to pHRI.

Our proposed method harnessed RL to modulate pHRI energy based on a user’s interaction behavior, culminating in the formulation of an effective energy value that facilitated the realization of desired gait patterns through the dynamics of iCPGs. This innovative approach showed great promise in resolving the previously mentioned challenges associated with ACPGs and personalized trajectory generation. Notably, the outcomes of both simulations and experiments served as tangible evidence of the

method's remarkable capacity to adapt effectively to a user's behavior across various walking scenarios involving the Indego lower-limb exoskeleton.

In Chapter 7, an integrated control strategy was meticulously developed to elevate safety levels by addressing both locomotion trajectory planning and postural stability, thereby fostering shared autonomy between the human operator and the lower-limb exoskeleton. Previously, the regulation of the center of mass (CoM) position for humanoid robots relied on Divergent Component of Motion (DCM) analysis rooted in the Linear Inverted Pendulum Flywheel (LIPF) model. However, within this chapter, a novel extended model was proposed for DCM analysis, supplanting the earlier LIPF model, which was originally tailored for multi-degree-of-freedom (DOF) exoskeletons. This novel model was intricately designed to be personalized for each user, relinquishing the assumption that the total CoM resided solely at the hip joint, as was presumed by the previous LIPF model.

As a result, the exoskeleton gained the authority to ensure postural stability and maintain the viability of locomotion during physical human-robot interaction (pHRI) by orchestrating upper body adjustments through a DCM-based hip correction strategy. Additionally, through the integration of adaptable CPGs, users were empowered to make real-time modifications to gait trajectories while adhering to the boundaries defined by feasible amplitude and frequency ranges for walking. The efficacy of this intelligent controller in promoting both safety and stability during locomotion was investigated and verified through a series of experimental studies conducted with a lower-limb exoskeleton.

Throughout the thesis and as demonstrated in the empirical results, the proposed ACPGs, iCPGs, and DCM algorithms have shown significant potential in enhancing the comfort and safety of motion planning for lower-limb exoskeletons. Both the ACPGs and iCPGs introduce adaptivity to the motion planning process, allowing users to customize the exoskeleton's gait to suit their individual comfort preferences. For instance, users can adjust walking velocity or the range of motion for specific

joints to optimize comfort and accommodate personal preferences. This adaptability empowers users to tailor their exoskeleton's movements according to their unique comfort requirements, ultimately enhancing the overall user experience and improving adherence to exoskeleton-assisted mobility.

The integration of ACPGs, iCPGs, and DCM algorithms has significantly bolstered the safety standards within the exoskeleton system. A key safety enhancement lies in the ensured synchrony among different joints of the exoskeleton during motion planning, facilitated by the ACPGs and iCPGs. This synchronization feature ensures smooth and coordinated movements, thereby promoting safer locomotion. Moreover, the inclusion of safety parameters within the ACPGs structure serves as an additional safeguard by constraining exoskeleton trajectories to safe velocities, step lengths, and ranges of motion. Beyond the ACPGs and iCPGs, the implementation of the DCM algorithm further enhances postural stability, contributing to safer locomotion planning for exoskeleton users. By improving stability and balance, the DCM algorithm helps mitigate the risk of falls or instability during walking, ultimately enhancing the overall safety profile of the exoskeleton system.

Although the proposed algorithms have primarily been tested with able-bodied individuals, they hold significant potential for individuals with neurological impairments, particularly those with spinal cord injuries (SCI). In clinical rehabilitation settings, therapists can leverage these algorithms by adjusting the exoskeleton settings to lower velocities and step lengths, allowing users to actively participate in modifying their walking patterns through applied force. Additionally, considering the diverse nature of impairments and rehabilitation needs among individuals with SCI, adaptive exoskeletons capable of dynamically adjusting gait trajectories offer tailored solutions. This adaptability enables therapists to customize rehabilitation programs to align with individualized goals and varying levels of impairment, fostering personalized gait training programs that effectively address specific challenges and facilitate optimal recovery.

Beyond rehabilitation, adaptive exoskeletons also hold significant potential in the realm of assistance. Currently, many commercially available exoskeletons are designed to be controlled by therapists, limiting independent usage for individuals with spinal cord injuries (SCI). Thus, adaptive exoskeletons emerge as crucial requirements for enabling independent use of these devices in various settings. While the current versions of the proposed algorithms may not be immediately applicable for such applications, the ongoing process of industrializing these algorithms holds promise for their eventual integration into adaptive exoskeletons. Through this process, the potential for individuals with SCI to use exoskeletons autonomously in diverse environments becomes increasingly feasible.

Industrializing the proposed ACPGs, iCPGs, and DCM algorithms for motion planning of exoskeletons for individuals with neurological impairments entails several essential steps. Firstly, conducting comprehensive user studies with able-bodied participants is imperative. This initial step allows for a thorough understanding of the algorithm’s most sensitive aspects, facilitating their refinement to optimize performance. With the improved algorithm and insights garnered from user studies, the next critical phase involves defining the specific neurological impairments that stand to benefit most from the algorithm’s application. Once the target population is clearly identified, rigorous testing of the algorithm on individuals with neurological impairments becomes paramount, accompanied by soliciting their feedback and insights.

This iterative process of user study within the target population offers invaluable insights into the algorithm’s efficacy and suitability for individuals with neurological impairments. By gathering feedback directly from users, including their experiences, challenges, and preferences, a comprehensive understanding of the algorithm’s potential success in addressing the needs of the target population is attained. These insights guide further refinements and adjustments to the algorithm, ensuring its alignment with the specific requirements and preferences of individuals with neurological im-

pairments. Ultimately, this systematic approach to industrialization facilitates the development of robust, user-centered algorithms tailored to enhance motion planning and optimize the functionality of exoskeletons for individuals with neurological impairments.

## 8.2 Limitations of this research

Despite the successful outcomes detailed in the preceding sections, each of the proposed algorithms exhibits certain limitations. For the proposed ACPGs (Chapters 3 and 4), the primary limitation lies in the necessity of applying interaction torque to update the gait. In essence, this method is only applicable to individuals capable of exerting voluntary interaction torques on the exoskeleton joints. Furthermore, the performance of the ACPGs algorithm is heavily reliant on the accuracy of pHRI estimation methods. Inaccuracies in pHRI estimation may lead to deviations from the desired gait pattern. Similarly, involuntary physical interactions with the exoskeleton, stemming from factors such as muscle spasticity, collisions with obstacles, or changes in motion direction, can also influence gait performance. However, despite these limitations, the presence of embedded safety measures within the algorithm ensures that these issues do not result in catastrophic events.

It's worth noting that the proposed ACPGs offer potential benefits in addressing specific scenarios involving involuntary interactions. Take, for instance, the case of muscle spasticity, where involuntary interactions may restrict the range of motion and walking velocity. In such instances, the ACPGs can dynamically adjust the exoskeleton trajectory to avoid positions and velocities that trigger these involuntary physical interactions. By adaptively modifying the gait pattern, the system can mitigate the impact of muscle spasticity, enhancing user comfort and safety during locomotion. Moreover, in the event of a collision with an obstacle in the environment, the ACPGs possess the capability to swiftly respond by either reducing the walking velocity or halting the exoskeleton altogether. This proactive adjustment helps prevent further

collisions and ensures the user’s well-being by promptly addressing potential hazards in the surroundings.

The proposed iCPGs (introduced in Chapters 5 and 6) encounter comparable limitations to those observed with the ACPGs. Challenges persist due to inaccuracies in pHRI torque estimation and the occurrence of involuntary physical interactions, both of which can impede the convergence of the RL agent, leading to suboptimal outcomes. When pHRI torque estimation is inaccurate, the RL agent may base its decisions on flawed information, potentially converging to local optima rather than identifying globally optimal policies. Similarly, involuntary physical interactions, such as those arising from muscle spasticity or collisions with obstacles, introduce uncertainties into the system dynamics, complicating the learning process for the RL agent. These uncertainties may disrupt the exploration-exploitation trade-off, hindering the agent’s ability to discover and exploit effective locomotion strategies.

The primary constraint of the proposed DCM algorithm outlined in Chapter 7 is its limitation to adjusting the upper-body position exclusively. Many algorithms addressing postural stability in bipedal robots typically incorporate adjustments to the upper body, ankles, and foot landing positions to enhance stability. Consequently, our proposed DCM algorithm is particularly effective in scenarios involving minor variations in the gait cycle, such as changes in velocity or step length. However, its applicability becomes restricted when confronted with more significant challenges, such as ensuring postural stability on slippery surfaces. Moreover, the proposed DCM algorithm is specifically designed for walking and may not extend its guarantee of postural stability to diverse modes of motion, such as stair climbing or transitioning from a seated to a standing position.

### **8.3 Future Work**

This thesis has laid the foundation for enhancing the adaptive locomotion planning of exoskeletons for the purpose of walking. While the results presented here showcase

the potential of our approach, there are several promising avenues for future research and development to further advance this field.

A primary and pivotal direction for future research entails the refinement of low-level control strategies to ensure the seamless and natural locomotion of exoskeleton users. While the present study predominantly emphasized high-level control aspects in exoskeletons, there exists significant potential in leveraging advanced low-level control techniques to enhance the flexibility and performance of exoskeletal locomotion. This optimization has the potential to deliver a more comfortable and user-friendly walking experience for exoskeleton wearers, ultimately fostering a heightened level of acceptance and integration of these groundbreaking devices into everyday life.

While this thesis primarily centered its attention on the optimization of walking gaits within the context of exoskeletons, it is imperative to recognize the vast landscape of potential locomotion scenarios that warrant exploration. A promising avenue for future research lies in the development of adaptive control algorithms that encompass a broader spectrum of locomotion types. Specifically, we can embark on investigations into the creation of control strategies for activities like sitting, stair climbing, and even the execution of more intricate locomotion tasks, such as navigating rough terrains and surmounting obstacles while utilizing exoskeleton technology. Furthermore, a crucial aspect deserving attention is the establishment of seamless and efficient transitions between these diverse locomotion modes. Future studies can thus delve into refining these transition mechanisms to further enhance the versatility and adaptability of exoskeleton-assisted mobility.

Functional electrical stimulation (FES) is a technique that uses electrical impulses to stimulate muscles and restore or enhance their function in individuals with neurological or muscular impairments. The integration of FES with motor actuation represents a promising avenue to enhance the capabilities of robotic locomotion. FES can be employed to stimulate muscles directly, enabling more natural and energy-efficient movements. Future work should explore the synergistic effects of combining FES with

conventional motor actuation, thereby improving the efficiency and adaptability of the locomotion system.

An essential yet unexplored aspect within this thesis pertains to the enhancement of sensory feedback and perception systems, which play a pivotal role in achieving superior control within real-world environments. To further elevate the practicality and adaptability of robotic systems, future research should center its efforts on the development of sensor fusion techniques. These techniques should seamlessly integrate data from diverse sources, including vision, proprioception, and tactile sensors. The creation of resilient perception models capable of dynamic adaptation to a wide array of terrains and scenarios represents a significant stride forward in advancing the field of robotics.

# Bibliography

- [1] H. S. Park, Y. Ren, and L. Q. Zhang, “Intelliarm: An exoskeleton for diagnosis and treatment of patients with neurological impairments,” in *IEEE RAS & EMBS International Conference on Biomedical Robotics and Biomechanics*, 2008, pp. 109–114.
- [2] W. H. O. (WHO), *Stroke, cerebrovascular accident*. [Online]. Available: <http://www.emro.who.int/health-topics/stroke-cerebrovascular-accident/index.html>.
- [3] SCIBC, *About spinal cord injury*. [Online]. Available: <https://sci-bc.ca/info-centre/spinal-cord-injury/>.
- [4] S. M. Anne Kawamura Amber Makino, *Comprehensive care of the ambulatory child with cerebral palsy (gmfcs i and ii): A canadian perspective*. [Online]. Available: <https://cps.ca/en/documents/position/>.
- [5] M. society, *Atlas of ms report shows 2.8 million people worldwide live with multiple sclerosis*. [Online]. Available: <https://mssociety.ca/resources/news/article/>.
- [6] H. S. Lo and S. Q. Xie, “Exoskeleton robots for upper-limb rehabilitation: State of the art and future prospects,” *Medical Engineering & Physics*, vol. 34, no. 3, pp. 261–268, 2012.
- [7] S. A. Murray et al., “Fes coupled with a powered exoskeleton for cooperative muscle contribution in persons with paraplegia,” in *Annual International Conference of the IEEE Engineering in Medicine and Biology Society (EMBC)*, 2018, pp. 2788–2792.
- [8] G. Zeilig et al., “Safety and tolerance of the rewalk™ exoskeleton suit for ambulation by people with complete spinal cord injury: A pilot study,” *The Journal of Spinal Cord Medicine*, vol. 35, pp. 96–101, 2012.
- [9] O. Jansen et al., “Hybrid assistive limb exoskeleton hal in the rehabilitation of chronic spinal cord injury: Proof of concept; the results in 21 patients,” *World neurosurgery*, vol. 110, pp. 73–78, 2018.
- [10] R. W. Evans et al., “Robotic locomotor training leads to cardiovascular changes in individuals with incomplete spinal cord injury over a 24-week rehabilitation period: A randomized controlled pilot study,” *Archives of Physical Medicine and Rehabilitation*, 2021.

- [11] K. A. Inkol and J. McPhee, “Assessing control of fixed-support balance recovery in wearable lower-limb exoskeletons using multibody dynamic modelling,” in *8th IEEE RAS/EMBS International Conference for Biomedical Robotics and Biomechatronics (BioRob)*, pp. 54–60.
- [12] A. Esquenazi et al., “Powered exoskeletons for walking assistance in persons with central nervous system injuries: A narrative review,” *PM&R*, vol. 9, no. 1, pp. 46–62, 2017.
- [13] J. K. Mehr, M. Akbari, P. Faridi, H. Xing, V. K. Mushahwar, and M. Tavakoli, “Artificial-intelligence-powered lower limb assistive devices: Future of home care technologies,” *Advanced Intelligent Systems*, p. 2200361, 2023.
- [14] V. Azimi et al., “Robust ground reaction force estimation and control of lower-limb prostheses: Theory and simulation,” *IEEE Transactions on Systems, Man, and Cybernetics: Systems*, vol. 50, pp. 3024–3035, 2020.
- [15] S. Grillner, “Biological pattern generation: The cellular and computational logic of networks in motion,” *Neuron*, vol. 52, no. 5, pp. 751–766, 2006.
- [16] A. Ijspeert et al., “From swimming to walking with a salamander robot driven by a spinal cord model,” *Science*, vol. 315, pp. 1416–1420, 2007.
- [17] T. Ji and A. Pachi, “Frequency and velocity of people walking,” *Struct. Eng.*, vol. 84, no. 3, pp. 36–40, 2005.
- [18] M. Sharifi, J. K. Mehr, V. K. Mushahwar, and M. Tavakoli, “Adaptive cpg-based gait planning with learning-based torque estimation and control for exoskeletons,” *IEEE Robotics and Automation Letters*, vol. 6, no. 4, pp. 8261–8268, 2021.
- [19] M. Sharifi, J. K. Mehr, V. K. Mushahwar, and M. Tavakoli, “Autonomous locomotion trajectory shaping and nonlinear control for lower limb exoskeletons,” *IEEE/ASME Transactions on Mechatronics*, vol. 27, no. 2, pp. 645–655, 2022.
- [20] J. K. Mehr, M. Sharifi, V. K. Mushahwar, and M. Tavakoli, “Intelligent locomotion planning with enhanced postural stability for lower-limb exoskeletons,” *IEEE Robotics and Automation Letters*, vol. 6, no. 4, pp. 7588–7595, 2021.
- [21] S. Schaal, “Dynamic movement primitives—a framework for motor control in humans and humanoid robotics,” in *Adaptive motion of animals and machines*, Springer, 2006, pp. 261–280.
- [22] Y. Yuan, Z. Li, T. Zhao, and D. Gan, “Dmp-based motion generation for a walking exoskeleton robot using reinforcement learning,” *IEEE Transactions on Industrial Electronics*, 2019.
- [23] S. Qiu, W. Guo, D. Caldwell, and F. Chen, “Exoskeleton online learning and estimation of human walking intention based on dynamical movement primitives,” *IEEE Transactions on Cognitive and Developmental Systems*, 2020.

- [24] R. Huang, H. Cheng, J. Qiu, and J. Zhang, “Learning physical human–robot interaction with coupled cooperative primitives for a lower exoskeleton,” *IEEE Transactions on Automation Science and Engineering*, vol. 16, no. 4, pp. 1566–1574, 2019.
- [25] S. Schrade et al., “Bio-inspired control of joint torque and knee stiffness in a robotic lower limb exoskeleton using a central pattern generator,” in *International Conference on Rehabilitation Robotics (ICORR)*, 2017, pp. 1387–1394.
- [26] K. Gui et al., “A generalized framework to achieve coordinated admittance control for multi-joint lower limb robotic exoskeleton,” in *International Conference on Rehabilitation Robotics (ICORR)*, 2017, pp. 228–233.
- [27] D. Zhang et al., “Cooperative control for a hybrid rehabilitation system combining functional electrical stimulation and robotic exoskeleton,” *Frontiers in Neuroscience*, vol. 11, p. 725, 2017.
- [28] X. Liu and Q. Wang, “Real-time locomotion mode recognition and assistive torque control for unilateral knee exoskeleton on different terrains,” *IEEE/ASME Transactions on Mechatronics*, 2020.
- [29] W. Wang et al., “Toward patients’ motion intention recognition: Dynamics modeling and identification of ileg—an llrr under motion constraints,” *IEEE Transactions on Systems, Man, and Cybernetics: Systems*, vol. 46, no. 7, pp. 980–992, 2016.
- [30] K. Gui et al., “A practical and adaptive method to achieve emg-based torque estimation for a robotic exoskeleton,” *IEEE/ASME Transactions on Mechatronics*, vol. 24, pp. 483–494, 2019.
- [31] Q. Wei, Z. Li, K. Zhao, Y. Kang, and C.-Y. Su, “Synergy-based control of assistive lower-limb exoskeletons by skill transfer,” *IEEE/ASME Transactions on Mechatronics*, vol. 25, no. 2, pp. 705–715, 2019.
- [32] T. Teramae, T. Noda, and J. Morimoto, “Emg-based model predictive control for physical human–robot interaction: Application for assist-as-needed control,” *IEEE Robotics and Automation Letters*, vol. 3, no. 1, pp. 210–217, 2017.
- [33] D. Ao, R. Song, and J. Gao, “Movement performance of human–robot cooperation control based on emg-driven hill-type and proportional models for an ankle power-assist exoskeleton robot,” *IEEE Transactions on Neural Systems and Rehabilitation Engineering*, vol. 25, no. 8, pp. 1125–1134, 2016.
- [34] D. Xu, Q. Wu, and Y. Zhu, “Development of a semg-based joint torque estimation strategy using hill-type muscle model and neural network,” *Journal of Medical and Biological Engineering*, pp. 1–11, 2020.
- [35] X. Wu, D.-X. Liu, M. Liu, C. Chen, and H. Guo, “Individualized gait pattern generation for sharing lower limb exoskeleton robot,” *IEEE Transactions on Automation Science and Engineering*, vol. 15, no. 4, pp. 1459–1470, 2018.

- [36] I. Kang et al., “Real-time neural network-based gait phase estimation using a robotic hip exoskeleton,” *IEEE Transactions on Medical Robotics and Bionics*, vol. 2, pp. 28–37, 2019.
- [37] R. Gupta et al., “Continuous angular position estimation of human ankle during unconstrained locomotion,” *Biomedical Signal Processing and Control*, vol. 60, p. 101968, 2020.
- [38] H. Kouzbary et al., “Generating an adaptive and robust walking pattern for a prosthetic ankle-foot by utilizing a nonlinear autoregressive network with exogenous inputs,” *IEEE Transactions on Neural Networks and Learning Systems*, pp. 1–9, 2021.
- [39] Y. Shen, Y. Wang, Z. Zhao, C. Li, and M. Q.-H. Meng, “A modular lower limb exoskeleton system with rl based walking assistance control,” in *2021 IEEE International Conference on Robotics and Biomimetics (ROBIO)*, IEEE, 2021, pp. 1258–1263.
- [40] R. Huang, H. Cheng, H. Guo, X. Lin, Q. Chen, and F. Sun, “Learning cooperative primitives with physical human-robot interaction for a human-powered lower exoskeleton,” in *2016 IEEE/RSJ International Conference on Intelligent Robots and Systems (IROS)*, IEEE, 2016, pp. 5355–5360.
- [41] P. Zhang and J. Zhang, “Motion generation for walking exoskeleton robot using multiple dynamic movement primitives sequences combined with reinforcement learning,” *Robotica*, pp. 1–16, 2022.
- [42] Z. Li, H. Ma, Y. Ding, C. Wang, and Y. Jin, “Motion planning of six-dof arm robot based on improved ddpq algorithm,” in *2020 39th Chinese Control Conference (CCC)*, 2020, pp. 3954–3959. DOI: 10.23919/CCC50068.2020.9188521.
- [43] S. Fujimoto, H. Hoof, and D. Meger, “Addressing function approximation error in actor-critic methods,” in *International Conference on Machine Learning*, 2018, pp. 1582–1591.
- [44] R. S. Sutton and A. G. Barto, *Reinforcement learning: An introduction*. MIT Press, 2018.
- [45] P. Henderson, R. Islam, P. Bachman, J. Pineau, D. Precup, and D. Meger, “Deep reinforcement learning that matters,” in *Proceedings of the AAAI conference on artificial intelligence*, vol. 32, 2018.
- [46] J. Kober, J. A. Bagnell, and J. Peters, “Reinforcement learning in robotics: A survey,” *The International Journal of Robotics Research*, vol. 32, no. 11, pp. 1238–1274, 2013.
- [47] M. Akbari, J. K. Mehr, L. Ma, and M. Tavakoli, “Uncertainty-aware safe adaptable motion planning of lower-limb exoskeletons using random forest regression,” *Mechatronics*, vol. 95, p. 103060, 2023.

- [48] Z. Peng *et al.*, “Data-driven reinforcement learning for walking assistance control of a lower limb exoskeleton with hemiplegic patients,” in *2020 IEEE International Conference on Robotics and Automation (ICRA)*, IEEE, 2020, pp. 9065–9071.
- [49] L. Rose, M. C. Bazzocchi, and G. Nejat, “A model-free deep reinforcement learning approach for control of exoskeleton gait patterns,” *Robotica*, vol. 40, no. 7, pp. 2189–2214, 2022.
- [50] L. Rose, M. C. Bazzocchi, and G. Nejat, “End-to-end deep reinforcement learning for exoskeleton control,” in *2020 IEEE International Conference on Systems, Man, and Cybernetics (SMC)*, IEEE, 2020, pp. 4294–4301.
- [51] A. Seth *et al.*, “Opensim: Simulating musculoskeletal dynamics and neuromuscular control to study human and animal movement,” *PLoS computational biology*, vol. 14, no. 7, e1006223, 2018.
- [52] R. Huang, H. Cheng, Q. Chen, H.-T. Tran, and X. Lin, “Interactive learning for sensitivity factors of a human-powered augmentation lower exoskeleton,” in *2015 IEEE/RSJ International Conference on Intelligent Robots and Systems (IROS)*, IEEE, 2015, pp. 6409–6415.
- [53] Y. Dong, Y. He, Z. Su, J. Ni, W. Feng, and X. Wu, “A motion planning method based on hrl for autonomous exoskeleton,” in *2021 IEEE International Conference on Real-time Computing and Robotics (RCAR)*, IEEE, 2021, pp. 1076–1081.
- [54] M. Shafiee-Ashtiani, A. Yousefi-Koma, and M. Shariat-Panahi, “Robust bipedal locomotion control based on model predictive control and divergent component of motion,” in *2017 IEEE International Conference on Robotics and Automation (ICRA)*, 2017, pp. 3505–3510. DOI: 10.1109/ICRA.2017.7989401.
- [55] T. Kamioka, H. Kaneko, T. Takenaka, and T. Yoshiike, “Simultaneous optimization of zmp and footsteps based on the analytical solution of divergent component of motion,” in *2018 IEEE International Conference on Robotics and Automation (ICRA)*, 2018, pp. 1763–1770. DOI: 10.1109/ICRA.2018.8460572.
- [56] H. Jeong, I. Lee, J. Oh, K. K. Lee, and J.-H. Oh, “A robust walking controller based on online optimization of ankle, hip, and stepping strategies,” *IEEE Transactions on Robotics*, vol. 35, no. 6, pp. 1367–1386, 2019.
- [57] T. Takenaka, T. Matsumoto, and T. Yoshiike, “Real time motion generation and control for biped robot -1st report: Walking gait pattern generation-,” in *2009 IEEE/RSJ International Conference on Intelligent Robots and Systems*, 2009, pp. 1084–1091. DOI: 10.1109/IROS.2009.5354662.
- [58] M. Khadiv, A. Herzog, S. A. A. Moosavian, and L. Righetti, “A robust walking controller based on online step location and duration optimization for bipedal locomotion,” *arXiv preprint arXiv:1704.01271*, 2017.

- [59] H. Jeong, I. Lee, O. Sim, K. Lee, and J.-H. Oh, “A robust walking controller optimizing step position and step time that exploit advantages of footed robot,” *Robotics and Autonomous Systems*, vol. 113, pp. 10–22, 2019.
- [60] J. Engelsberger, C. Ott, and A. Albu-Schäffer, “Three-dimensional bipedal walking control based on divergent component of motion,” *IEEE Transactions on Robotics*, vol. 31, no. 2, pp. 355–368, 2015. DOI: 10.1109/TRO.2015.2405592.
- [61] Q. Li *et al.*, “Contact force/torque control based on viscoelastic model for stable bipedal walking on indefinite uneven terrain,” *IEEE Transactions on Automation Science and Engineering*, vol. 16, no. 4, pp. 1627–1639, 2019. DOI: 10.1109/TASE.2019.2903564.
- [62] Y. Lee *et al.*, “Flexible gait enhancing mechatronics system for lower limb assistance (gems l-type),” *IEEE/ASME Transactions on Mechatronics*, vol. 24, no. 4, pp. 1520–1531, 2019. DOI: 10.1109/TMECH.2019.2922977.
- [63] Z. Li *et al.*, “Human-in-the-loop control of a wearable lower limb exoskeleton for stable dynamic walking,” *IEEE/ASME Transactions on Mechatronics*, pp. 1–1, 2020. DOI: 10.1109/TMECH.2020.3044289.
- [64] C. Buesing *et al.*, “Effects of a wearable exoskeleton stride management assist system (sma<sup>®</sup>) on spatiotemporal gait characteristics in individuals after stroke: A randomized controlled trial,” *Journal of neuroengineering and rehabilitation*, vol. 12, no. 1, pp. 1–14, 2015.
- [65] Y. Lee *et al.*, “A flexible exoskeleton for hip assistance,” in *2017 IEEE/RSJ International Conference on Intelligent Robots and Systems (IROS)*, IEEE, 2017, pp. 1058–1063.
- [66] C. A. McGibbon *et al.*, “Evaluation of the keeogo exoskeleton for assisting ambulatory activities in people with multiple sclerosis: An open-label, randomized, cross-over trial,” *Journal of neuroengineering and rehabilitation*, vol. 15, no. 1, pp. 1–14, 2018.
- [67] S. Kim and J. Bae, “Force-mode control of rotary series elastic actuators in a lower extremity exoskeleton using model-inverse time delay control,” *IEEE/ASME Transactions on Mechatronics*, vol. 22, no. 3, pp. 1392–1400, 2017.
- [68] Y. Yang, X. Dong, X. Liu, and D. Huang, “Robust repetitive learning-based trajectory tracking control for a leg exoskeleton driven by hybrid hydraulic system,” *IEEE Access*, vol. 8, pp. 27 705–27 714, 2020.
- [69] J. Fang, Y. Ren, and D. Zhang, “A robotic exoskeleton for lower limb rehabilitation controlled by central pattern generator,” in *2014 IEEE International Conference on Robotics and Biomimetics (ROBIO 2014)*, IEEE, 2014, pp. 814–818.
- [70] R. Luo, S. Sun, X. Zhao, Y. Zhang, and Y. Tang, “Adaptive cpg-based impedance control for assistive lower limb exoskeleton,” in *2018 IEEE International Conference on Robotics and Biomimetics (ROBIO)*, IEEE, 2018, pp. 685–690.

- [71] C. T. Pan *et al.*, “Development a multi-loop modulation method on the servo drives for lower limb rehabilitation exoskeleton,” *Mechatronics*, vol. 68, p. 102 360, 2020.
- [72] W. Huo, M. A. Alouane, Y. Amirat, and S. Mohammed, “Force control of sea-based exoskeletons for multimode human–robot interactions,” *IEEE Transactions on Robotics*, 2019.
- [73] W. Huo, S. Mohammed, and Y. Amirat, “Impedance reduction control of a knee joint human-exoskeleton system,” *IEEE Transactions on Control Systems Technology*, vol. 27, no. 6, pp. 2541–2556, 2018.
- [74] F. Ghorbel, B. Srinivasan, and M. W. Spong, “On the uniform boundedness of the inertia matrix of serial robot manipulators,” *Journal of Robotic Systems*, vol. 15, no. 1, pp. 17–28, 1998. DOI: 10.1002/(SICI)1097-4563(199812)15:1<17::AID-ROB2>3.0.CO;2-V.
- [75] M. Sharifi, H. Salarieh, S. Behzadipour, and M. Tavakoli, “Impedance control of non-linear multi-dof teleoperation systems with time delay: Absolute stability,” *IET Control Theory & Applications*, vol. 12, no. 12, pp. 1722–1729, 2018.
- [76] J. Slotine and W. Li, *Applied Nonlinear Control*. Prentice-Hall, 1991, ISBN: 9780130400499.
- [77] A. J. Ijspeert, A. Crespi, D. Ryczko, and J.-M. Cabelguen, “From swimming to walking with a salamander robot driven by a spinal cord model,” *Science*, vol. 315, no. 5817, pp. 1416–1420, 2007, ISSN: 0036-8075. DOI: 10.1126/science.1138353.
- [78] P. Ioannou and J. Sun, *Robust Adaptive Control* (Dover Books on Electrical Engineering Series). Dover Publications, Incorporated, 2012, ISBN: 9780486498171.
- [79] M. N. Mahyuddin, J. Na, G. Herrmann, X. Ren, and P. Barber, “Adaptive observer-based parameter estimation with application to road gradient and vehicle mass estimation,” *IEEE Transactions on Industrial Electronics*, vol. 61, no. 6, pp. 2851–2863, 2014.
- [80] S. Sastry and M. Bodson, *Adaptive Control: Stability, Convergence and Robustness*. Dover Publications, 2011, ISBN: 9780486482026.
- [81] V. Azimi, D. Simon, and H. Richter. “Kinematic and kinetic human gait data for able-bodied and transfemoral amputee subjects.” (), [Online]. Available: <https://www.vahidazimi.com/data-code>.
- [82] V. Azimi, S. Abolfazl Fakoorian, T. Tien Nguyen, and D. Simon, “Robust adaptive impedance control with application to a transfemoral prosthesis and test robot,” *Journal of Dynamic Systems, Measurement, and Control*, vol. 140, no. 12, 2018.
- [83] M. Sharifi *et al.*, “Patient-Robot-Therapist Collaboration Using Resistive Impedance Controlled Tele-Robotic Systems Subjected to Time Delays,” *Journal of Mechanisms and Robotics*, vol. 10, p. 061 003, 2018.

- [84] A. A. Blank et al., “Current trends in robot-assisted upper-limb stroke rehabilitation: Promoting patient engagement in therapy,” *Current Physical Medicine and Rehabilitation Reports*, vol. 2, pp. 184–195, 2014.
- [85] M. Sharifi et al., “Impedance variation and learning strategies in human-robot interaction,” *IEEE Transactions on Cybernetics*, pp. 1–14, 2021. DOI: 10.1109/TCYB.2020.3043798.
- [86] W. Meng et al., “Recent development of mechanisms and control strategies for robot-assisted lower limb rehabilitation,” *Mechatronics*, vol. 31, pp. 132–145, 2015. DOI: <https://doi.org/10.1016/j.mechatronics.2015.04.005>.
- [87] M. Shahbazi et al., “Robotics-assisted mirror rehabilitation therapy: A therapist-in-the-loop assist-as-needed architecture,” *IEEE/ASME Transactions on Mechatronics*, vol. 21, pp. 1954–1965, 2016. DOI: 10.1109/TMECH.2016.2551725.
- [88] M. Sharifi et al., “Impedance learning-based adaptive control for human-robot interaction,” *IEEE Transactions on Control Systems Technology*, pp. 1–14, 2021.
- [89] J. Vantilt et al., “Model-based control for exoskeletons with series elastic actuators evaluated on sit-to-stand movements,” *Journal of NeuroEngineering and Rehabilitation*, vol. 16, p. 65 (21 pages), 2019.
- [90] A. Riani et al., “Adaptive integral terminal sliding mode control for upper-limb rehabilitation exoskeleton,” *Control Engineering Practice*, vol. 75, pp. 108–117, 2018, ISSN: 0967-0661. DOI: <https://doi.org/10.1016/j.conengprac.2018.02.013>.
- [91] R. Lu et al., “Development and learning control of a human limb with a rehabilitation exoskeleton,” *IEEE Transactions on Industrial Electronics*, vol. 61, no. 7, pp. 3776–3785, 2014. DOI: 10.1109/TIE.2013.2275903.
- [92] M. Sharifi et al., “Assist-as-needed policy for movement therapy using telerobotics-mediated therapist supervision,” *Control Engineering Practice*, vol. 101, p. 104 481, 2020, ISSN: 0967-0661. DOI: <https://doi.org/10.1016/j.conengprac.2020.104481>.
- [93] E. Diaconescu, “The use of narx neural networks to predict chaotic time series,” *Wseas Transactions on computer research*, vol. 3, pp. 182–191, 2008.
- [94] L. Xin et al., “Omnidirectional mobile robot dynamic model identification by narx neural network and stability analysis using the aplf method,” *Symmetry*, vol. 12, p. 1430, 2020.
- [95] H. Xie et al., “Time series prediction based on narx neural networks: An advanced approach,” in *International Conference on Machine Learning and Cybernetics*, 2009, pp. 1275–1279.
- [96] L. Du et al., “Response characteristics prediction of surge protective device based on narx neural network,” *IEEE Transactions on Electromagnetic Compatibility*, vol. 62, pp. 74–82, 2020.

- [97] S. Guo, Y. Ding, and J. Guo, “Control of a lower limb exoskeleton robot by upper limb semg signal,” in *2021 IEEE International Conference on Mechatronics and Automation (ICMA)*, IEEE, 2021, pp. 1113–1118.
- [98] Y. He *et al.*, “Gc-igtg: A rehabilitation gait trajectory generation algorithm for lower extremity exoskeleton,” in *2019 IEEE International Conference on Robotics and Biomimetics (ROBIO)*, IEEE, 2019, pp. 2031–2036.
- [99] L. Shore, “Development of a design tool to optimise acceptance of exoskeletons by older adults,” Ph.D. dissertation, University of Limerick, 2019.
- [100] J. K. Mehr, E. Guo, M. Akbari, V. K. Mushahwar, and M. Tavakoli, “Deep reinforcement learning based personalized locomotion planning for lower-limb exoskeletons,” in *2023 IEEE International Conference on Robotics and Automation (ICRA)*, IEEE, 2023, pp. 5127–5133.
- [101] A. M. et al., “A velocity-field-based controller for assisting leg movement during walking with a bilateral hip and knee lower limb exoskeleton,” *IEEE Trans. Robot.*, vol. 35, no. 2, pp. 307–316, 2019.
- [102] L. Zhou et al., “A novel precision measuring parallel mechanism for the closed-loop control of a biologically inspired lower limb exoskeleton,” *IEEE/ASME Trans. Mechatron.*, vol. 23, no. 6, pp. 2693–2703, 2018. DOI: 10.1109/TMECH.2018.2872011.
- [103] T. Takenaka et al., “Real time motion generation and control for biped robot -1st report: Walking gait pattern generation-,” in *IROS*, 2009, pp. 1084–1091. DOI: 10.1109/IROS.2009.5354662.
- [104] M. Khadiv et al., “A robust walking controller based on online step location and duration optimization for bipedal locomotion,” *CoRR*, vol. abs/1704.01271, 2017. arXiv: 1704.01271. [Online]. Available: <http://arxiv.org/abs/1704.01271>.
- [105] M. Khadiv et al., “Step timing adjustment: A step toward generating robust gaits,” in *Humanoids*, IEEE, 2016, pp. 35–42.
- [106] D. A. Winter, *Biomechanics and motor control of human movement*. John Wiley & Sons, 2009.

# Appendix A: DCM dynamics

## A.1 Inertia matrix and gravity vector values:

The elements of inertia matrix  $M$  are

$$\begin{aligned}
 M_{11} &= m_1 l_{c1}^2 + m_2 (l_1 + l_{c2})^2 + m_3 (l_1 + l_{c3})^2 + \\
 &\quad m_4 (l_1 + l_3 + l_{c4})^2 + I_1 + I_2 + I_3 + I_4 \\
 M_{12} &= m_2 l_{c2} (l_1 + l_{c2}) + m_3 l_{c3} (l_1 + l_{c3}) + \\
 &\quad m_4 (l_3 + l_{c4}) (l_1 + l_3 + l_{c4}) + I_2 + I_3 + I_4 \\
 M_{13} &= m_3 l_{c3} (l_1 + l_{c3}) + m_4 (l_3 + l_{c4}) (l_1 + l_3 + l_{c4}) + \\
 &\quad I_3 + I_4 \\
 M_{14} &= m_4 l_{c4} (l_1 + l_3 + l_{c4}) + I_4 \\
 M_{22} &= m_2 l_{c2}^2 + m_3 l_{c3}^2 + m_4 (l_3 + l_{c4})^2 + I_2 + I_3 + I_4 \\
 M_{23} &= m_3 l_{c3}^2 + m_4 (l_3 + l_{c4})^2 + I_3 + I_4 \\
 M_{24} &= m_4 l_{c4} (l_3 + l_{c4}) + I_4 \\
 M_{33} &= m_3 l_{c3}^2 + m_4 (l_3 + l_{c4})^2 + I_3 + I_4 \\
 M_{34} &= m_4 l_{c4} (l_3 + l_{c4}) + I_4 \\
 M_{44} &= m_4 l_{c4}^2 + I_4
 \end{aligned} \tag{A1}$$

and the elements of gravity matrix  $G$  are obtained as

$$\begin{aligned}
 G_{11} &= 3m_1 g l_1 + m_1 g l_{c1} \\
 G_{12} &= G_{22} = m_2 g l_{c2} \\
 G_{13} &= G_{23} = G_{33} = -m_3 g l_3 - m_3 g l_{c3} \\
 G_{14} &= G_{24} = G_{34} = G_{44} = -m_4 g l_{c4}
 \end{aligned} \tag{A2}$$

in which  $g$  is the gravitational acceleration.

## A.2 DCM definition

The motion of HES center of mass can be divided into the convergent ( $C$ ) and divergent ( $D$ ) components as

$$\begin{aligned} C &= x_{CoM} - \frac{\dot{x}_{CoM}}{\sqrt{\alpha}} \\ D &= x_{CoM} + \frac{\dot{x}_{CoM}}{\sqrt{\alpha}} \end{aligned} \tag{A3}$$

where  $x_{CoM}$  and  $\dot{x}_{CoM}$  denote the position and velocity of the center of mass and  $\alpha$  is a constant value defined in (8). Taking the time derivative of (A3) and substituting (7) in the absence of control input ( $\tau = 0$ ), the time derivative of the divergent and convergent parts are obtained as

$$\begin{aligned} \dot{C} &= -\sqrt{\alpha}C \\ \dot{D} &= \sqrt{\alpha}D \end{aligned} \tag{A4}$$

As seen, the convergent part of the motion ( $C$ ) will converge to zero without any control effort. Therefore, controlling the divergent part of the motion ( $D$ ) will guarantee the convergence of  $x_{CoM}$  to its corresponding desired value. Accordingly, the DCM is defined as

$$\zeta = x_{CoM} + \frac{\dot{x}_{CoM}}{\sqrt{\alpha}} \tag{A5}$$

and the paper is focused on the control of the DCM by adjusting the control input ( $\tau$  in (7)).